SAPIENZA
UNIVERSITÀ DI ROMA

EMBL

Facoltà di Scienze Matematiche Fisiche e Naturali

DOTTORATO DI RICERCA
IN NEUROSCIENZE DEL COMPORTAMENTO
XXXVIII Ciclo (A.A. 2025/2026)

# Active vision across scales: internal signals shape visual processing from retinal circuits to cortical population dynamics

Dottorando
Pietro Micheli

Docente guida
Dr. Santiago Rompani

Coordinatore
Prof. Stefano Ferraina

# Acknowledgements

There are so many people who, in one way or another, contributed to making the years of my PhD a truly memorable journey, a journey of intense scientific and personal growth.

First, I would like to thank my supervisor, Santiago. From the beginning, he always cared about helping me grow as a scientist according to my interests and perspectives, fostering my love for this work and helping me develop the tools and the confidence to follow this career path. For this, and for his genuine openness to dialogue and discussion, I am truly grateful. I would then like to thank my lab mates, particularly the people with whom I shared most of this journey; these are the people who directly contributed to making my workplace a pleasant yet intellectually stimulating environment, where all the frustration that inevitably comes from scientific research could be diluted with smiles, laughter, and a lot of panini from Renatone. Thank you, Tjasa, for your kindness and enthusiasm. It was so easy and smooth to work with you on our project, and I am proud of what we managed to achieve together. Thank you, Gioia, for being a constant source of inspiration, both scientifically and humanly. You've always been so supportive and caring, and for that I'm deeply grateful to you. Thank you, Alex. I enjoyed our conversations so much, and you truly helped me in shaping a more mature theoretical mindset. Thank you Andres for all the smiles, your knowledge and the crazy hard work you put in the lab. Thank you, Aiendrila, for sharing this journey with me from the very beginning to the very end; all the bad, all the good, it was always reassuring to have someone like you to talk and confront myself with. Thank you all!

During this time at EMBL, I feel lucky to say that I met a lot of people whom I consider much more than simple colleagues, people who enriched my daily life and directly contributed to making my time in Rome so enjoyable. Thank you, Fir, for the laughs, the chats, the encouragement, the sunglasses, the wigs, the clothes, and the fun nights. Thank you, Celeste, for your friendship, for your generosity and hospitality, for the pastry workshops, for your inspiring temper, and for your very cool family. Thank you, Irene, for the endless deep talks on life, science, and more; thank you for your always genuine enthusiasm, for being my friend, and for sharing fun and pain. Thank you, Francesco, for being a generous grumpy bear; thank you for all the laughter, the jokes, the beers and the dunny moments we shared in these years.
Thank you, Demetra, for bringing so much energy, passion, and a spark of wonderful chaos to my days; I feel so lucky I got to see what a special and truly unique person you are.

A special remark goes to Flavio. Thank you for literally everything. Thank you for being such a beautiful person from every possible angle. Thank you for sharing daily life with me and for making it so light and enjoyable. Thank you for the fun, thank you for your wisdom, for your so pleasant temper, for your patience, for your generosity, and for your hospitality. On this note, I also want to take the opportunity to thank Antonella, Antonio, Giordano, and Giuliano; you've been my sort of Roman family, and you made me feel so warmly welcomed from the very beginning. For that, I'm deeply grateful.

Thanks to my friends in Brescia for making me feel at home every time I come back. Thanks for being a group of such cool and interesting people; thanks for the fun, thanks for the drama. Thank you, Livio, for your true friendship, for being such an inspiring person, and for your kindness and care; you are family. Thank you, Bianca, for your love, for contributing to making me the person I am today, for endlessly believing in me during all these years, and for reminding me that I should do it myself too.

A final thanks goes to my family. Thank you to my mom, to my dad, and to my sister. Thank you for always caring only about my true happiness and wellbeing. Thank you for your unconditional love and support, thank you for always believing in what I am and what I can become. Thank you for proving it on a daily basis. I feel truly lucky to know you are in my life no matter what, and you will always be my home. Finally, a special thanks to my nonni Franco and Renata. Thank you for everything you taught me during these many years, for the wisdom, for your encouragement and for the love.

I've always been intrigued by observing and trying to find a rationale for what makes life such a wonderful phenomenon, but it is thanks to people that I realized that living the beauty of life is the only way we can gain access to its most hidden mysteries.

# Content

# Content

# List of figures

# List of figures

# List of figures

# Aims

The overarching aim of this thesis is to investigate how internally-generated state signals shape visual processing across multiple stages of the visual pathway within the broader framework of active vision. Rather than conceptualizing vision as a passive feedforward transformation of external stimuli, the active vision perspective emphasizes that sensory input is continuously shaped by motor, autonomic, and internal brain processes. Neural activity in the visual system therefore reflects not only the structure of the external world, but also internally-generated signals that regulate how sensory information is sampled, filtered, and represented. These signals can act peripherally, by directly shaping the input reaching the retina, or centrally, by modulating the cortical population dynamics underlying sensory encoding. In this thesis I examine both levels of interaction, describing two complementary projects that I pursued during my PhD journey.

The first project is the result of a close collaboration with Tjaša Lapanja, a former PhD student in the lab. The project focuses on the pupillary light reflex (PLR) and its impact on early visual processing. The PLR is classically described as a subcortical reflex that adjusts retinal illumination in response to changes in ambient light. In this view, pupil constriction serves primarily an optical function, adjusting the photon flux onto photoreceptors. However, in this work we demonstrate that PLR-induced changes in pupil size do not merely normalize the retinal responses to ambient luminance, but instead can actively drive retinal activity. By performing 2-photons calcium imaging recordings in mice, we show that pupil constrictions generate structured responses in retinal ganglion cells that propagate through central visual pathways. Complementary psychophysical experiments in humans indicate that these pupil-driven retinal signals influence perceptual experience. This work therefore repositions the PLR as an active component of visual encoding, highlighting how a brainstem-mediated motor reflex can shape early sensory representations. The project resulted in a peer-reviewed publication of which me and Tjaša are co-first authors[1].

The second project addresses how internal brain states, particularly arousal, reshape neural activity at the cortical level. Here, the focus shifts from peripheral modulation of retinal input to central modulation of population dynamics in primary visual cortex (V1). Using in vivo two-photon calcium imaging during continuous visual stimulation, I investigated how arousal reorganizes the geometry and dimensionality of cortical population activity in layer 2/3 and layer 4 of V1.

# Aims

This work reveals layer-specific embedding of arousal signals and demonstrates that internal state fluctuations interact with stimulus complexity to reshape cortical representations over slow timescales.

Together, these two projects provide a multi-level perspective on state-dependent visual processing. The first demonstrates that reflexive, brainstem-driven pupil dynamics can directly shape retinal output. The second shows how global internal states reorganize cortical population geometry during sustained sensory drive. By bridging peripheral and cortical levels, this thesis proposes that visual processing is continuously shaped by centrally generated signals that operate across hierarchical stages of the visual system.

# Chapter 1

## Introduction

## 1.1. The image-forming pathway

### 1.1.1. Overview

Among all the various sensory modalities, vision is by far the most fundamental in humans. Through vision, organisms acquire detailed information about the spatial layout, identity, and dynamics of their environment. This enables fine-tuned behaviours ranging from navigation, and object recognition to risk assessment and thread avoidance. To support these functions, the visual system is able to capture and encode the spatio-temporal patterns of light emitted from the environment, building more and more integrated and abstract neural representations, distributed across multiple processing stages. Although important differences exist between human and mouse vision, the latter provides a particularly convenient model for studying the mechanisms of the neuronal computations underlying image formation. Mice offer unparalleled experimental accessibility, allowing the combination of genetic tools, large-scale neural recordings, cell-type–specific manipulations, and behavioural assays within the same preparation. Moreover, the organisation of the mouse visual pathway shares key canonical features with that of primates, including a hierarchical image-forming pathway, retinotopic organisation, and layered cortical architecture in V1, making it well-suited for investigating general principles of sensory processing.

The hierarchical structure of the early visual pathway allows for a sequential processing of the visual information, where different features of the visual scene can be extracted and encoded into specific patterns of neural activity. This computational process starts with the retina, which is able to capture the light emitted by the different elements composing the environment that

surrounds the organism. Here, an incredibly rich and well-structured neuronal circuit generates spatially resolved, local representations of luminance and contrast patterns. These are then sequentially fed to downstream brain areas, which implement more and more complex transformations on the raw visual information, tailored to a prioritized representation of specific visual features. Specifically, the information collected by the retina travels through the optic nerve up the dorsal part of the Lateral Geniculate Nucleus. Here, individual neurons start integrating the different information channels before projecting to the visual cortex for further, higher-level feature extraction. Within cortical areas, semantically richer representations of the visual scene can then emerge and inform downstream higher cognitive process.

### 1.1.2. The Retina

The journey that will lead to the generation of the so-called neural image, the representation of the visual world encoded in patterns of neural activity, starts with the retina. This is the very first step of the image-forming pathway, where the light coming from different portions of the visual field is collected, preserving its spatial organization. After passing through the pupil and the lens, the image is inverted and projected to the retina. In creatures where the field of views covered by each of the two eyes overlap, part of the temporal retina collects information from the binocular portion of the field of view, while the nasal part from the monocular one. The vertebrate retina comprises five classes of neurons that are arranged into three nuclear and two synaptic layers [2] (Fig 1.1). The first synaptic layer, known as the outer plexiform layer, hosts the photoreceptors. These cells constitute the actual sensors of the system, in charge of transducing the photons coming from the visual scene in electrical signals that can be passed to other cells for integration and processing. Photoreceptors come in two main flavours: the rods are mainly active in dim light conditions and quickly saturate in bright light. Cones, on the other hand, are active in bright light conditions and able to selectively respond to specific, narrow, wavelength range according to the particular cone subtype, allowing for colour vision.

At the core of retinal computation lies the transformation of the photoreceptor signal into multiple parallel channels, each emphasizing distinct aspects of the visual scene. A fundamental example of this processing is the

separation between ON and OFF pathways, first suggested by the observation that retinal ganglion cells can be excited either by light increments or by light decrements within their receptive-field centre [3,4]. This division originates at the first synapse between photoreceptors and bipolar cells: OFF bipolar cells preserve the sign of the photoreceptor signal, whereas ON bipolar cells invert it through a distinct glutamatergic receptor mechanism. As a result, increases and decreases in local luminance are already represented by partially separate circuits before reaching the ganglion cell layer. Together with lateral interactions mediated by horizontal and amacrine cells, this organization gives rise to centre-surround receptive fields, which emphasize local contrast rather than absolute light intensity [4,5]. The retina therefore does not simply transmit a pixel-wise representation of the visual scene, but performs an early decomposition of visual information into parallel feature channels, such as contrast polarity, spatial contrast, temporal dynamics, colour opponency and motion-related signals.

In the outer plexiform layer, the photoreceptors release glutamate onto the dendrites of the bipolar cells and horizontal cells. Here, the bipolar cells are mainly responsible for feeding the information forward across the next layers of the retina, while the horizontal cells provides both feedback and feedforward signals to the photoreceptors and the bipolar cells respectively. At this stage, the bipolar cells project to the inner plexiform layer, where they contact the dendritic processes of the amacrine cells and the retinal ganglion cells (RGCs). Here, like for the horizontal cells in the outer plexiform layer, the role of amacrine cells is mainly to integrate and modulate the feedforward information coming from the bipolar cells, through feedback inhibition and feedforward signals. The vast diversity of amacrine cells that has been characterized in the mouse retina suggests the idea that they play crucial roles in the early extraction of low-level visual features that already happens inside the retina. Although many of those functions are still poorly understood, a classic example of computation carried out but by the starburst amacrine cells is the ability of encoding the directions of motion present in the visual scene [6].

The journey of the retina ends then with the RGCs. These neurons are the ones responsible for integrating the signals coming from the bipolar and the amacrine cells, and constitute the last stage of the retinal computation. Their axonal projections form the optic nerve, which, among other brain areas not involved in the image-forming pathway, pass the information to the Lateral

Geniculate Nucleus (LGN). The RGCs integrate the local features extracted in the earlier stages of the retinal computation. They are characterized by a circular centre-surround receptive field, and their activity selectively encodes for specific, low-level local features of the visual scene such as contrast, spectral or directional information. The extent of the functional heterogeneity of the RGC populations have been studied thoroughly, reporting over then 30 different functional types, each one tuned for a specific set of low-level visual features [7]. Each different functional RGC population forms a separate channel, which passes the pre-processed information to the next stages of the pathway.

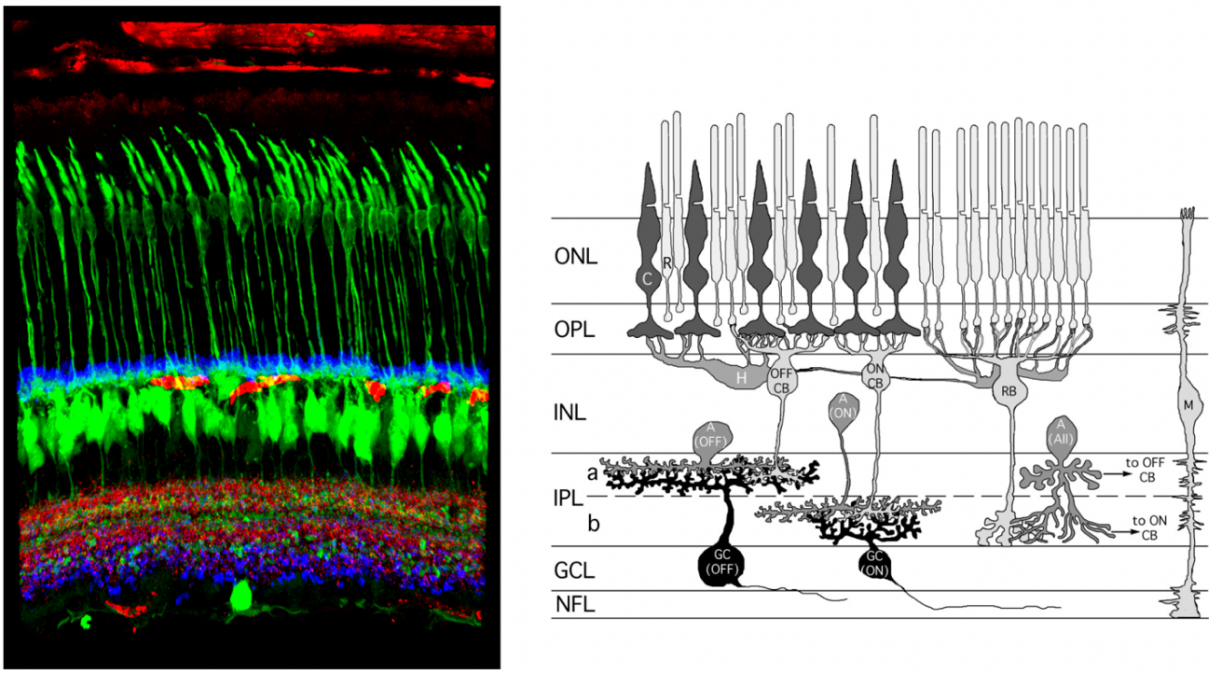


***Figure 1.1. Major retinal cell types and synaptic pathways in the mouse retina.***
***Left**: Confocal image of the mouse retina showing labeled neuronal cell types (image adapted from M.J. Ruiz- Pastor). **Right**:Schematic representation of the retinal layers—ONL, outer nuclear layer; OPL, outer plexiform layer; INL, inner nuclear layer; IPL, inner plexiform layer; GCL, ganglion cell layer; NFL, nerve fiber layer (image adapted from Wiley-Liss).*

### 1.1.3. Lateral Geniculate Nucleus

The visual information leaves the retina through the optic nerve and reaches the optic chiasm: here the axons coming from the nasal portion of the retina, which mainly collect information from the monocular side of the field of view, decussate, crossing the chiasm and projecting to several subcortical areas. The fibres originating from the temporal portion of the retina generally don't cross the chiasm, projecting instead on the ipsilateral hemisphere. One of the principal targets of the retinal projections is the Lateral Geniculate Nucleus (LGN), which constitute the area where the next processing step of the image forming pathway takes place. The majority of the RGC axons projecting to the LGN come from the contralateral retina, with only 5-10% of RGC axons originating in the temporal part of the ipsilateral retina. The LGN constitutes the principal thalamic relay of image-forming visual information to the neocortex and preserves a precise retinotopic organization while actively shaping retinal signals before their transmission to primary visual cortex (V1) [8].

Across species, the LGN exhibits marked anatomical specialisation. In primates, the LGN is highly laminated, with distinct magnocellular, parvocellular, and koniocellular layers that receive input from functionally segregated RGC classes [9]. In carnivores such as the cat, the LGN also exhibits clear lamination and parallel processing streams, though with differences in layer number and functional organisation compared to primates [10]. By contrast, the rodent LGN lacks prominent laminar structure and instead displays a more compact cytoarchitecture [11], although a segregation of the retinal projections into ipsilateral and contralateral retinorecipient region is present [12].

At the cellular level, the LGN comprises thalamocortical relay neurons, which project primarily to layer 4 and layer 1 of V1, and a population of non-relay neurons, including local GABAergic interneurons that lack direct cortical projections [13]. Beyond faithfully relaying retinal signals, thalamocortical neurons in the LGN implement a range of transformations that reshape visual information before its transmission to cortex. Classical work has shown that LGN neurons act as dynamic filters, adjusting temporal integration, contrast gain, and response linearity as a function of stimulus statistics and behavioural state [8]. In mice, recent studies have demonstrated that these transformations are more diverse than previously appreciated. [14] showed that mouse LGN relay neurons receive convergent input from multiple

functionally distinct retinal ganglion cell types, allowing for complex combinations of different retinal information channels. This further supports the idea that the LGN actively recombines retinal information rather than merely preserving parallel channels.

In addition to the convergence of different functional types of RGCs to the same target LGN neurons, the transformations that these neurons apply on the ascending visual information are also strongly influenced by neuromodulatory systems. The LGN receives dense modulatory input from brainstem and hypothalamic nuclei, including cholinergic afferents from the parabrachial region, noradrenergic input from the locus coeruleus, serotonergic projections from the dorsal raphe, and dopaminergic innervation from midbrain sources [13,15,16]. These neuromodulators regulate membrane excitability, synaptic efficacy, and firing mode, thereby controlling the balance between tonic and burst firing and modulating the gain and reliability of thalamocortical transmission [17]. Recently, [18] suggested how, based on brain slice electrophysiology, immunohistochemistry, anatomical projections, and single cell sequencing data, the activity of serotonergic projections to the LGN may contribute to the selective suppression of specific retinal axonal boutons.

Together, these findings support a view of thalamocortical relay neurons as adaptive processors that integrate retinal drive with local inhibition, corticothalamic feedback, and neuromodulatory signals. Rather than functioning as a passive gateway, the mouse LGN dynamically transforms and gates visual information in a state-dependent manner, shaping the signals delivered to cortex and thereby influencing cortical representations [18,19].

### 1.1.4. Visual Cortex

At this stage of the image forming pathway, the visual signals can then enter the primary visual cortex (V1) via thalamocortical projections originating in the LGN. Here, the thalamic representations pass through a highly structured laminar circuit, whose organization supports a sequential yet recurrent flow of information.

Feedforward sensory input is here progressively transformed through the interactions between a variety of different cell types, local recurrent connectivity, long-range feedbacks and modulatory inputs, generating richer representations of the visual scene. Despite its evident idealization, the notion of mammalian neocortex as a six-layered structure is generally accepted and widely used as the reference for describing a wide range of anatomical and physiological data [20].

*Layer 4* (L4) constitutes the principal recipient of thalamocortical input and serves as the main gateway for retinal information into the cortical circuitry. In rodents, LGN axons predominantly terminate in L4 and deep L3, forming strong synapses onto L4 neurons. Several different morphological cells types have been characterized in L4 in adult mice. These includes excitatory pyramidal cells with a non-complex dendritic arborization in layer 1, Parvalbumin-positive GABAergic large basket cells which provide local inhibition, and Somatostatin-positive, GABAergic Martinotti cells which also project to layer 1, potentially able to synapse onto the tuft of L4 pyramidal cells [21]. Functionally, the receptive fields of L4 neurons look quite similar to those characterizing the LGN neurons, but with amplified tuning properties for the phase, orientation and spatial structure of the visual stimulus, reflecting the integration of convergent thalamic input and local inhibition [22]. L4 principal cells project to all layers, but most strongly to layers 2/3.

From L4, activity propagates to *layers 2/3* (L2/3), which form a major site of intracortical integration and horizontal communication. Neurons in L2/3 are predominantly pyramidal cells with extensive horizontal axonal projections that link cortical columns with similar functional properties across V1 and higher visual areas. L2/3 sends a major descending interlaminar axonal projection that branches extensively and densely in L5A and L5B, but not in L4. This L2/3→5A/B pathway appears to be a particularly prominent and consistent feature of cortical circuits across areas and species [23].

L2/3 neurons exhibit sharper tuning for orientation, direction, as well as increased selectivity for more complex stimulus features compared to L4, reflecting nonlinear integration of feedforward input with recurrent excitation and inhibition [24]. Due to the high level of cortico-cortical horizontal projections that characterize this layer, modulation from other cortical areas allows also for contextual and multimodal integration of different streams of information [25,26]. Moreover, afferences from several different neuromodulatory systems allow for the activity in L2/3 to be strongly modulated by behavioural and state-dependent signals [27–29].

*Layer 1* (L1) is the most superficial layer of the cortex. Although be scarcely populated by excitatory cells, this layer has a particularly important modulatory role in cortical processing. L1 is dominated by the apical dendritic tufts of neurons projecting from deeper layers, as well as a population of GABAergic interneurons, including neurogliaform cells [30]. It receives dense feedback projections from higher cortical areas and neuromodulatory inputs from cholinergic and noradrenergic systems [31]. Thanks to these feedbacks and modulatory inputs, L1 plays an important role in regulating dendritic integration in pyramidal neurons from deeper layers, shaping sensory processing without directly driving spiking activity [32]. L1 in V1 constitute a key site for the interaction between the early sensory representations and behavioral signals, shaping the sensory processing and making it highly state-dependent.

Following processing in superficial layers, the information containing the integrated, behaviourally-shaped sensory representations is projected down to *layer 5* (L5). This layer is main output of the cortical circuitry. Here the pyramidal cells, characterized by a prominent dendritic tuft in L1 and long-range axonal projections, sends the cortical output down to several subcortical targets, including the superior colliculus, thalamus and brainstem. L5 neurons also generate feedback projections to the superficial layers, constraining the ongoing cortical processing with the current output, both in the same as well as in different cortical regions [20].

Finally, *layer 6* (L6) plays a central role in feedback control and gain regulation of the cortical processing within the thalamocortical loop. The pyramidal cells in L6 of V1 are morphologically diverse and characterized by different projection patterns. These cells receive direct input from L5 and feedback the cortical output both locally to the input L4, closing the cortical loop,

and to the LGN, forming the corticothalamic feedback pathways [20,33]. The descending feedback projections from L6 target most of the thalamic relay nuclei. Such projections don't act as a direct driver of the thalamocortical cells, but rather as a modulator, shaping the subcortical feedforward sensory processing accordingly to the current information extracted by the cortical computation [34].

Together, the laminar architecture of V1 supports a structured yet flexible flow of visual information, in which thalamic input is progressively transformed through layer-specific computations and dynamically modulated by feedback and internal state signals. This organisation provides the substrate through which early sensory representations are integrated and shaped into context- and state-dependent cortical codes.

# 1.2. The role of pupillary dynamics in shaping vision

## 1.2.1. Overview

The pupil constitutes a dynamic optical aperture that regulates the amount of light entering the eye and thus directly shapes the statistics of the retinal input available for neural processing. By adjusting retinal illuminance, pupil size can influence signal-to-noise ratio, contrast sensitivity, depth of field, and visual acuity, thereby modulating both the sampling and the early transformations on the visual information operated by the retina [35]. The dynamic modulation of pupil diameter is operated by the antagonistic smooth muscles of the iris, namely the sphincter muscles and the dilator muscles. Such muscles are innervated by different motor afferences, controlled by very distinct pathways: the sphincter muscle receives parasympathetic innervations, which start from the Edinger-Westphal nucleus and enter the orbit through the oculomotor nerve; notably, the Edinger-Westphal nucleus receives strong, bilateral innervation from the pretectal olivary nucleus which directly relays retinal information. On the other hand, the contraction of the dilator muscles is driven sympathetically through a tri-synaptic pathway: the first-order neuron starts in the hypothalamus and descend to the ciliospinal centre of Budge; the second-order, pre-ganglionic sympathetic neuron exits the spinal cord and ascend to the superior cervical ganglion; the third-order post-ganglionic neurons enter the orbit upon the short and long ciliary nerve and finally synapse the dilator muscles [36]. The very different nature of the two neural pathways leading to pupil constriction and pupil dilation underlies the idea that pupil size fluctuations reflect the ongoing dynamics of fundamentally different processes. From one side, we have the simpler, parasympathetic modulation of pupil diameter as a function of the current retinal output, responsible of the pupillary light reflex (PLR) and the pupil near response. On the other side, the sympathetic modulation of pupil dilation, reflects more complex fluctuations of the internal brain states. For example, it has been widely shown that pupil dilation correlates remarkably with arousal, locomotion and behavioural engagement [37–40].

### 1.2.2. The Pupillary Light Reflex

As the light falls on the retina, the RGCs activity propagates along the optic nerve to the optic chiasma. At the chiasma, the information coming from the two eyes combines and reorganizes, before getting projected to the pretectal nucleus (PN): similarly to what happens to the information flowing through the image-forming pathway, the information coming from the nasal portion of the retina is projected contralaterally to the PN of opposite hemisphere, while the information coming from the temporal part is sent to the ipsilateral PN. From the PN, information is sent to the Edinger-Westphal nucleus (EWN). Each EWN receives input from both the ipsilateral and contralateral PN, merging the information coming from the monocular and binocular visual fields of both eyes. At this point, the activity of the EWN neurons drives the Oculomotor Nerve (III), which in turns passes to information to the ciliary ganglion (CG) in the same hemisphere. The CG innervates and provides cholinergic input to the iris sphincter muscles, causing its contraction and the subsequent constriction of the pupil. The pupillary light reflex (PLR) is the process which, thanks to the neural pathway described above, leads to the constriction of pupil in response to brightness and the dilation in response to darkness. Notably, as the EWNs both receive information coming from both eyes, the PLR is a consensual reflex, meaning that the increase of light detected by one eye (irrespectively of whether it happened in the monocular or binocular portion of the field of view) leads to the activation of both EWNs, thus causing the pupil constriction to happen in both eyes. The PLR is driven by all the known types of photoreceptors, which include rods, cones and intrinsically-photosensitive RGCs (ipRGCs). Due to the different kinetics of their response to light increase, different photoreceptors contribute differently to the PLR. Particularly, cones and rods are characterized by fast and transient response to light, and are crucial for driving the initial phase of the pupillary constriction. However, the response generated by these photoreceptors is also transient, and quickly adapt during prolonged light stimulation. Complementary, the ipRGCs show an opposite trend, with a slow-rising, sustained activity in response to sudden luminance increase, which make them responsible for keeping the pupil constricted during prolonged exposure to bright light [41].

Functionally, there are different hypothesis on how the PLR could help improving visual perception. One of the most accepted concerns the balance between visual sensitivity and visual acuity [42]. The benefit of a dilated pupil is quite intuitive: the larger the pupil aperture is, the more light can reach the retina. This allows the visual system to collect and process more information about the visual scene compared to a constricted pupil scenario, helping the detection of faint stimuli [43]. Consequently, pupil dilation helps with visual perception in dim light condition by lowering the amount of dark adaptation that would be required by the photoreceptors if the pupil was constricted. Beside increasing the amount of light collected and decreasing the amount of dark adaptation needed, however, pupil dilation can also negatively impact the quality of visual perception. The reason is because an increase in the amount of light passing through the lens determines a loss of image contrast due to optical aberrations and diffraction, thus limiting visual acuity and the resolution of the retinal image [35]. For this reason, a smaller pupil size allows to see sharply across a wide range of distances by increasing the depth of field.

The dynamic control that the visual system is able to exert on the pupil aperture is then essential for balancing how much (sensitivity) versus how well (acuity) one can see, as well as assisting and optimizing the dark adaptation process. This becomes particularly relevant if we consider how much and how rapidly the overall luminance and the contrast of the visual scene can vary in a natural environment. In the context of the visual system as a whole, the PLR can therefore be viewed as an early, state-sensitive mechanism that shapes visual perception by controlling the flow of photons into the eye.

### 1.2.3. State-dependent pupillary dynamics

In addition to luminance-driven constriction controlled by the constriction pathway, pupil size is also strongly modulated by internal brain states, exhibiting transient or sustained dilation independently of changes in the ambient light.

Such state-dependent pupillary dynamics directly reflect the engagement of the neural pathway controlling pupil dilation, which, in contrast to the constriction pathway described above, is not directly driven by luminance changes. Instead, pupil dilation is driven by sympathetic and

neuromodulatory systems that are tightly linked to the global brain state. This makes the dynamics of pupil dilation a convenient proxy for arousal, attention and behavioural engagement [37,39,40,44].

Pupil dilation is mediated by activation of the iris dilator muscle via a multisynaptic sympathetic pathway originating in hypothalamus and locus coeruleus (LC). Both structures projects to the intermedio-lateral column of the spinal cord (IML), from which preganglionic sympathetic neurons project to the superior cervical ganglion. Postganglionic fibres then innervate the iris dilator muscle, leading to pupil enlargement.

The LC is a small brainstem nucleus which constitutes the primary source of noradrenaline in the brain. This area is particularly active when an organism is awake and attentive, which means that the level of activity of the LC closely relates to the level of arousal [37,45]. Particularly, phasic LC activity is associated with transient pupil dilation during task engagement and attentional shifts, while tonic LC activity is associated with baseline pupil size and arousal level. Moreover, manipulations of LC activity modulate pupil diameter, supporting a direct functional link between noradrenergic signalling and state-dependent pupil dynamics [40]. Similarly, in the context of pupil dilation, the hypothalamus also reflects the overall level of wakefulness and arousal.

Beyond noradrenaline, other neuromodulatory systems seems to be associated, either directly or indirectly, with the sympathetic pathway controlling pupil dilation. Activity in the cholinergic axonal projection recorded in L1 of V1 and A1, for example, was shown to correlate well with the pupil dynamics during periods of locomotion [46]. Optogenetic activation of serotonergic neurons in the dorsal raphe nucleus (DRN) was also shown to induce transient pupil dilation, revealing a tight relationship between phasic activation of 5-HT neurons and pupil size, consistent with a role of serotonin in regulating arousal and affective state [47]. Dopaminergic systems have also been indirectly linked with pupil dilation, where the time course of pupil size correlated with risk prediction error during decision making tasks, suggesting a tight interplay between pupil dilation, the noradrenergic and the dopaminergic system [48].

As a consequence of these interactions, pupil size covaries with behavioural engagement, locomotion, attention, and task performance. In mice, pupil dilation strongly correlates with locomotion and arousal fluctuations, even under constant illumination, as well as with changes in cortical state and sensory responsiveness [28]. In humans and non-human primates, pupil diameter tracks attentional effort and cognitive load, reflecting a role of the neuromodulatory resources in controlling higher cognitive functions [43]. These findings support the idea that the dynamics of pupillary dilation provide a convenient readout on the global, brain-wide states fluctuations.

Importantly, luminance-independent fluctuations in the pupil size could not be merely epiphenomenal, as they directly alter the amount of light entering the eye. Such modulation could affect the adaptation state of the retina, as well as shaping the RGCs activity, thus modulating the visual information transmitted to the LGN and the visual cortex. Through this mechanism, the neuromodulatory systems could also indirectly impact sensory processing by modulating the sensory input itself, other than shaping the higher-order, thalamic and cortical processing of the visual information.

# 1.3. The role of internal states in shaping vision

## 1.3.1. Overview

As we mentioned above, neural activity in the cortical regions, but in fact all over the brain, is constantly varying and fluctuating across different states. This makes the sensory representations that the brain generates, i.e. the spatial and temporal patterns of neural activity encoding the current state of the world, to be extremely susceptible to the spontaneous dynamics of such latent process. In cortical areas, internal states have been shown to modulate the baseline activity of neuronal populations, as well as to alter the excitability, synaptic integration, and response gain of individual neurons. Traditionally, cortical states have been mainly characterized in the context of sleep cycles. For example, enrichment in the low-frequency components of the EEG spectrum observed during the non-REM sleep is generally associated with a synchronized cortical state, where all neurons oscillate together between "up" and "down" phases. On the other end, during REM sleep as well as during wake, the activity of the cortical populations is more desynchronized, with individual neurons showing less correlated neural activity [49]. However, growing evidence in recent years have shown that also during wakefulness the cortical state is far from stationary. Attentive and engaged animals showed more desynchronized cortical activity than quiescent animals, which in turn are characterized by spontaneous oscillatory cortical activity reminiscent of the one observed during slow-wave sleep [50].

In alert or engaged states, cortical neurons are typically depolarized and show increased gain and reliability of sensory responses, whereas synchronized or quiescent states promote large fluctuations, burst firing, and stronger coupling to ongoing population activity. This shows how brain state fluctuations can drastically influence shared variability, correlation structure, and representational geometry of a neuronal population. From a computational and efficient coding perspective, heterogeneity in neural activity and low noise correlations are associated with increased representational capacity and better performance in cognitive tasks [51]. This is because a less correlated neuronal population is generally characterized by higher degrees of freedom and higher dimensionality, allowing for richer neural patterns to emerge and thus for more complex information to be encoded [52,53]. Conversely, synchronized states emphasize internally generated

dynamics that can dominate sensory responses, effectively constraining the dimensionality of population activity.

Brain states fluctuate on relatively slow (seconds) timescales, much slower than the usual timescales of sensory processing. Such slow, global fluctuations are closely linked to the phasic activity of neuromodulatory systems, particularly noradrenergic, cholinergic, serotonergic inputs, which can globally regulate membrane conductances, synaptic efficacy, and the balance between excitation and inhibition [37,50]. Noradrenergic projections from the locus coeruleus modulate cortical gain, signal-to-noise ratio, and response reliability, with experimental work proposing that noradrenaline enhances sensory-evoked responses while suppressing stimulus-unrelated background activity [37]. Cholinergic input from the basal forebrain to cortical visual areas has been shown to increase overall responsiveness and to sharpen stimulus selectivity [54,55].

Typically, the activation of these two neuromodulatory systems is associated with two distinct yet often correlated components of brain states: arousal and motor activity. As mentioned above, it is often convenient and surprisingly accurate to operationalize arousal with a unidimensional measure of pupil size [56]. Analogously, overall motor activity can be conveniently operationalized with locomotion velocity, even though more subtle motor activity associated, for example, with orofacial movement has been shown to strongly impact the geometry of spontaneous population activity in V1[57].

### 1.3.2. Arousal and Locomotion

Arousal and locomotion represent two closely related but partially dissociable internal states that exert profound influence on visual cortical activity. In rodents, these states are generally associated with stereotyped changes in global brain dynamics, neuromodulatory tone, and behavioural engagement, making them powerful experimental handles for studying state-dependent cortical computation. Over the past decade, a growing amount of work has established that transitions between quiescence and heightened arousal or locomotion fundamentally reshape both spontaneous and sensory-evoked activity in primary visual cortex (V1), with consequences that extend from single-neuron response properties to population-level coding and information transmission [51,28,38,58–60].

Mechanistically, the effects of arousal and locomotion on V1 are mediated by interactions between neuromodulatory systems and local cortical circuitry. Cholinergic input from the basal forebrain has been shown to play a central role in locomotion-related modulation of visual responses, in part by engaging disinhibitory circuits involving VIP interneurons that suppress SST-mediated dendritic inhibition of pyramidal cells [27,61]. Noradrenergic input from the locus coeruleus further contributes to gain modulation and decorrelation of population activity, during arousal and behavioural engagement [37,60]. These neuromodulatory effects are layer- and cell-type specific, leading to differential modulation of feedforward, recurrent, and feedback pathways within V1.

As mentioned in the above paragraph, one of the main effects of arousal-related neuromodulation of cortical populations is the decupling of individual neurons' activity from global, stimulus-unrelated, shared modes (such as slow waves oscillations during quiescence), which translate in a more heterogeneous population activity. The reduction in the overall neural coherence attributed to noradrenergic (arousal) and cholinergic (locomotion) modulation of V1 has been shown to decrease the noise correlations and trial to trial variability, effectively increasing the signal to noise ratio and thus the response reliability [27,28,38,51,58]. Moreover, population recordings in mouse V1 have also revealed that the decorrelation of cortical activity observed during locomotion and arousal directly increases the dimensionality of population responses and enables a more effective representation of visual information [51,62]. Notably, these observations have been made specifically on trial-structured data, where the neural response to multiple repetitions of the same stimulus were used to estimate signal and noise components of the neural activity. Importantly, arousal and locomotion are not equivalent states, and their effects on visual processing can be dissociated. While locomotion reliably correlates with increased arousal in rodents, changes in pupil size and cortical state can occur in the absence of movement, indicating that arousal-related modulation can be decoupled from motor output [60,39,38]. Some studies have shown that pupil-indexed arousal better predicts changes in cortical variability and encoding fidelity than locomotion per se, suggesting that neuromodulatory state, rather than movement, is the primary driver of many observed effects [38]. This distinction is critical for interpreting state-dependent modulation in experimental settings and highlights the importance of separating behavioural correlates from underlying neural mechanisms.

On a different note, activity in sensory cortices (and particularly V1) was also studied in the context of spontaneous cortical states dynamics [28,57,63]. In this case, no sensory input directly drove the activity of the recorded neural populations, which in turns purely reflected internal states dynamics. Even in the absence of any sensory input, the activity of cortical populations is strongly driven both by arousal and by motor activity. In both cases, the timescales of these fluctuations are typically much slower than the timescales of sensory-driven activity [57], and strongly correlated with pupil size, locomotion and orofacial movements. The estimated dimensionality of this spontaneous activity largely depends also on the size and the cortical span of the recorded population: even if the dynamics of the internal state fluctuation might be low-dimensional - e.g. 'ON/OFF'-like dynamics for arousal state fluctuations [59] – it might also have different effects on different neural populations. If the neural activity was sampled simultaneously from distant cortical populations, the overall dimensionality of the recording is likely to be high dimensional, even if the latent, driving dynamics was relatively low-dimensional [57,62].

### 1.3.3. Models of behavioural-sensory integration

A central challenge in understanding state-dependent cortical computation is explaining how sensory inputs and non-sensory, state-dependent modulatory signals - such as arousal and locomotion - are combined to drive neural activity in cortical neurons. The observations that internal states can extensively reshape both the magnitude and the geometry of population activity regardless of if a sensory input is present or not, have motivated a range of conceptual and computational models, often framed in terms of additive and multiplicative components of neural responses.

In the simplest phenomenological description, neural activity is modelled as the sum of a stimulus-driven component and a state-dependent additive term. In this framework, internal state shifts the baseline firing rate independently of sensory input, effectively displacing neural activity along a low-dimensional state axis in population space. This additive model captures the observation that activity in sensory areas seems in be driven by internal states fluctuations also in the absence of any sensory stimulus. At the population level, additive state signals account for the large, coherent fluctuations in the activity baseline observed during arousal or locomotion, which dominate the neural variance [59,62]. However, purely additive models

struggle to explain why arousal and locomotion have often been associated with increased stimulus-evoked responses and improved sensory encoding[51].

An alternative and widely supported class of models posits that internal states interact with sensory responses primarily through multiplicative gain modulation. In these models, arousal scales stimulus-evoked activity without altering tuning properties, effectively amplifying or attenuating sensory signals [64]. Gain models are consistent with observations that locomotion and arousal induce multiplicative changes stimulus-evoked responses in V1 neurons [38,65]. At the population level, if the multiplicative factor of is reasonably constant across the all the neurons, the gain modulation can preserve the relative geometry of stimulus representations while increasing the gain of individual neurons' stimulus-specific responses, thereby enhancing discriminability. These models naturally account for improvements in signal-to-noise ratio and reduced trial-to-trial variability observed in high-arousal states.

However, such models mainly consider the effects of state-dependent modulation at the level individual neurons. In fact, no purely additive or multiplicative models seem to fully account for the effects that internal state dynamics seem to exert at the population level. Particularly, more complex and hybrid approaches have led to better models, able to reconcile observations such as modulation of the global operating point of the neural population, stimulus-dependent multiplicative gain fluctuations, spike counts decorrelations and reshape of the population's covariance structure [59,66]. Moreover, circuit-level implementations of these models emphasize the role of inhibitory interneurons and recurrent connectivity. Microcircuits characterized by disinhibitory motifs involving VIP, SST and PV interneurons provide mechanisms by which neuromodulation could modulate cortical activity [27,61]. For example, cholinergic activation of VIP interneurons can suppress the SST-mediated inhibition of pyramidal cells, potentially leading to both increase of stimulus-driven responses as well as spontaneous, tonic firing to end neural decorrelation. These circuit mechanisms naturally give rise to mixed additive and multiplicative effects at the level of single neurons while producing nonlinear changes at the population level.

# Chapter 2

## Pupillary-Light-Reflex shapes the neural activity throughout the image forming pathway

## 2.1. Abstract

To correct for varying light levels in the visual scene, retinal adaptation is assisted by the pupil, which contracts and dilates to modulate light entering the eye. Currently, such pupillary dynamics are thought to prevent global light changes from triggering neuronal activity in the retina. However, the ability for pupillary change to induce retinal activity has not been tested. We find that pupillary constriction from increased light, the pupillary light reflex (PLR), can drive strong responses in the retinal output neurons, the retinal ganglion cells (RGCs) *in vivo* in mice. The PLR drives neural activity simultaneously in both the ON and OFF channels, and pupil-driven activity is relayed to the visual cortex. Furthermore, the consensual PLR allows one eye to indirectly respond to luminance changes happening on the other eye, leading to a binocular response and binocular modulation during low-amplitude luminance changes. To test if pupil-induced activity is consciously perceived, we performed psychophysics on human volunteers, finding that full-field luminance changes can evoke a perceptual dimming consistent with PLR-induced responses in mice. Our findings thus uncover that pupillary dynamics can directly induce visual activity that is consciously detectable, suggesting a novel role for the pupil in encoding perceived ambient luminance.

# 2.2. Introduction

Vision begins with the capture of light and its conversion into neural signals by the retina, followed by extensive processing in the brain. Yet, regulation of the visual input occurs even before photons reach retinal photoreceptors. The pupil serves as a dynamic aperture that continuously adjusts the amount of incoming light according to ambient luminance, contrast, arousal, and cognitive demands[67–71]. In darkness, pupil dilation increases photon influx, whereas elevated luminance triggers constriction via the pupillary light reflex (PLR)[72,73]. This reflex is thought to stabilize photoreceptor responses under global luminance shifts[74,75], thereby preserving the retina's ability to encode spatially localized luminance variations that define visual features[76–78]. In addition, a constricted pupil under bright conditions is predicted to improve optical quality by enhancing contrast and minimizing blur, as light passes preferentially through the central portion of the lens, reducing peripheral aberration and scatter[79–81]. Nevertheless, even in daylight the pupil does not remain maximally constricted. Instead, it exhibits ongoing, complex fluctuations in size[82–84], with the function of such pupillary dynamics remaining unclear.

Although PLR-mediated constriction can reduce retinal illumination by up to an order of magnitude, such changes have generally been considered to exert negligible influence on retinal output[79,85–87]. Here, we challenged this assumption by asking whether natural pupillary dynamics might directly shape retinal activity through transient alterations in the total light flux entering the eye. We specifically hypothesized that during daylight visual stimulation, PLR-driven constriction could produce a rapid drop in retinal luminance. This abrupt decrease would be expected to enhance activity in the OFF pathway while simultaneously reducing activity in the ON pathway.

The PLR is controlled by a subcortical circuit that integrates luminance signals from both eyes, giving rise to a consensual response: illumination of one eye leads to bilateral pupil constriction[87–90]. Additionally, binocular stimulation leads to increased pupil constriction compared to monocular stimulation[89]. If these pupil-driven luminance transients influence retinal output, they would introduce a form of binocularity at the retinal level that has not previously been described[90]. The retina is classically regarded as a monocular structure, and to our knowledge, binocular responses have not been reported in retinal

ganglion cells (RGCs), the output cells of the retina. By contrast, binocular integration is well documented in downstream visual structures where monocular inputs converge, such as the primary visual cortex (V1) and the dorsal lateral geniculate nucleus (dLGN). In these areas, neurons are defined as binocularly responsive when each eye independently evokes activity, and as binocularly modulated when one eye drives a response that can be enhanced or suppressed by stimulation of the other eye[91,92]. Should the PLR lead to retinal activity, we predicted that the following binocular phenomena should also be seen in RGCs: 1) Stimulation of one eye would shape visual information on the other eye via the consensual PLR, consequently driving retinal activity. Such retinal neurons would, by definition, thus exhibit binocular responses. 2) Stimulation of both eyes would lead to larger constriction than stimulating only one eye and, consequently, a larger luminance transient. Retinal neurons would thus exhibit binocular modulation. Finding these two types of responses would imply that the consensual pupillary response induces a non-canonical form of binocularity already at the retina. Importantly, not all retinal outputs necessarily reach conscious perception. Certain retinal signals are compensated for or suppressed at later processing stages. For example, saccadic eye movements generate pronounced retinal activity, yet these signals are not observed in visual cortex or higher areas because corollary discharge mechanisms suppress motion-related responses[93,94]. By analogy, activity induced by PLR-mediated luminance changes might also be attenuated in cortex or downstream structures. Therefore, it is important to determine not only whether such signals arise in the retina, but also whether they propagate to cortical areas and ultimately contribute to conscious visual experience.

To test whether pupillary constriction can induce monocular and binocular retinal activity, we performed head-fixed *in vivo* calcium imaging of RGC axons in the dLGN. We indeed found that the PLR can induce monocular and binocular retinal responses, that pupil-mediated activity is strong, and consistently in both the OFF and ON channels. Binocular RGC responses mediated by pupil dynamics were amplified through the interaction of direct and consensual PLR when stimuli were presented to both eyes. Furthermore, we found that PLR-induced responses are detectable in the LGN axons projecting to V1 and neurons in layer 2/3 of V1. Lastly, changes in luminance consistent with PLR-induced RGC activity are detectable in humans, suggesting such non-canonical retinal stimulation is accessible to conscious perception.

# 2.3. Results

## 2.3.1. Recording retinal activity from RGC boutons in the dLGN

To detect visually-evoked activity in the RGC axons in the dLGN *in vivo*, we injected an RGC-specific AAV[95] expressing GCaMP into a single eye (the right eye), then performed a craniotomy to access the dorsal surface of the left dLGN with 2-photon microscopy (Fig. 1.1A). This allowed for calcium imaging of dLGN-projecting RGCs axons (Fig. 1.1A-C) in anesthetized and awake mice[96,97], with all recordings in subsequent figures being anesthetized unless mentioned they are in awake. We presented visual stimulation on two curved screens with a custom-made separator between the eyes, allowing for independent stimulation of either the left (ipsilateral to imaged dLGN) or right (contralateral, GCaMP expressing) eye. The mice were first adapted to a grey background to both eyes. Next, we presented a series of full-field stimuli to either eye or both eyes in a pseudo-randomized order. Importantly, the non-stimulated eye received constant background stimulation.

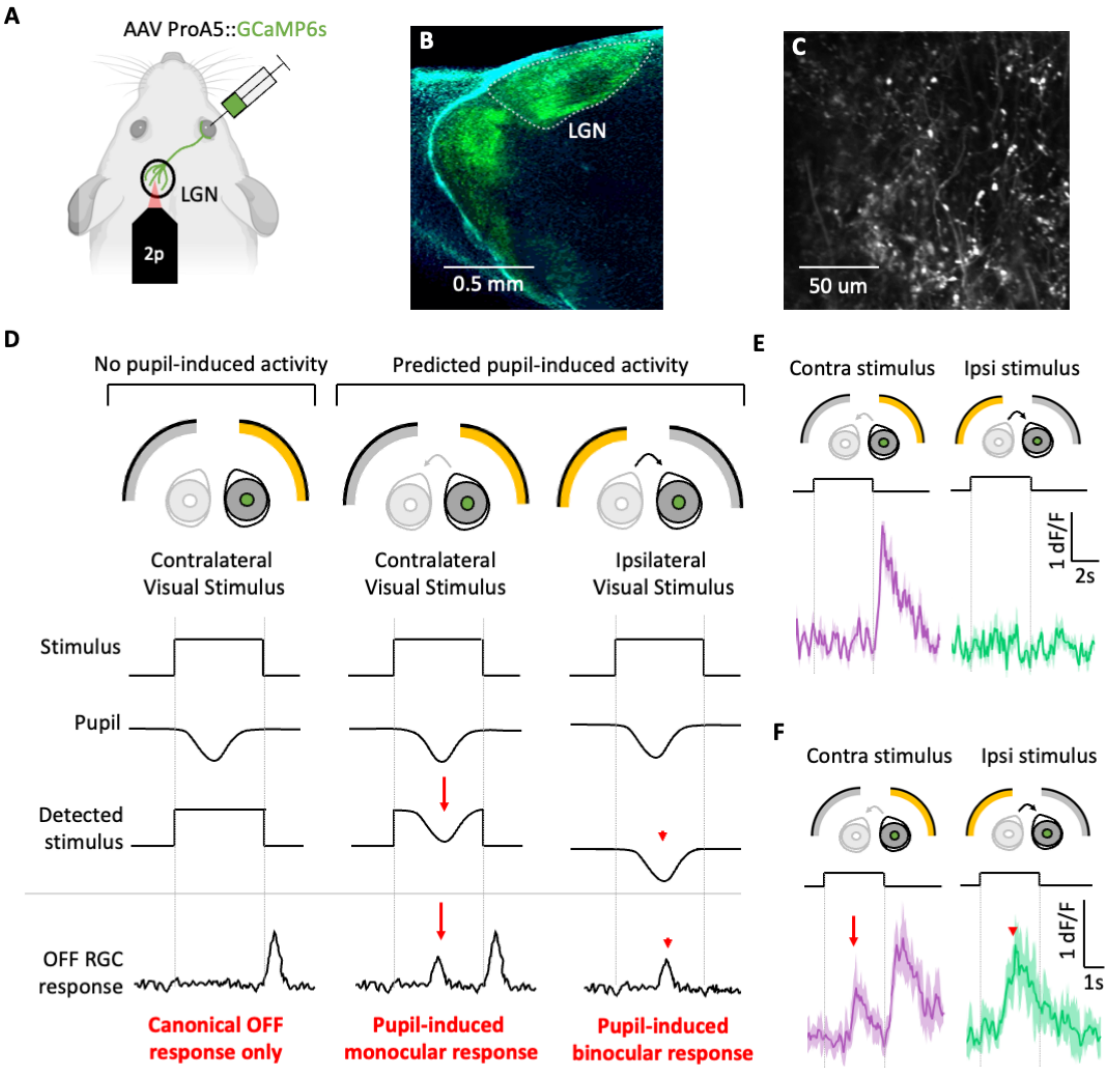


***Figure 2.1. Pupillary constriction's predicted monocular and binocular responses in RGC axons in vivo, compared to canonical responses.***

*(**A**) Schematic of retinal AAV injection to label RGC axons in the dLGN for in vivo 2-photon imaging. (**B**) RGC axons in the dLGN (**C**), RGC boutons during 2-photon imaging. (**D**) Schematic of possible OFF cell responses: an OFF cell where pupillary constriction plays no role in the response, it only shows a canonical response at light offset to stimulus presented to the injected eye, from the screen contralateral to the recording site (left), an OFF cell exhibiting a predicted pupil-induced response from contralateral screen stimulus (middle, arrow), an OFF cell exhibiting a predicted pupil-induced binocular response to stimulating the non-injected eye from ipsilateral screen stimulus (right, arrowhead). (**E**) Example RGC activity showing canonical OFF response to contralateral eye stimulation (left) and no binocular response to ipsilateral eye stimulation (right), contralateral pupil responses to each stimulus in bottom. (F) Example RGC showing a response consistent with predicted pupil-induced monocular response to contralateral eye stimulation (left, arrow), as well as a binocular response to ipsilateral eye stimulation (right, arrowhead), contralateral pupil responses to each stimulus in bottom. All flashes are from a 9.5 Lux baseline to 31 Lux.*

### 2.3.2. Retinal responses to direct and consensual PLR-induced pupillary constriction

We predicted that pupillary constriction during the full-field stimulus presentation could drive visual responses by producing a negative luminance transient on the retina. These pupillary-driven visual responses would occur after the onset of the stimulus, but with a delay consistent with the dynamic of pupillary constriction (Fig. 1.1D). Both ON and OFF RGCs could respond to pupillary-driven luminance transient. However, the response characteristics of OFF RGCs would allow for easier separation of canonical and pupil-driven responses. While the canonical response of OFF RGCs occurs at the offset of a full-field flash (Fig. 1.1D left, Fig. 1.1E left), a PLR-driven response would occur during the stimulation onset (Fig. 1.1D middle, Fig. 1.1F left). As the PLR acts consensually, stimulation of the ipsilateral eye would also lead to constriction of the contralateral pupil and, therefore, to a pupil-driven visual response in the absence of direct stimulation (Fig. 1.1D right, Fig. 1.1F right). This would suggest that the retina can produce a non-canonical binocular response by leveraging the PLR. Importantly, since these binocular responses would ultimately be the result of the luminance transient on the non-stimulated eye induced by the consensual PLR, they would only occur if the non-stimulated eye is not in complete darkness, but rather viewing a constant background.

OFF RGC boutons in the dLGN responded to full field flashes presented to the contralateral (GCaMP expressing) eye with a canonical response to the offset of the visual stimulation (Fig 2.2A-F, A2.1). Additionally, a substantial number of OFF boutons exhibited a delayed response consistent with pupillary dynamics in both anesthetized (55.6% of OFF boutons (n=361/649 N=5 animals)) and awake animals (30.5% of OFF boutons (n=216/709 N=4 animals) (Fig 2.2A-H, magenta traces, S1D). ON boutons, on the other hand, showed a negative modulation of the response to contralateral stimulation during PLR (Fig A2.1A-B, n=693 boutons, N=5 animals). As predicted by the hypothesis of consensual PLR driving binocular responses, stimulation of the ipsilateral (non-recorded) eye led to a similarly delayed visual response during the flash in 45.9% of OFF RGCs (n=298/649 N=5 animals) (Fig 2.2A-F, green traces)

This binocular visual response driven by ipsilateral stimulation was substantial, reaching on average 64.2% of the maximal response to contralateral stimulation (0.79 dF/F and 1.23 dF/F, respectively). We refer to the non-canonical response component of OFF RGCs during the flash as the "non-canonical OFF response". ON boutons also exhibited, albeit weaker, responses to ipsilateral stimulation (Fig A2.1 A-C, A2.2). Pupillary constriction started 0.51± 0.16s after the onset of the stimulation, reaching peak constriction 1.74 ± 0.37s after stimulus onset (Fig 2.2G, A2.1E), correlating with the non-canonical RGCs responses (Fig 2.2I, A2.1F).p While the consensual PLR was generally weaker than direct PLR, the overall dynamics of constriction, both in terms of time to onset and time to peak was not significantly different (Fig 2.2G, A2.1E-F), as was previously reported[87]. We did, however, observe animal to animal variability in the strength of PLR likely due to the effect of anesthesia varying between animals, as has also been reported[98]. To demonstrate that both direct and binocular non-canonical OFF responses in OFF RGC boutons occur due to pupillary constriction, we pharmacologically blocked the PLR. Application of atropine to the contralateral eye kept the pupil fully dilated throughout the visual stimulation and carbachol kept it fully constricted (Fig A2.3A-C, n= 848 (atropine) 307 (carbachol) boutons, N=4 (atropine) 3 (carbachol) animals). The subsequent lack of pupillary dynamics successfully abolished both direct and binocular non-canonical OFF responses while keeping the canonical OFF responses intact (Fig 2.2I-K, A2.3D). Similar effects were observed in ON RGC boutons (Fig A2.2, n=71 boutons, N=5 animals). To rule out light contamination as a possible source of binocular activity, we inactivated the ipsilateral eye with intravitreal injection of TTX, preventing any action potential firing in RGCs of that injected eye. This inactivation would eliminate any binocular responses but not responses due to light contamination or direct PLR-induced activity. Indeed, we found that the binocular non-canonical OFF responses in OFF cells were entirely eliminated by TTX (Fig 2.2L, right trace, Fig 2.2M). Importantly, direct PLR-induced activity of the contralateral eye itself was maintained (Fig 2.2L, left trace, n=187 boutons, N=3 animals, Fig 2.2M), as expected for a purely monocular response mediated by the contralateral eye. Altogether, these data suggest that two non-canonical visual responses can be induced by the pupil in OFF RGCs: a monocular and binocular one, with less salient responses in ON cells. In addition, we performed correlation of spontaneous activity to determine how many boutons were from a single axon, and, consistent with previous work, found up to 6.5 boutons per axons, all statistical calculations corrected for this possible confound (Fig A2.4, Annex).

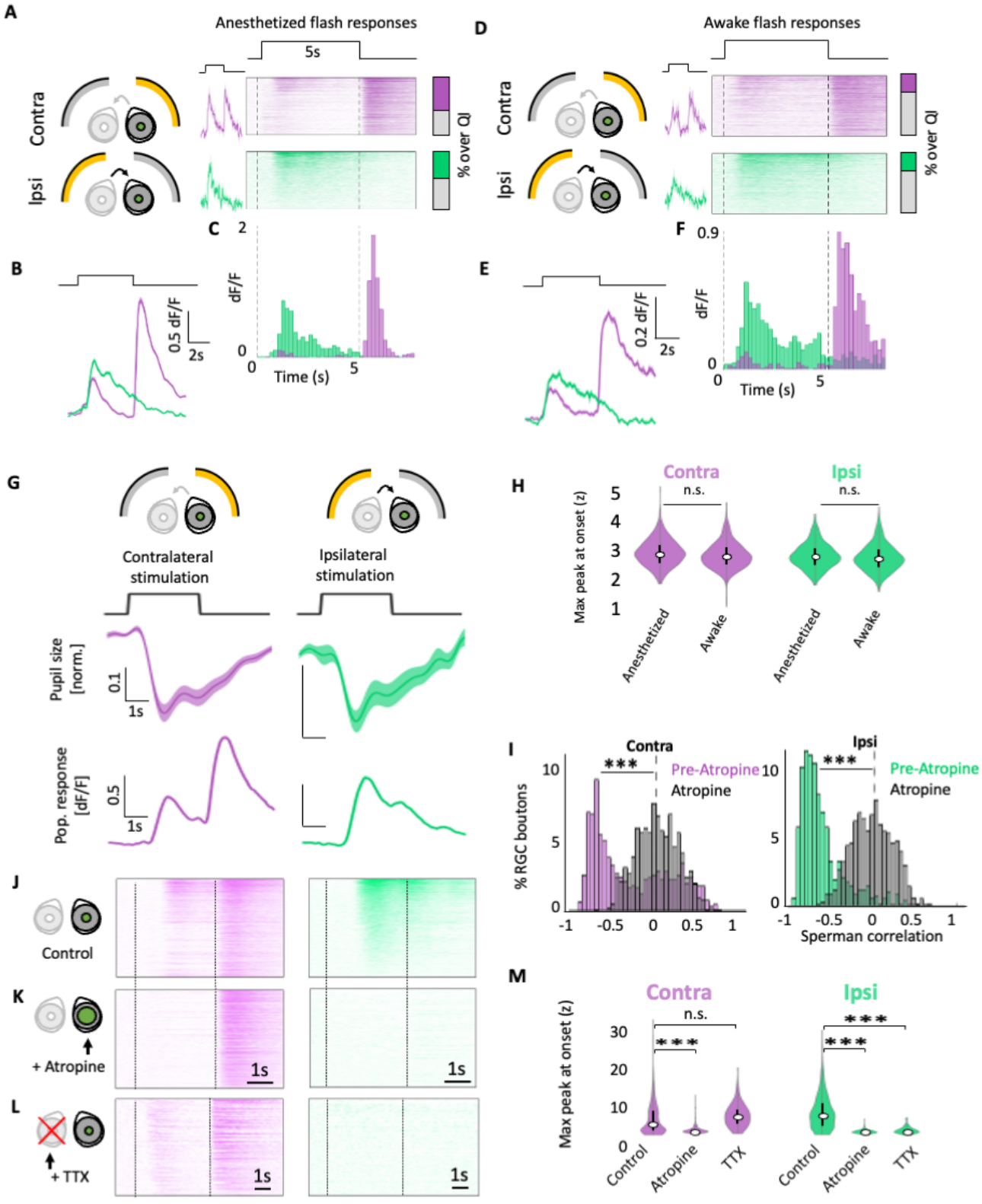
A
Anesthetized flash responses
5s
Contra
Ipsi
% over QI
D
Awake flash responses
B
0.5 dF/F
2s
C
dF/F
Time (s)
E
0.2 dF/F
F
G
Contralateral stimulation
Ipsilateral stimulation
Pupil size [norm.]
Pop. response [dF/F]
H
Contra
Ipsi
n.s.
Max peak at onset (z)
Anesthetized
Awake
I
% RGC boutons
Pre-Atropine
Atropine
Sperman correlation
J
Control
K
+ Atropine
L
+ TTX
M
Control
Atropine
TTX

***Figure 2.2. Binocular RGC activity is due to pupillary constriction.***
*(**A**) RGC responses to full-field flash stimulus to the contralateral (top) or ipsilateral eye (bottom) in anesthetized animals, for example response (middle) and heatmap of individual boutons (right). QI= quality index (see Methods) (n = 649 boutons N=5 animals). (**B**) Population average of heatmaps in A. (**C**) Histogram of responses in A. (**D**) Same as A, but for awake, freely moving RGC responses (n= 709 boutons, N=4 animals). (**E**) Population average of heatmaps in D. (**F**) Histogram of responses in D. (**G**) Pupillary constriction from full-field stimulus (middle) to either contralateral (left) or ipsilateral (right) stimulation, and RGC population responses in the same animals (bottom) (n=849 boutons, N=5 animals). (**H**) Peak non-canonical OFF responses (normalized, RMI) in anesthetized and awake animals to contralateral or ipsilateral stimulation (n=649, N=5 and n=709, N=4 respectively). (**I**) Spearman correlation between RGC activity and pupillary constriction due to contralateral (top) or ipsilateral (bottom) stimulation, before and after atropine. ***p <0.001 (two-sample Kolmogorov-Smirnov test) (n= 849 boutons, N=5 animals, n=848 boutons, N=4 animals, respectively) (**J**) Heatmap of RGC axons imaged in G. (**K**) RGC responses of boutons in G-I after administration of atropine to the contralateral eye, eliminating non-canonical OFF responses due to contralateral stimulation (left) and ipsilateral responses entirely (right). (**L**) Heatmap of RGC axons after TTX injection into the ipsilateral eye, seeing no change in contralateral activity, including the non-canonical OFF response (left), but completely eliminating ipsilateral responses (right) (n=187 boutons, N=3 animals). (**M**) Peak non-canonical OFF responses for contralateral (left) or ipsilateral (right) stimulation shown in I-K. ***p < 0.001 (2 sample t-test). Flashes are from a 9.5 Lux baseline to 65 Lux (A-E), or 31 Lux (G-M).*

### 2.3.3. PLR drives visual responses in all RGC cell types

Having established that binocular RGC responses arise exclusively from pupillary constriction, we leveraged ipsilateral stimulation as a tool to examine how distinct RGC types respond to the PLR. To functionally classify RGCs, we employed the full-field chirp stimulus, which has previously been shown to reliably differentiate retinal ganglion cell types[99] and presented it either to the contralateral (GCaMP-expressing) or to the ipsilateral eye.

RGC classification was based on responses to contralateral chirp stimulation. This analysis revealed five functional RGC classes (Fig 2.3A) with axons interspersed across the dLGN (Example field of view, Fig 2.3B). The identified groups comprised one transient OFF type, two sustained OFF types, one transient ON type, and one sustained ON type (Fig 2.3C, types 1-5, respectively n= 1492 boutons, N=3 animals). Stimulation of the ipsilateral eye elicited PLR-driven responses in each of the 5 RGC classes (Fig 2.3D). Consistent with the

temporal characteristics of pupil dynamics –specifically, that constriction occurs only after at least 0.51 s of continuous stimulation– the chirp stimulus elicited a PLR exclusively during the full-field flash epochs. Retinal responses during chirp (Fig 2.3D red arrowheads) similarly only occurred during prolonged (>0.51s) full-field flashes and not during fast-changing stimuli (Fig 2.3D, red dotted box).

To determine the types of responses driven by the consensual PLR, we next clustered the responding RGC boutons from Fig 2.3D based on their response to the chirp stimulus presented to the ipsilateral eye (Fig 2.3E). We found two types of PLR-driven responses: a delayed-transient ON response (Fig 2.3F top) and a delayed oscillating ON response (Fig 2.3F bottom). When further analyzing the temporal profile of PLR-driven responses (Fig 2.3G) we can observe that, as expected, response increase in OFF cells and decrease in activity in ON cells occurs during pupillary constriction (between 0.51s and 1.74s after the onset). Interestingly, some ON RGCs (especially transient ON RGCs), also responded with an increase in activity during rebound pupillary dilation after the PLR peak at 1.74s (Fig 2.3G, 3F insert zoom). This suggests that RGC visual responses can also be driven by different types of pupil modulation.

The two types of responses were also scattered across the field of view (example field of view in Fig 2.3H). The delayed-transient ON ipsilateral response was found to be present in the OFF RGC types (52.4%, 30.6%, and 47.2%, for types 1,2 and 3), while the oscillating response was present in the ON RGC types (13.3% and 40.4% for types 4 and 5) (Fig 2.3I). This demonstrates that PLR-driven binocular responses in RGC axons are present in all detected RGC types but qualitatively differ in ON versus OFF boutons, pointing to a global pupil-driven activation of the two channels.

***Figure 2.3. Pupil-induced RGC responses are present across RCG types.***

*(**A**) UMAP of 5 clusters of RGC responses to contralateral full-field chirp stimulus. (**B**) Example field of view, color coded with cluster identity. (**C**) Responses of RGC boutons to chirp presented to the contralateral eye, showing 3 OFF RGC and 2 ON RGC types. Top row is example RGC, bottom is population average (n= 1492 boutons, N=3 animals). (**D**) Responses of each RGC cluster in C to chirp presentation to the ipsilateral eye. Arrowheads= responses consistent with pupil-induced responses. Box = lack of activity in amplitude or frequency ramps (**E**) UMAP of 2 clusters of RGC ipsilateral responses to chirp stimulus in D. (**F**) Population responses of ipsilateral chirp responses: type 1 (middle) = a delayed ON response, type 2 (bottom) = a delayed OFF response followed by oscillating rebound. (**G**) Top: PLR phases during 3s Full field flash. For boutons in each RGC subclass: peak response time*

*(color) and suppressed response time (gray) to ipsilateral stimulation during the Full-Field-Flash section of chirp stimulation for each bouton passing response threshold (OFF RGC types: 1: peak=276, suppressed=3, 2: peak=137, suppressed=1, 3: peak=268, suppressed=0. ON RGC types: 1: peak=60, suppressed=7, 2: peak=61, suppressed=61). (**H**) Same example field of view as 2B, with 2 ipsilateral clusters color-coded based on ipsi cluster obtained in D-E. (**I**) Prevalence of each ipsilateral response in the 5 contralaterally-determined clusters, with type 1 overwhelmingly in OFF RGCs and type 2 in ON RGCs.*

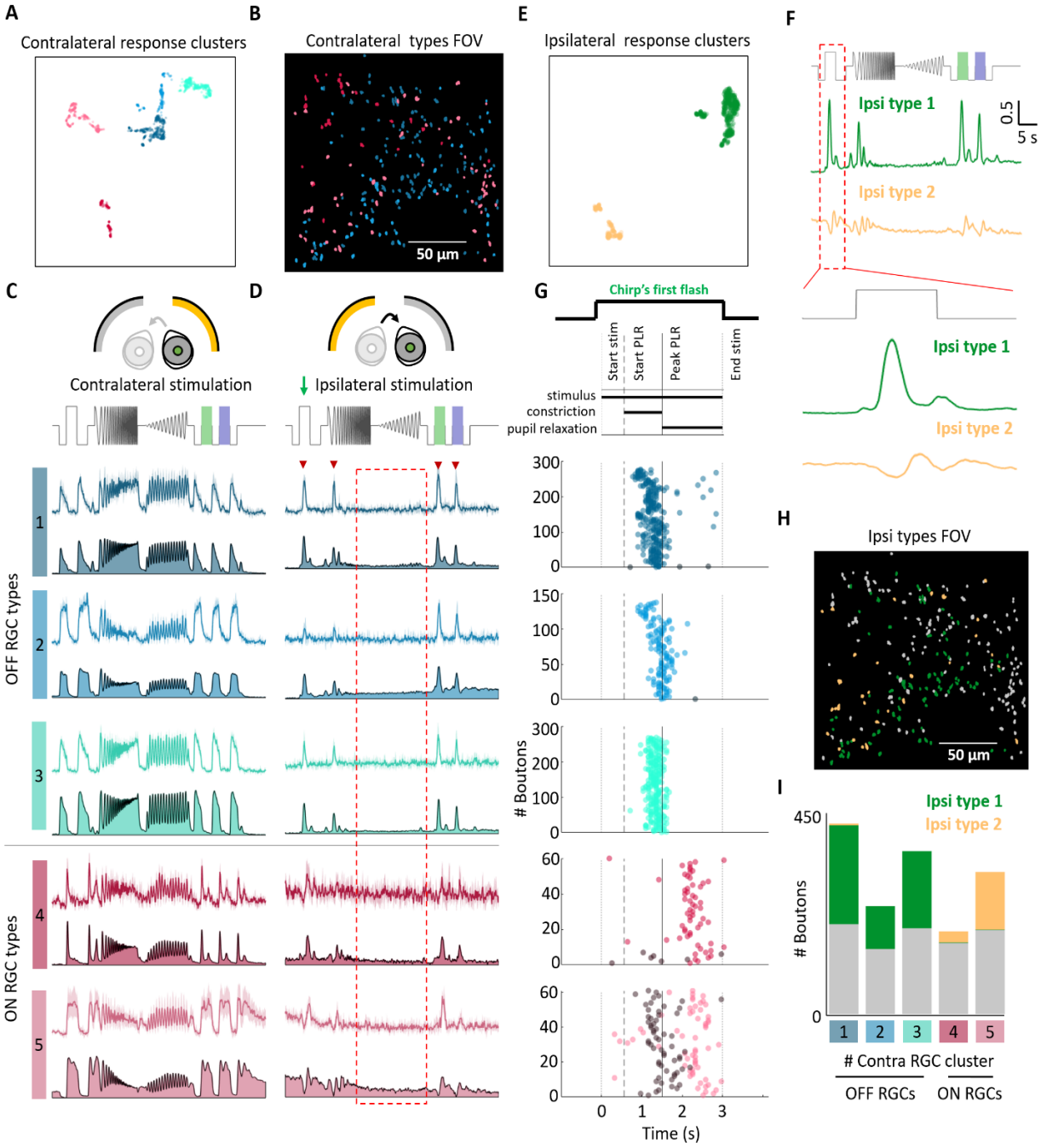

### 2.3.4. PLR-driven retinal activity is relayed to the visual cortex

Next, we wanted to show that the PLR-driven visual responses get relayed to the visual cortex. To do so, we injected an AAV expressing GCAMP8f into the dLGN (Fig 2.4A). We then recorded the activity of the dLGN axon terminals in the primary visual cortex (V1) in response to chirp and full-field flash stimulation of either the contralateral or ipsilateral eye (Fig 2.4B).

Unlike RGCs, dLGN neurons are known to receive inputs from both eyes [100–102]. However, previous work reported limited functional binocularity of the dLGN boutons in V1, with only 7% of boutons having strong binocular responses[103,104]. Due to their experimental conditions (with the opposite eye in the dark), their data would not detect PLR-induced binocularity. In contrast, when using a grey background to allow for PLR-driven responses, we show that 56.1% (48 out of 82, N=3) of dLGN boutons in V1 respond to full field flash presented to either eye (Fig 2.4A-E). Furthermore, responses to ipsilateral stimulation have characteristics comparable to those observed in PLR-driven responses in the RGC boutons. Namely, they occur during the stimulation with a characteristic delay after the onset of the stimulation (Fig 2.4E). Together, binocular response prevalence and characteristics suggest that dLGN boutons in V1 exhibit PLR-driven responses.

To check whether the signal recorded in the RGCs and dLGN boutons actually reached V1 neurons, we performed *in vivo* calcium imaging recordings of cell bodies in the monocular zone of layer 2/3 of V1 in awake animals (Fig 2.4F-G). A constant grey screen was placed in front of the contralateral eye and an LED was used to stimulate the ipsilateral eye, in order to specifically evoke PLR-driven responses. While full-field flash stimuli are notably less able to induce responses in V1 compared to the retina or LGN, we found a significant population of cells (n=150/250, N=2) that exhibited either positive or negative strong correlation with the pupil dynamics during the evoked PLR events (Fig 2.4H-M). The two population were clearly separated in the PCA space and showed response dynamics reminiscent of the ones we found in the OFF and ON RGCs populations. Particularly, the OFF responses (Fig 2.4I) presented the typical delay consistent with the PLR onset (Fig 2.4K) and

clearly correlated with the pupil constriction, whereas the ON cells were negatively modulated after the onset of the PLR and correlated with the pupil redilation following the PLR event. Overall, these data further support the previous findings in the dLGN boutons, suggesting that the PLR-driven retinal activity is relayed to the visual cortex.

***Figure 2.4. Pupil-induced RGC activity is relayed to the visual cortex.***

*(**A**) Experimental setup. 2-photon imaging of GCaMP8f expressing LGN axon terminals in V1. (**B**) Example field of view. (**C**) Responses of LGN neurons to full field visual stimulation of contralateral (violet) or ipsilateral (green) eye (n=82 boutons, N=3 animals). (**D**) Response quality index of responses during stimulation. Contralateral stimulation: mean=0.24, above response threshold (0.3): 18.3%. Ipsilateral stimulation: mean=0.31, above response threshold (0.3): 56.1%. (**E**) Response dynamics of LGN responses. Left: Population response of boutons to contralateral (purple) and ipsilateral (green) stimulation. Right: Time of peak response. Purple: the difference between stimulus offset and maximal response to contralateral stimulation. Green: the difference between stimulus onset and maximal response to ipsilateral stimulation. Red bad: time in histogram. (**F**) Experimental setup of 2-photon imaging of GCaMP8f expressing layer 2/3 neurons in V1. (**G**) Example field of view. (H) K-means clustering in PCA space of the average responses of all the cells that showed strong PLR-correlated activity in at least one trial (n=152 boutons, N=2 animals). The responses clustered into 2 groups: an OFF (green) and an ON (yellow). (**I,J**) top: examples of trial-averaged responses from one OFF (green) and one ON (yellow) cell. Black, vertical lines represent the beginning and the end of the ipsilaterally-presented LED flash. Shaded areas around the traces represent SEM error calculated over the trial responses; bottom: trial-averaged pupil area traces (z-score). Grey areas around the traces are ± SEM. (**K**) Histogram of the distribution of the delay of the response onset after the trial onset, for all the cells, color-coded according to the functional cluster (OFF green, ON yellow). (**L**) Average responses calculated over the correlated trials for all the cells (n=152, N=2). Back, vertical lines are the onset and the offset of the trial; the black dashed line the averaged pupil response, with the grey area are ± SEM. (**M**) Population average response for the two functional populations (OFF in green, ON in yellow), plotted together with the averaged pupil response (same as in L), all ± SEM. (**N**) Histogram of the percentage of the trial correlated with the pupil, calculated for all the cells recorded (n=250 boutons, N=2 animals)*

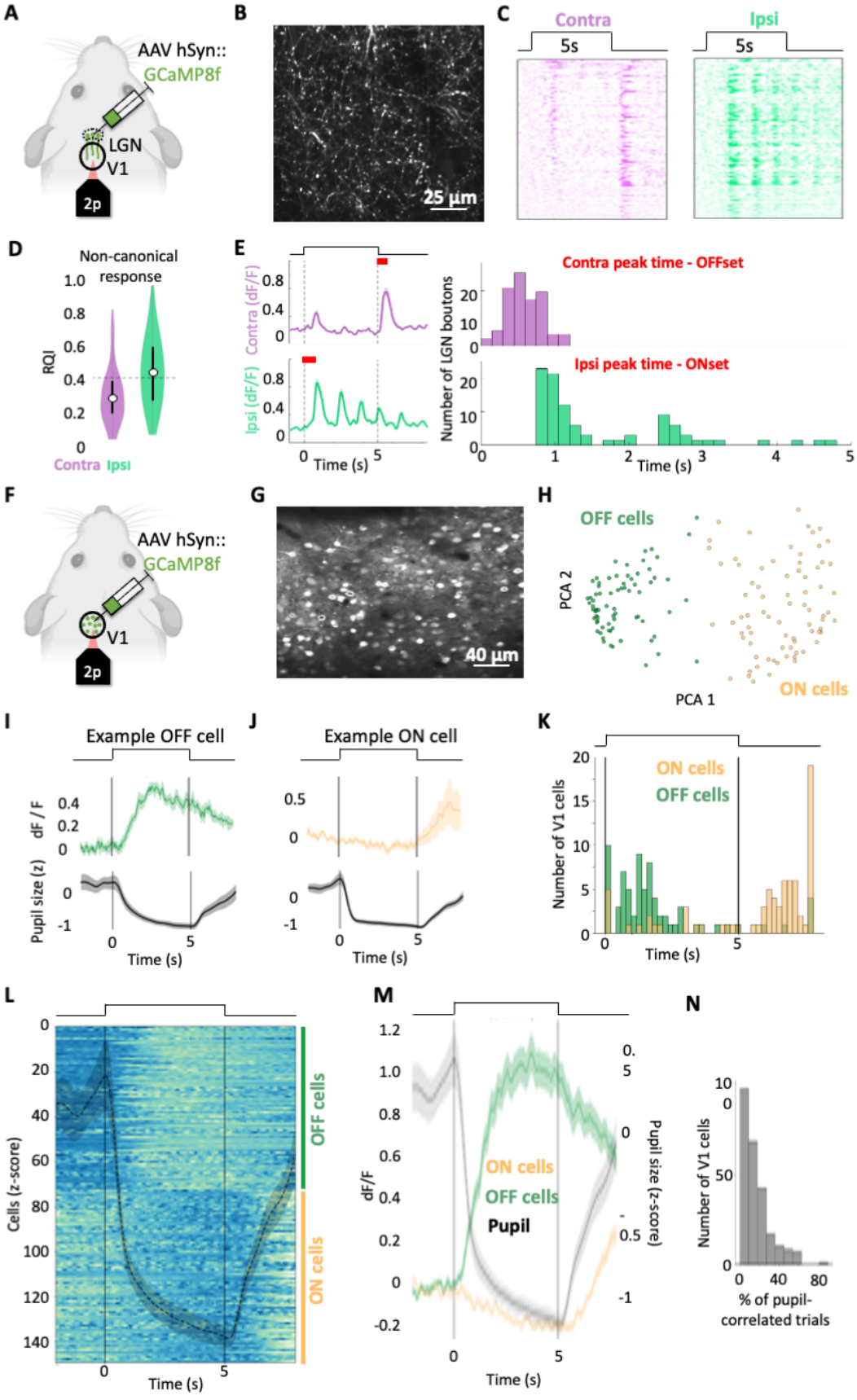
A
AAV hSyn::
GCaMP8f
LGN
V1
2p
B
25 µm
C
Contra
Ipsi
5s
5s
D
Non-canonical
response
RQI
Contra
Ipsi
E
Contra (dF/F)
Ipsi (dF/F)
Time (s)
Contra peak time - OFFset
Ipsi peak time - ONset
Number of LGN boutons
Time (s)
F
AAV hSyn::
GCaMP8f
V1
2p
G
40 µm
H
OFF cells
ON cells
PCA 2
PCA 1
I
Example OFF cell
dF / F
Pupil size (z)
Time (s)
J
Example ON cell
Time (s)
K
ON cells
OFF cells
Number of V1 cells
Time (s)
L
Cells (z-score)
OFF cells
ON cells
Time (s)
M
ON cells
OFF cells
Pupil
dF/F
Pupil size (z-score)
Time (s)
N
Number of V1 cells
% of pupil-
correlated trials

### 2.3.5. The consensual PLR response enables binocular facilitation at low contrast

Stimulation of either eye leads to constriction of both pupils and, therefore, to PLR-driven visual responses. Stimulating both eyes at the same time, however, has been shown to enhance pupillary constriction compared to stimulating only one eye[87–89]. We therefore predicted that stronger pupillary constriction following binocular stimulation could lead to potentiation of non-canonical, PLR-induced retinal responses. Since binocular stimulation is known to assist with the detection of low-contrast stimuli, a process known as binocular summation[105], we decided to probe the effect of binocular stimulation on the PLR-driven responses using low-contrast and high-contrast luminance changes. Binocular summation theoretically requires that the activity driven by both eyes during low contrast stimulation is boosted compared to the activity driven by the dominant eye alone. We asked whether the synergistic interplay between the direct and consensual PLR during stimulation of both eyes could potentiate the PLR-driven retinal responses to low contrast luminance changes (Fig 2.5A). We recorded RGC axonal activity while presenting either high- or low-contrast full-field flashes either to the contralateral eye or both eyes. We segmented 2 OFF and one ON functional populations. For the first OFF RGC type, the canonical response to the stimulus offset remained constant (Fig 2.5B-C red arrowhead). However, the PLR-induced component of the responses underwent significant binocular facilitation only during low contrast stimulation (Fig 2.5B-C red arrow, n= 287 (low contrast), 519 (high contrast) boutons, N=5 animals). While the amplitude of the effect was stronger in the population reported in Fig 2.5, both the OFF populations showed significant facilitation during the low-contrast luminance change stimulus. Furthermore, we observed increased contralateral pupillary constriction in response to stimulation of both eyes compared to the contralateral eye alone during low contrast (pupil facilitation index (PFI) = 0.16, p=0.005) but not high contrast stimulation (PFI =0.03, p=0.48) (Fig 2.5D top, N=5 animals). This pupillary constriction correlated with binocular facilitation (red arrow in Fig 2.5D bottom). Low contrast stimulation of both eyes led to facilitation in 46.3% of boutons, while only 3.2% were binocularly facilitated during high contrast stimulation (Fig A2.5E-F, n= 133/287 (low contrast), 17/519 (high contrast) boutons, N=5 animals). The described binocular facilitation was limited to OFF boutons, with ON boutons exhibiting comparable

responses to monocular and binocular stimulation. To confirm that low-contrast enhancement of activity was mediated by the PLR, we tested if this response could be eliminated with atropine or carbachol administration to the contralateral eye. This facilitation was indeed eliminated by both atropine and carbachol (red arrow in Fig 2.5E-F), including an elimination of the correlation between RGC activity and the pupil (Fig 2.5G).

We further tested if the response to both eyes could be explained by a simple addition of activity driven by the direct and consensual PLR alone (linear summation) or whether the facilitation was more than additive (supralinear summation). In low contrast stimulation, 40.4% of RGC boutons exhibited responses that were more than additive (Fig 2.5H left), compared to 0.4% during high contrast stimulation (Fig 2.5H right). These data show that: 1) increased pupillary constriction following binocular stimulation can lead to an increase in the PLR-driven visual responses, and 2) PLR-induced binocular facilitation disproportionately facilitates responses to low contrast, compared to high contrast luminance changes.

***Figure 2.5. Pupil-induced binocular modulation facilitates low contrast responses***.
*(**A**) Predicted pupil-induced response in RGCs to contralateral stimulation (Left) and both screen stimulation (Right), showing predicted pupil induced monocular response (Left) and predicted binocular facilitation (Right, arrow) in OFF RGC responses. (**B**) Example RGC bouton response to low (left) or high (right) contrast stimulation from the contralateral screen (Top) or both screens (Bottom). Arrow = site of pupil-induced binocular facilitation, Arrowhead = Canonical OFF response. (**C**) Heatmap (Top) of RGC difference between binocular and monocular responses (z-score), as well as population z-score average (Bottom trace) (n= 287 (low contrast), 519 (high contrast) boutons, N=5 animals). (**D**) Pupil response to contralateral (magenta) or both eye (yellow) stimulation (top) compared to population average of RGC activity (bottom). Arrow = presence of predicted binocular facilitation. (n= 287 (low contrast), 519 (high contrast) boutons, N=5 animals) (**E**) Same as in D, but after atropine administration to the contralateral eye, all binocular facilitation eliminated (arrow). (n= 218 (low contrast), 776 (high contrast) boutons, N=4 animals) (**F**) Same as in D, but after carbachol administration to the contralateral eye, also eliminating all binocular facilitation (arrow). (n= 133 (low contrast), 307 (high contrast) boutons, N=3 animals) (**G**) Spearman correlation between increased pupil contraction and binocular facilitation before (orange, green) and after (grey) atropine administration for low (Left) and high (Right) contrast, with RGC activity to low contrast being substantially correlated to pupil activity. ***p <0.001, *p < 0.05 (two-sample k-s test). (**H**) Plot of RGC activity during stimulation onset to both eye stimulation (y-axis) against the sum of responses to the individual screens (x-axis) for low contrast (Left) and high contrast (Right) (n= 287 (low contrast), 519 (high contrast) boutons, N=5 animals). Low contrast flashes are from a 9.5 Lux baseline to 20 Lux, high contrast from 9.5 Lux to 65 Lux.*

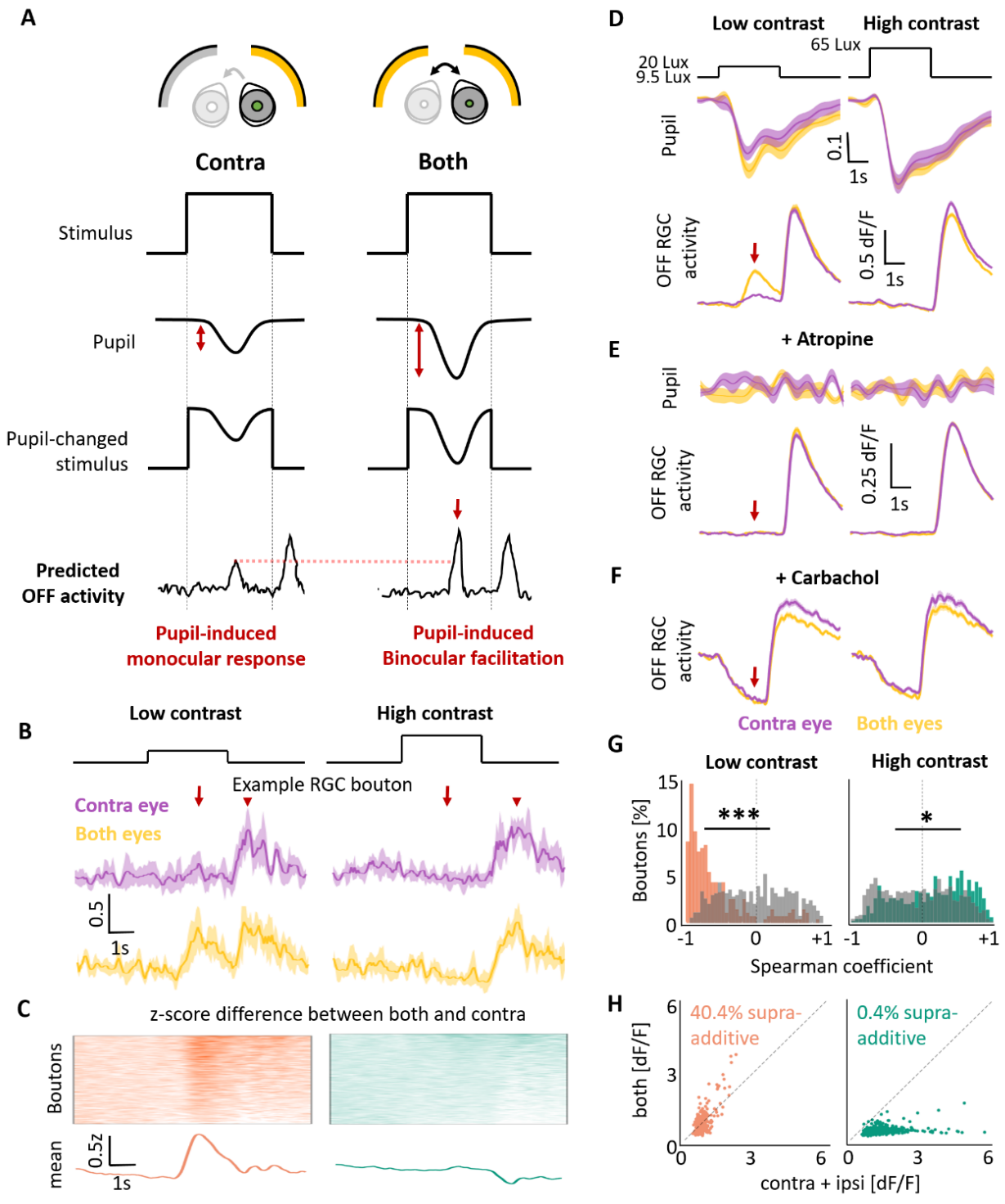
A
Contra
Both
Stimulus
Pupil
Pupil-changed stimulus
Predicted OFF activity
Pupil-induced monocular response
Pupil-induced Binocular facilitation
B
Low contrast
High contrast
Example RGC bouton
Contra eye
Both eyes
0.5
1s
C
z-score difference between both and contra
Boutons
mean
0.5z
1s
D
Low contrast
High contrast
20 Lux
9.5 Lux
65 Lux
Pupil
0.1
1s
OFF RGC activity
0.5 dF/F
1s
E
+ Atropine
Pupil
OFF RGC activity
0.25 dF/F
1s
F
+ Carbachol
OFF RGC activity
Contra eye
Both eyes
G
Low contrast
High contrast
Boutons [%]
15
10
5
0
***
*
-1
0
+1
Spearman coefficient
H
40.4% supra-additive
0.4% supra-additive
both [dF/F]
6
3
0
contra + ipsi [dF/F]

### 2.3.6. The dynamics of pupillary constriction constraint PLR-driven retinal activity

We proposed that a change in luminance on the retina due to PLR leads to visual responses in RGCs, and that the increased pupillary constriction following binocular facilitation leads to low contrast binocular facilitation. However, it is currently predicted that a smaller pupil itself could improve visual detection by reducing blur [79–81]. To decouple the two effects and show that a transient change in luminance leads to binocular facilitation, rather than a smaller final size of the pupil, we first relied on the temporal dynamics of pupillary constriction. As shown above, the pupil takes 0.51s to start constricting, with RGCs responding with a ~0.9s delay after the onset of the stimulation. Therefore, a sinusoidal full-field stimulus with temporal frequency slower than time to constriction onset (0.55Hz) would lead to a PLR at each response peak (Fig 2.6A left). However, the pupil would not follow a high-frequency stimulus presented at 2Hz. Rather, during high-frequency stimulus presentation, the pupil would gradually constrict throughout the stimulation (Fig 2.6A right)[86]. This way, the 2Hz contrast ramp would achieve a smaller pupil size, but not the fast luminance transients induced by the 0.55Hz contrast ramp. Should the pupillary dynamics and not merely the final state of the pupil be important for binocular facilitation, RGC responses would be facilitated when the pupil is able to track the signal (at 0.55Hz), but not when it cannot (at 2Hz). However, if the facilitation was only due to the final smaller pupil size, it should be present in both conditions. Using a sinusoidal, temporal contrast ramp stimulus, we found that the pupil was indeed able to track the luminance changes if the stimulus was presented at 0.55Hz (Fig 2.6B left). However, when the stimulus was presented at 2 Hz, the pupil constricted gradually throughout the stimulation, not following the luminance change of stimulus (Fig 2.6B right). OFF RGC boutons (n=1381 (0.55 Hz), n=648 (2Hz) boutons, N=5 (0.55 Hz), 3 (2Hz) animals) responded to contralaterally presented contrast ramp at both frequencies (Fig 2.6C, right). However, PLR-driven responses were only present when the slower, 0.55 Hz contrast ramp was shown to the ipsilateral eye (Fig 2.6D left). When stimulating the ipsilateral eye with a 2Hz contrast ramp, we observed no responses (Fig 2.6D right). Stimulation of both eyes increased final pupillary constriction compared to monocular stimulation both during the 0.55Hz contrast ramp and during the 2Hz contrast ramp in comparable amplitude (Fig 2.6E, p=0.26, see methods). However, only 0.55 Hz stimulus elicited binocular facilitation

of the RGC responses (Fig 2.6F), suggesting that a stronger pupillary transient, not a smaller final pupil size, is important for the facilitation of RGC response. This data confirms that fast luminance transients, such as those caused by the PLR, are necessary for pupil-driven visual responses. Therefore, pupil-driven activity from the PLR is not due to any effect of a smaller pupil compared to a bigger one, but a retinal response to a sharp luminance change.

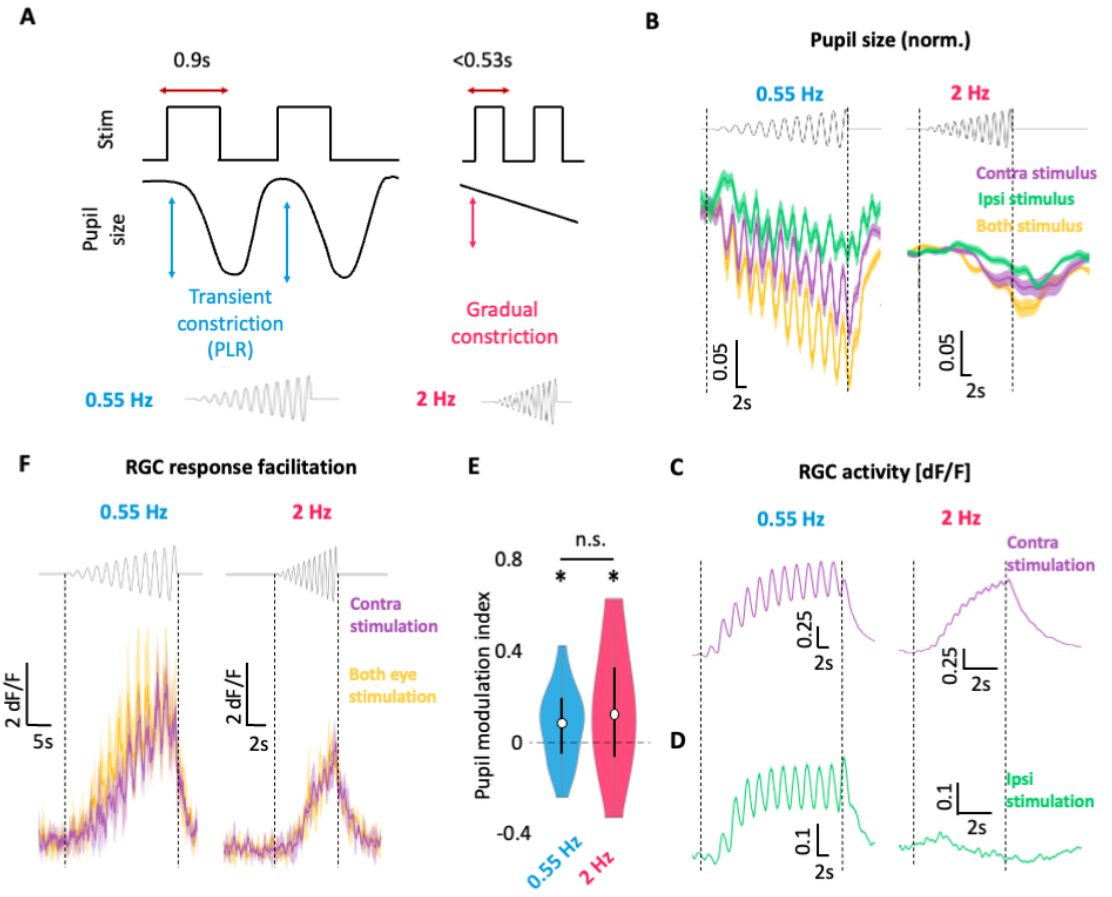


***Figure 2.6. The dynamics of pupillary constriction constrain PLR-driven RGC activity.***
*(**A**) Design of visual stimulus of increasing contrast that allows for the pupil to track each contrast change, by having the flashes presented at 0.55 Hz (left), compared to stimulus of identical properties, but presented at 2Hz (right). (**B**) Pupil size of the contralateral eye due to contralateral (magenta), ipsilateral (green), or both screen (yellow) stimulation at either 0.55Hz (left) or 2Hz (right). (N=5 (0.55 Hz) and 3 (2 Hz) animals). (**C-D**) Population RGC axon activity from 0.55Hz (left) or 2Hz (right) stimulation to either the contralateral (C) or ipsilateral (D) eye. (n= 1381 (0.55 Hz), 648 (2 Hz) boutons, N=9 (0.55 Hz), 5 (2 Hz) animals) (**E**) Increased pupillary constriction on both eyes compared to the contralateral eye for 0.55 or 2Hz amplitude ramp. n.s. (two sample t-test) (N=5 (0.55 Hz) and N=3 (2 Hz) animals, 6 repeats). (**F**) Example RGC axon activity when presented with 0.55Hz (left) or 2Hz (right) amplitude ramp, binocular facilitation (yellow trace greater than magenta) only observed at 0.55Hz.*

Binocular facilitation of boutons in Fig 2.6B-D during 0.55 Hz stimulation was strongest during the early, low-contrast part of the contrast ramp stimulus (mean RMI of 0.23 ± 0.01SEM at 3rd contrast step), with less facilitation present throughout the stimulation (mean RMI 0.1±0.004 SEM at 9th contrast step), consistent with the PLR-induced RGCs responses being preferentially potentiated by low contrast stimuli (Fig 2.7 A-B, middle, blue). This facilitation was entirely eliminated after the application of atropine (Fig 2.7A-B, bottom, gray). Binocular presentation of 2Hz stimulus failed to facilitate responses (Fig 2.7 A-B, top, red). We further examined low- and high-contrast binocular facilitation by comparing the change in RMI in individual boutons during low-contrast steps (peaks 2,3 and 4) and high-contrast steps (peaks 9,10,11) in anesthetized (Fig 2.7C) and awake mice (Fig 2.7D right, n=213 (0.55Hz), n=312 (2 Hz) boutons, N = 3 animals, top 50% modulated boutons for anesthetized condition). In both anesthetized and awake animals, responses to low contrast stimulation were more binocularly facilitated than responses to high contrast stimulation only during 0.55Hz contrast ramp (Fig 2.7C-E) Thus, RGC boutons exhibited binocular facilitation only for stimuli that the pupil constriction could track (0.55Hz), such binocular facilitation being enriched for low contrast stimulus. Additionally, we complemented the analysis of the binocular facilitation happening during the 0.55 Hz contrast ramp by characterizing the improvement in the signal to noise ratio (SNR). Previous work on human psychophysics found that binocular viewing increases low contrast detection by a factor of 1.4 (or $\sqrt{2}$), and in some cases by a factor of 2, a phenomenon termed binocular summation, which is predicted to occur at the first point of binocularity[87]. Since PLR-driven binocularity on the retina precedes thalamic or cortical binocular integration, we hypothesized that PLR-induced binocular detection could also improve the SNR by a factor of 1.4-2 compared to monocular detection. Interestingly, we found that the average increase in the SNR observed for the low-contrast portion of the stimulus reached value above 1.4 for a significant proportion of the recorded OFF boutons, with some responses reaching 2-fold improvement [106–108]. This amount of SNR improvement is consistent with the notion of active, supralinear summation of two signals (as also shown in Fig 2.5H) also reported in the literature of perceptual binocular summation.

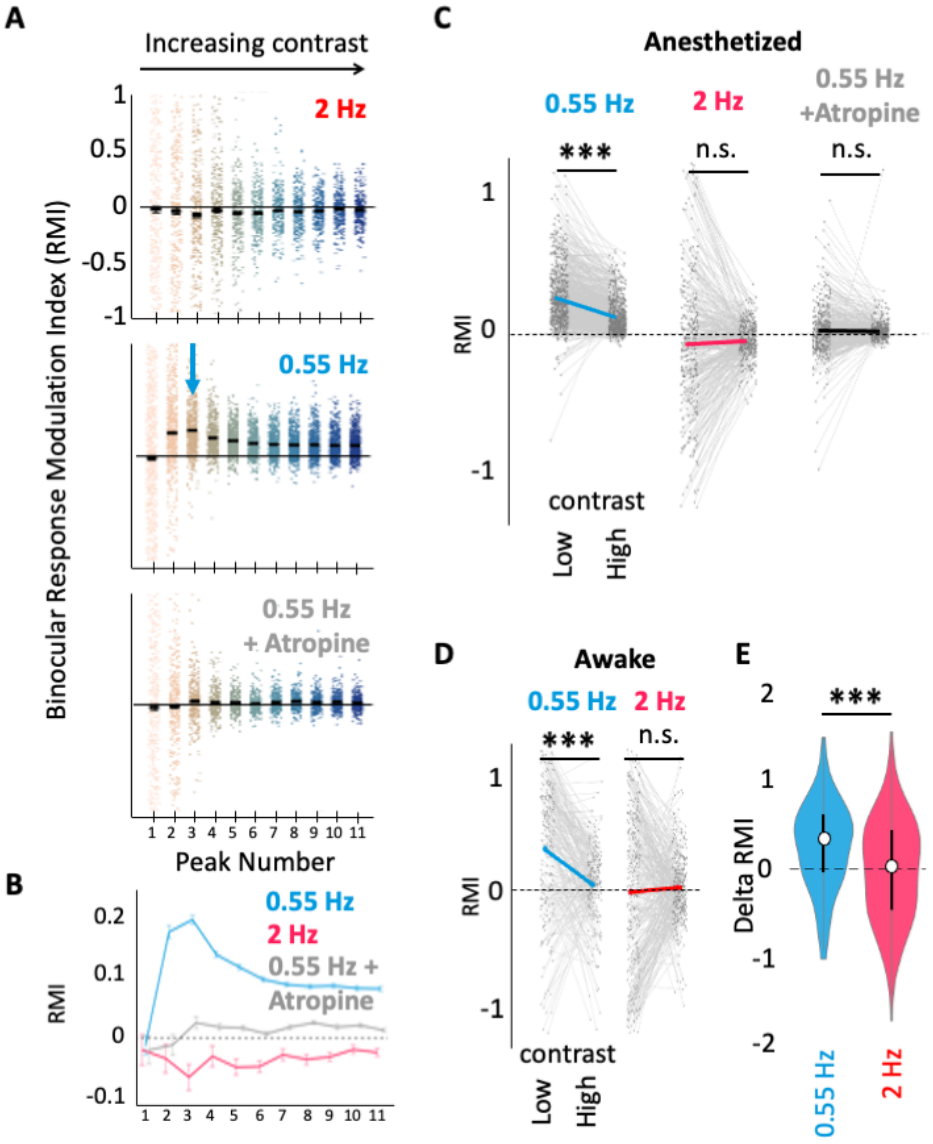


***Figure 2.7. Quantification of PLR-driven responses at different stimulus frequences.***
*(**A**) Binocular facilitation (RMI, see methods) for top 50% OFF RGC at each peak of the amplitude ramp at 2Hz (top), 0.55Hz (middle), or 0.55Hz after atropine administration. Arrow = peak binocular facilitation. (n=691 (0.55 Hz), 351 (0.55Hz+atropine), n=324 (2Hz). (**B**) Population means for A. (**C**-**D**) Paired binocular facilitation in individual boutons at low contrast (peaks 2,3,4) or high contrast (peaks 9, 10, 11) in (C) anesthetized, top 50% boutons (n= 691 (0.55 Hz), 351 (0.55Hz+atropine), 324 (2 Hz) boutons, N=5 (0.55 Hz), 4(0.55 Hz+atropine), 3(2Hz)) or (D) awake animals, all boutons . ***p <0.001 (paired t-test) (n= 213 (0.55 Hz), 312 (2Hz) boutons, N=4 animals). Thick colored line = population mean RMI difference. (**E**) Mean difference in total RMI at low contrast in D, comparing 0.55Hz stimulus to 2 Hz. ***p <0.001 (2-sample t-test).*

### 2.3.7. PLR-driven retinal activity can impact visual perception in humans

Since all monocular and binocular PLR-driven responses we found could be attributed to the dynamics of pupillary constriction, we examined if these dynamics are conserved between mice and humans. We found that the dynamics of PLR in response to a full field flash are comparable between mouse and human (Fig 2.8A). There was no significant difference between times of constriction onset (mouse=0.56s, human=0.55s, p=0.11) (Fig 2.8B left) but peak constriction was faster in human (mouse=1.56s, human=1.18s, p=0.0070) (Fig 2.8B right).

Furthermore, in humans, pupillary constriction was also able to track a sinusoidal contrast ramp at a 0.55Hz (Fig 2.8C right), but not at 2Hz (Fig 2.8C left). In both species, at 0.55 Hz the stimulus correlated with pupil dynamics, but at 2 Hz it did not (Fig 2.8D-E), meaning that both species share an optimal temporal frequency profile for pupil tracking of sinusoidal signal. This similarity in pupil constriction kinetics suggests that pupil-driven RGC responses may also be present in humans.

In order to understand whether the PLR-driven visual responses that we found throughout the visual circuit ultimately affects perception, we performed human psychophysics.

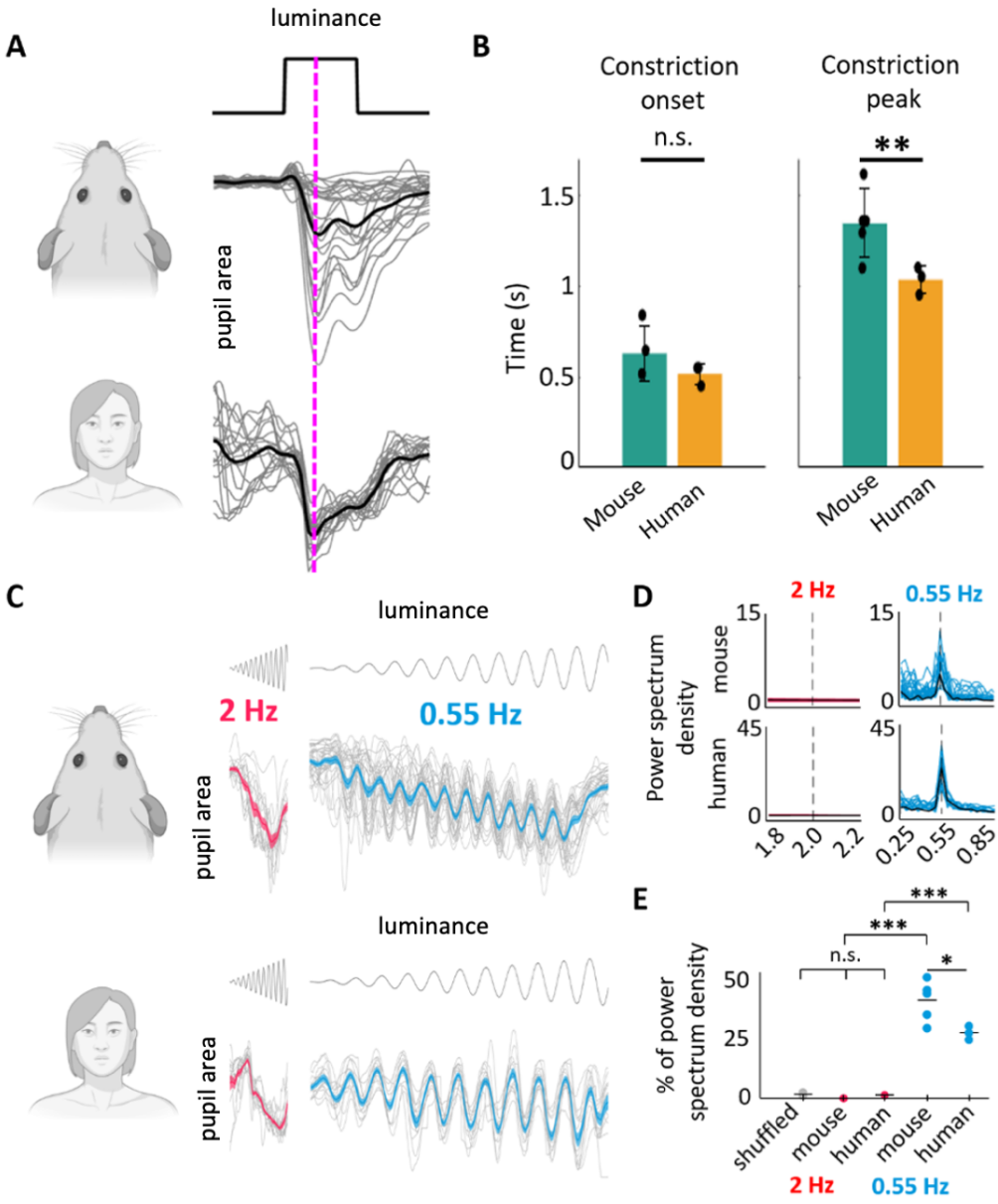


***Figure 2.8. Pupillary kinetics are conserved between the mouse and human.***

*(**A**) Averge pupillary response to 3-second full-field flash stimulus in mice (top, N = 5 animals) and human (bottom, N = 3 volunteers), the dotted line highlighting peak pupil response coincident with mouse delayed ON RGC responses (see Fig. 1.1-2). (**B**) Mean pupillary constriction onset (left) and peak of constriction (right) for data in A. **p <0.01 (t-test) (**C**) Average pupillary response to 2Hz (left) or 0.55Hz (right) stimulation in mice (top, N = 5 animals) and humans (bottom, N = 3 volunteers). (**D**) Fast Fourier Transform (FFT) of pupillometry data in C, showing no signal from the 2Hz stimulus centered on 2Hz (left), but a significant peak from the 0.55Hz stimulus centered on 0.55Hz (right). (**E**) Percent of the entire FFT signal (above 0.25Hz) at either 2Hz or 0.55Hz for those respective stimuli, for mouse and human. *p <0.05 ***p <0.001 (1-way ANOVA)*

Volunteers were placed in front of a curved screen and were presented with a sequence of 5-second long full-field increases in the monitor brightness from a grey baseline. The sequence of flashes was composed of a randomized combination of low or high-amplitude luminance steps comparable to ones we used for our mouse recordings (see methods). Prior to the test, the volunteers were informed that they would be presented with a sequence of luminance steps and that some of them would fluctuate in intensity after flash presentation, with a fluctuation happening at a random point during the 5-second long stimulus. In reality, the luminance was kept constant throughout the duration of the stimulus after flash presentation. They were asked to press a button as soon as they detected any change in luminance during the 5-second flash (Fig 2.9A). Remarkably, 7 out of 8 subjects reported the perception of a luminance change, namely a dimming, during uniform stimulation. This perceptual dimming would be consistent with our mouse data if it was seen more frequently with low contrast stimulation than at high contrast. Indeed, across the 8 volunteers this perceptual dimming was reported in 67.2% (43/64) of low contrast stimuli, but only in 26.6% (17/64) of high contrast stimuli (Fig 2.9B-D). This was a significantly greater ability to detect perceptual dimming of the stimulus at low contrast than at high (Fig 2.9E). Importantly, the time of reported perceptual dimming was 1.2 s (0.13 SEM) for high contrast, 1.1 s (0.06 SEM) for low contrast after the stimulus onset, aligning well with the peak of the PLR event (Fig 2.9F). Altogether, these data suggest that the PLR-driven retinal activity we found in mice is likely also present in humans. Furthermore, conscious detection of the PLR-driven activity suggests that this non-canonical retinal modulation plays a hitherto overlooked role in shaping conscious perception.

***Figure 2.9. Humans perceive luminance transient coinciding with pupil constriction.***
*(**A**) Stimulus setup. Top: Human subjects (4 male and 4 female) were viewing stimulus presented on computer screen and reporting perceived change in luminance during the 3-second flash. Middle: Stimulus. Full-field-flash of high contrast (corresponding to LL5 stimulus presented in mice) or low contrast (corresponding to LL1 stimulus presented in mice). Bottom: Prediction. We hypothesized that subjects would perceive dimming of the stimulus in time with PLR due to decreased luminance on the retina. (**B**) Examples of 2 subjects reporting perceptual dimming during low-contrast (orange) and*

*high-contrast (green) stimulus. Change in pupil size during stimulus presentation (dark gray: mean, light gray: repetitions). Dots: Time of perceived dimming. X: trials with no detected dimming. (**C**) Perceptual dimming in all volunteers. Top: Dimming detection during low-contrast stimulation. Time of dimming detection for each of the subjects (dots) and number of trials with no detection (X). The plot is the change in pupil size (line: mean, shaded area +-SEM). Bottom; Same as top, but for high-contrast stimulation. Blue line = 1 second. (**D**) Detection times shown in C (bottom histograms) aligned to pupil response (top traces). (**E**) Percentage of trials where dimming was detected during low contrast (orange) compared to high contrast (green) stimulation, n=8, p=0.013, paired t-test. (F) Difference between each dimming detection and PLR peak time during low-contrast stimulation for all the subjects. PLR start and end (dotted line) are approximated from mean PLR shown in C.*

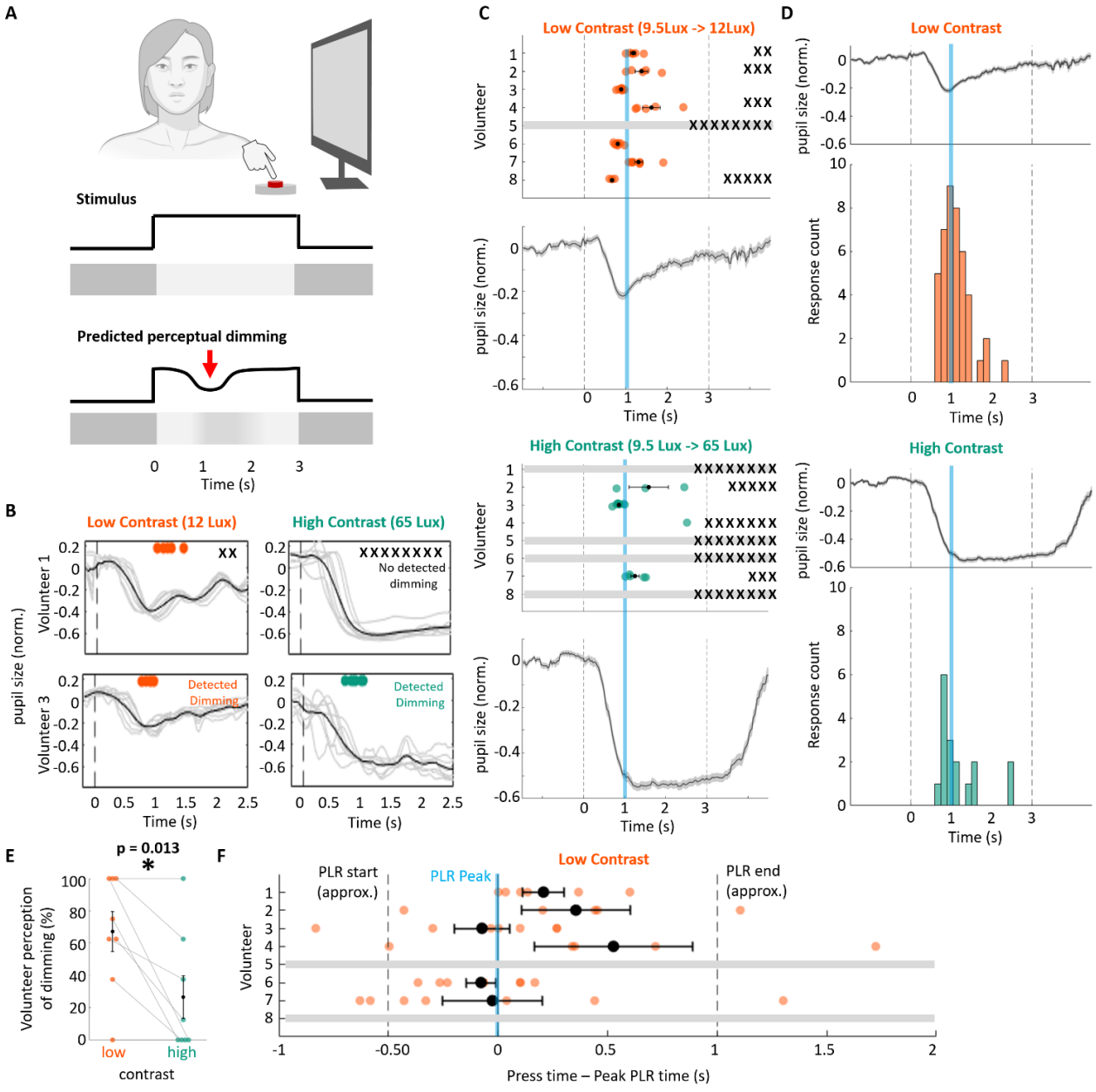

## 2.4. Discussion

Here we demonstrated that pupillary constriction could induce visually-evoked monocular and binocular responses in RGC axons in the dLGN *in vivo*. These responses were synchronous, globally affecting both the ON and OFF channel, and were relayed to the visual cortex. We found that low contrast changes in luminance induced stronger pupillary constriction when presented to both eyes than when presented to only one eye. This also translated into stronger PLR-driven retinal responses, showing that pupillary constriction could drive binocular facilitation. Moreover, we showed that this facilitation improved the SNR of the RGC response to binocular stimulation by a factor 1.4-2. Finally, we reported that the kinetics of pupillary constriction driving retinal activity in mice is conserved in humans, and that the PLR is able to affect perception in humans, suggesting that primate vision may also use pupillary constriction for potentiating neuronal responses in the retina. Overall, we propose this previously undescribed pupil-mediated activity can play an active role in shaping conscious vision in daylight conditions.

Binocularity is currently thought to be predominantly a cortical process, with binocular responses defined as a cell responding to stimulus from either eye[91,92]. Canonical binocular responses are enriched in the primary visual cortex, and not prevalent in the dLGN [91,92,100,101,109–111]. In contrast, we found that pupil-driven binocular responses are highly prevalent already at the level of retinal output, both in terms of the percentage of cells exhibiting binocularity (between 27% and 55% of RGCs, depending on the type) and amplitude of the response (over half of a canonical response's maximum dF/F) (Fig 2.2-3). Previous mouse studies recording RGC activity *in vivo* did not test for this effect[103,104]. We also found that stimulating both eyes could facilitate RGC activity compared to stimulating one eye alone. This binocular modulation was dramatic for low contrast stimulation but negligible for high contrast stimulus (Fig 2.5), was more than additive, and significantly improved the SNR of the produced binocular signal. According to psychophysical studies in human binocular summation, an SNR improvement of 1.4 implies passive addition of two monocular signals, while SNR improvement of 2 would imply an active process[87]. However, such work was performed on faster stimulus that would not be modulated by the pupillary dynamics described here[106–108]. Our observed pupil-mediated non-canonical activity thus likely potentiates other regimes of vision than those that have been previously tested in humans.

Overall, a role for the pupil in shaping binocular responses were likely overlooked in both mouse visual circuits and human psychophysics at least in part because the pupil was not considered as a potential driver of retinal activity.

Changes in pupil size are also often used as a readout of arousal in various species[68,112]. Arousal-associated pupil dilation is driven by the activity of the locus coeruleus, but the role of the pupil dilation itself on various neuronal circuits is confounded by the broad noradrenergic modulation the locus coeruleus exhibits through the brain [113]. While retinal axons in both the dLGN and superior colliculus have been previously found to exhibit changes in firing rate correlating with pupillary dilation, the effect was attributed to neuromodulatory influences on retinal axons within the brain, not to visually-evoked retinal activity[67,70,96]. Furthermore, previous work focused on comparing responses at different pupil sizes as a readout of stable arousal states, not triggered by the pupil change itself[70,96]. In light of our finding that pupillary dynamics can drive retinal activity, we speculate that arousal-mediated pupillary dilation could affect visual responses in at least two ways: 1) Pupillary dilation itself could drive visual responses by increasing the luminance on the retina. In this case, the responses would likely be driven mainly in the ON channel—such as via the responses shown in Fig 2.3F-G and A2. 2) In the hyper-dilated pupil state, PLR-driven responses would likely get stronger, as the pupillary constriction would lead to a larger luminance transient on the retina.

There are other strong retinal responses that ultimately do not lead to perceptual changes, most famously saccade-induced responses, the retina responding very well to the large motion sweeps induced by a saccadic eye movement, with corollary discharge preventing such responses from affecting the visual cortex. The PLR-induced response we describe, however, is prevalent in the visual cortex (Fig 2.4) and can be perceived by humans as perceptual dimming of a sustained full-field flash (Fig 2.9). We infer that perceptual dimming found in human volunteers is due to the PLR for two reasons. The first is that the kinetics of this dimming is very slow, within the range of 1 second, and thus consistent with the PLR-induced retinal response (Figs. 2, 6, 7), and not with other well-known rapid, canonical visual processes. Secondly, volunteers detected perceptual dimming better at low contrast than high contrast, despite the higher contrast eliciting a greater PLR and most canonical visual processes in the human being more robust under high contrast. This is consistent with our mouse recordings, where low contrast stimulation was

better at eliciting responses than high contrast stimulus, also despite higher contrast eliciting a greater PLR. Altogether, these links strongly suggest that human perceptual dimming is due to PLR-induced retinal activity, but future pharmacological trials in humans would further cement the causal link between perceptual dimming and the role of the pupil inducing non-canonical responses.

A key aspect of pupillary dynamics that emerges from our data is how it imposes global, highly coordinated activity onto retinal output. This is a qualitatively different mode of information transfer compared to canonical RGC activity, where the asynchronous activity of different neurons is used to encode the local differences in the highly heterogeneous information content of the visual scene. Global, synchronous PLR-driven modulation could be used as a pathway for relaying ambient luminance information to the primary visual cortex and higher visual areas. We speculate this strong signal could assist some form of global activity normalization throughout the visual system, helping in the detection of low contrast stimuli under a particular retinal adaptation regime. This could be useful when the average luminance on the retina changes, for example, when a shadow falls on a light source (a leaf above moving to block sunlight). Interestingly, it could also help normalize visual information during non-PLR pupil modulation, such as arousal, when the luminance changes solely due to the change in pupil size, and not due to a change in the environment.

Overall, our findings suggest that instead of being a static shutter that can be understood as having an open or closed state, pupillary dynamics plays a key, nuanced role in shaping conscious vision.

# 2.5. Methods

All the experiments were carried out in accordance with European Union Directive 2010/63/EU and under the approval of the EMBL Animal Use Committee and the Italian Ministry of Health License 23- 004_RM_SR. C57BL/6-J (males and females) mice were used in the study.

## 2.5.1. Anaesthetics

For the general anaesthesia induced during both the surgical procedures and the 2-photon imaging sessions, we used intra-peritoneal (IP) injections of FMM. An injectable solution of fentanyl (Fentadon, Dechra, 50 ug/ml, 0.05 mg/kg BW), medetomidine (Domitor, Orion Pharma, 1 mg/ml, 0.5 mg/kg BW) and midazolam (Buccolam, Lesvi, 7.5 mg, 5 mg/kg BW) was prepared and diluted in 0.9% saline solution. The solution was then filtered using a 0.1 μm antibacterial filter (HUM) and kept in a container with restricted access at room temperature until use.

## 2.5.2. Retinal injections

To label RGC axons, 1 ul of chimeric AAV1.2-ProA5-GCaMP6s ($4.4x10^{13}$ vg, produced at EMBL RomeGEVF) was injected intravitreally in the right eye of 4-6 weeks old mice, using a Hamilton syringe (Merck, cat. HAM7634-01-1EA) with a 23s G needle (Analytics, cat n. 7762-05). Mice were first anesthetized using FMM solution (10 ul/g bw, formulation as described above) and head-fixed in a stereotaxic frame (WPI, cat. 505371), while keeping the body temperature to 37°C using a heating pad (Harvard Apparatus, cat. 55-7023). The sclera of the right eye was pierced using a 30 gauge needle on the dorso-temporal side, and the Hamilton needle was inserted and gently pushed on the retina. Virus was delivered at ~30 nl/s and the Hamilton syringe was extracted after 10 minutes from the injection. After the injection, 10% buprenorphine (Bupaq, Livisto) was administered subcutaneously, and mice were allowed to recover.

### 2.5.3. Brain Injections

To label LGN neurons, 200 nl of chimeric AAV1.2-hSyn-GCaMP8f ($2.1x10^{14}$ vg, 1:10 dilution; the plasmid pGP-AAV-syn-jGCaMP8f-WPRE was a gift from GENIE Project: Addgene plasmid # 162376; http://n2t.net/addgene:162376; RRID: Addgene_162376), was injected into the left LGN. Mice were first anesthetized using FMM (10 ul/g bw, formulation as described above) and head-fixed in a stereotaxic frame, while keeping the body temperature to 37°C using a heating pad. The hairs were removed and the skin cleaned with iodopovidone (betadine, Pharmavola, cat. 023907292). After performing a single incision with a scalpel, the skull was exposed, cleaned with 0.9% saline and aligned. A small hole was drilled using a dental drill (Foredom, cat. 1070) with steel a 0.25 diameter drill bit (Jota, cat. 515) above the LGN of the left hemisphere, at -2.2 antero-posterior and -2.07 medio-lateral from Bregma. The virus was delivered 3 mm below the brain surface through a pulled glass needle using an automatic injector (Nanoliter 2020 injector, WPI cat. **300704**), at a flow rate of 10 nl/s. 10 minutes after the injection, the glass needle was extracted and the skin was sutured. Animals were then injected subcutaneously with buprenorphine and allowed to recover.

### 2.5.4. LGN cranial window implantation

After 4 weeks from the retinal injection, a cranial window was opened and a cannula with a coverslip was placed on the surface of the LGN contralateral to the injected eye, to allow for 2-photon recordings of the axonal terminals of the labeled RGCs. Mice were anesthetized with FMM (10 ul/g bw) and placed on a heating pad set to 37°C on a stereotaxic apparatus (as described above). After the hairs were removed and the skin cleaned with iodopovidone (betadine), the skull was exposed and aligned. A ~3.2 mm diameter craniotomy was drilled on the left hemisphere (contralateral to the injected eye), at -1.8 antero-posterior and -2.15 medio-lateral from Bregma, tangential to the skull surface. The brain was kept hydrated using a cortex buffer (125 mM NaCl, 5 mM KCl, 10 mM glucose, 10 mM HEPES, 2 mM CaCl2, 2 mM $MgSO_4$ in ddH2O). The underlying cortical and hippocampal tissue was carefully aspirated using a vacuum pump, exposing the surface of the thalamus. Care was

taken to ensure the thalamic surface and the optic tract were not damaged. Afterwards, a 3 mm diameter stainless steel cannula (custom made), previously glued to a 3 mm coverslip using cyanoacrylate glue, was gently lowered into the craniotomy. The surface of the coverslip was slightly pushed onto the surface of the thalamus and then the outer edge was glued to the skull using tissue adhesive (Vetbond, Ubuy, cat. 14639582) and cyanoacrylate glue (Pattex ultra gel, Distrelec, cat. 110-41-180). After cannula insertion, the remaining exposed portion of the skull was covered with cyanoacrylate glue in order to prevent tissue damage, and a titanium head plate was placed ensuring that the craniotomy was correctly centered. The head plate was further fixed to the skull with dental cement (Paladur, Dentag, cat. DL4621578 and cat. DL6421317) to ensure permanent seal. Carprofen (50mg/ml) (Rimadyl, Zoetis, cat. 10000319) was administered subcutaneously after the surgery, and the mice recovered for 5-7 days.

### 2.5.5. V1 cranial window implantation

After 5-8 weeks from the brain injection, a cranial window was opened above the surface of V1, to allow 2-photon recordings of V1-projecting LGN axons. Mice were anesthetized with FMM (10 ul/g bw) and placed on a heating pad set to 37°C on a stereotaxic apparatus. After the hairs were removed and the skin cleaned with iodopovidone (betadine), the skull was exposed and aligned. A 4 mm diameter craniotomy was drilled above the left visual cortex (ipsilateral to the injected LGN) at -4.5 antero-posterior and -2.4 medio-lateral from bregma. A glass coverslip was gently pushed on the surface of the cortex, and then glued to the skull using cyanoacrylate glue. The head plate was then positioned and fixed using dental cement. At the end of the surgery, mice were injected subcutaneously with 10% buprenorphine, and allowed to recover for 5-7 days.

### 2.5.6. 2-photon imaging

2-photon calcium imaging was performed using a resonant scanning 2-photons microscope (Neurolabware, custom designed) with a 16x, 0.80 NA, 3.0 mm WD water-dipping objective (Nikon, cat. MRP07220). GCaMP molecules were excited using a Ti:Sapphire laser (Coherent, Chameleon Vision II, 80 MHz) at 980 nm and images were collected using Scanbox software (Neurolabware) at 15.5 frames/second 655 x 510 pixels/frame. The recordings were

performed at 4.8x digital zoom for the RGCs axon imaging (~280 x 260 um FOV size, between 50 and 100 um below the optic tract) and at 8x for LGN neurons axon imaging (FOV size ~140 x 130 um, around 100 um from the brain surface). To avoid light leaking from the screen into the PMT during visual stimulation, the objective and the space around the head plate was carefully shielded using black fabric (Thorlabs, cat. BK5) and tape (Thorlabs, cat. T137-1.0). For the animals where multiple locations were recorded during RGC axon imaging, the FOVs were selected to be at least 30 um spaced in the z direction. For recordings on anesthetized animals, mice were injected with FMM at a dose of 5ul/g bw and a thin layer of ophthalmic ointment (VitaPos, cat. B00WG11SD4) was applied prior to recording. Body temperature was kept at 37°C by placing the animal on a heating pad. For awake recordings, mice were trained to run on a circular treadmill (custom-made) while head fixed until they were comfortable and not showing signs of excessive stress (10 days, 2h training per day).

### 2.5.7. Visual stimulation

For all the experiments, visual stimulation was provided dichoptically using two flexible 6 inch OLED screens (2880x1440, 60Hz refresh rate, Wisecoco, model TOP060S02K), curved on 3D-printed arcs. Screens were compensated to make their output linear by inverting the gamma correction function. Screens were placed at 10 cm from the respective eye, spanning 70° x 30° visual degrees. To avoid cross stimulation between the two screens and ensure true separation of the stimuli presented, a black separator was shaped to fit the silhouette of the mouse head and placed between the two screens, isolating each eye from the stimuli presented to the other. Control experiments using TTX on the non-injected eye further confirmed the reliability of the stimuli separation. To characterize the effect of pupillary constriction on the neural activity of RGC projecting to the LGN, or on the LGN neurons projecting to V1, three different full-field stimulation protocols were used. Each stimulus in the different protocols was presented to either the contralateral, the ipsilateral or both eyes for 6 times in a randomized order, for a total number of 18 trials. During the 10 seconds-long inter-trial pauses, the screen was kept on a constant luminance level. That was crucial for the binocular responses to occur, as the baseline luminance allowed a for the consensual PLR to generate a (negative) luminance transient able to evoke a neural response. Such baseline luminance was set to 9.5 LUX. The stimulation protocols were synced with the 2 photon recordings by sending a TTL signal to the acquisition hardware

through a digitally controlled arduino.

### Full-Field Flash

The full field flash stimuli consisted of a simple full-field positive luminance step of either 3 or 5 seconds duration, rising from the baseline luminance. 2 different luminance levels were chosen for generating a "LOW" (20 LUX, 20% Michaelson contrast) or "HIGH" (65 LUX, 43% Michelson contrast) contrast stimulus.

### Full-Field Contrast Ramp

The last stimulation protocol consisted in presenting 12 cycles of a linearly ramping sinusoidal stimulus. The stimulus started from the baseline luminance and oscillated around that, with the amplitude of the oscillations linearly increasing with the number of cycles, ranging from minimal to maximal contrast. The minimal and maximal luminances of the stimulus were set, respectively to 0.15 and 34 LUX. The contrast ramp stimulus was presented at either 0.55 or 2 Hz and was used for assessing the impact of the stimulus frequency on the PLR dynamics and thus on the PLR-driven binocular responses.

### Full-Field Chirp

The chirp stimulation was designed as described in Baden *et al.* (2016), and was presented with the main purpose of maximizing the identification of functional clusters within the recorded neural populations. It was obtained by concatenating 3s long full-field flashes (white, green and blue) , a swept-frequency (chirp) from 0.5 Hz to 8Hz and 12 cycles of a 2 Hz sinusoidal contrast ramp (same as described above), ranging from minimal to maximal contrast. The minimal and maximal luminances of the stimulus were set, respectively to 0.15 and 34 LUX.

### 2.5.8. Pupil tracking

During 2 photon recordings, both eyes were recorded using two camera equipped with a NIR-enhanced CMOS sensor (Basler acA1300-60gmNIR), a 100 mm f/2.8 lens (MVL100M23, Thorlabs) and a 850 nm bandpass filter (Thorlabs, cat. FBH850-40) placed between the sensor and the objective lens. The eyes were illuminated using infrared lamps, and short-pass dichroic mirrors (Edmund Optics, cat. 69-219) were placed in front of each eye for redirecting the NIR light to the cameras, positioned behind the animal. The acquisition of each frame of the cameras was synchronized with the acquisition of the frames of the microscope, aligning the eye videos with the 2 photons recording. The videos were analyzed and the pupil segmented using a custom made Python script, based on a pre-trained CNN published by [114]. The pupil area was calculated by fitting an ellipse to the mask predicted by the algorithm, and the resulting time series low-pass filtered at 1 Hz in order to only keep the pupil fluctuations compatible with the slow dynamics typical of the PLR.

### 2.5.9. Atropine application

In order to perturb the PLR-mediated binocular responses, we used 0.1% atropine (Atropina LUX 10 mg/ml, Allergan, purchased at pharmacy) to block the PLR on the contralateral eye during 2 photons recordings under anaesthesia. We first performed control recordings of the RGC activity in response to a full-field flash stimulation. After 4 to 5 days the responses to the same stimulus, in approximately the same FOVs, were recorded after the instillation of 1 drop (~30 ul) of atropine into the contralateral eye once the pupil was completely dilated and no PLR was visible (5-6 minutes after administration).

### 2.5.10. TTX Injection

To confirm the reliability of our dichoptic stimulation system and be sure that no light was leaking from one side of the separator to the other, we recorded the activity of RGC boutons in anesthetized mice before and after the intravitreal injection of TTX. Animals were anesthetized with FMM and then the

RGC activity was recorded in response to a full-filled flash stimulation. After a control recording, animals were injected intravitreally with 1 ul of 1 mM TTX (Tocris, cat. 1069) using a Hamilton syringe with a 23s G needle. After ~10 minutes from the injection, animals were placed back under the microscope and the RGC activity in the same field of view was recorded in response to the same full-field stimulus.

### 2.5.11. Bouton mask identification and time course extraction

All the image pre-processing, bouton mask identification, and neuropil estimation was done using suite2p (ref here). The raw videos were first visually inspected, discarding all the recordings where drift in the z axis was detected. The videos that passed this step were then registered for correcting for x-y motions along the image plane. After registration, the bouton masks were extracted using Cellpose[115] on the enhanced mean image calculated by suite2p (with model='cyto' and diameter=5). The automatic segmentation was then manually curated and only the predicted ROIs with correct shape and size were kept.

The downstream analysis was performed using custom pipelines (Matlab and Python). First, the neuropil signal was scaled by 0.7 and subtracted from the whole raw trace $F_{RAW}$. The resulting corrected trace $F_{CORR}$ was smoothed with a moving mean window of 4 frames and the activity windows of each trial were extracted using the synchronization file generated during the recording. In order to compensate for possible shift in the baseline fluorescence due to photobleaching, we independently performed $\Delta F/F$ normalization on each individual trial by using as baseline $F_0$ the mean of the activity calculated during the 2 s before the stimulus onset. The extracted traces were further selected according to a response quality index RQI calculated as described by Baden *et al.* (2016) [7]:

$$RQI = \frac{Var[\langle C \rangle_r]_t}{\langle Var[C]_t \rangle_r}$$

where *C* is the T by R response matrix (time samples by number of trials) and

$\langle\rangle_x$ and $Var[]_x$ denote the mean and variance across the indicated dimension, respectively. The RQI gives a quantification of how strong and how conserved across trials the responses are. If the mean of the trials is perfectly representative of each individual trial (i.e. all trials are exactly the same) RQI is equal to 1. For all the recordings, the threshold for the RQI was set between 0.3 and 0.45, according to the overall level of GCaMP expression in each of the FOVs, which could impact the strength of the recorded signal. The ROIs which didn't pass the RQI threshold were discarded and not considered for the subsequent analysis.

### 2.5.12. Response modulation index

To quantify the amplitude of binocular modulation for a stimulus S, we compared the responses elicited by the stimulation of the contralateral eye (*CONTRA* trials) with the one elicited by the simultaneous stimulation of both eyes (*BOTH* trials). Such quantification was done by calculating the response modulation index RMI, defined as

$$\mathrm{RMI}(S) = \frac{\mathrm{AUC}(R_{BOTH}) - \mathrm{AUC}(R_{CONTRA})}{\mathrm{AUC}(R_{BOTH}) + \mathrm{AUC}(R_{CONTRA})}$$

Where, for stimulus *S*, $AUC(R_{BOTH})$ and $AUC(R_{CONTRA})$ are the area under the curve of the trial-averaged $\Delta F/F$ response to the binocular (*BOTH*) and contralateral (*CONTRA*) trials respectively. For the full-field flash stimulus the response modulation index was always calculated during the 'On' period, for the buttons belonging to both On and Off populations, since the pupillary-mediated binocular modulation always occurred during the onset of the stimulus. For calculating the binocular modulation during the full-field contrast ramp stimulus, we used the area under the curve (AUC) of the first 5 cycles to compute the RMI to the "low contrast phase" of the stimulus, while the AUC of the last 7 cycles was used to calculate the RMI to the "high contrast phase" of the stimulus.

### 2.5.13. Identification of functional populations

In order to separate the boutons according to the dynamics of their responses, we used dimensionality reduction to try to construct a low-dimensional embedding where boutons with similar time curse are close together. To do so,

we first selected for each bouton a "response signature". For recordings where the responses to both full-field flash and full-field contrast ramp were available, we concatenated the responses to the *CONTRA* trials of the two stimuli, and used it as the response signature. For the chirp stimulus, since it was specifically designed for maximally separating the RGCs classes, we simply used the responses to the *CONTRA* trial. This created a response signature matrix NxT, where N is the number of boutons and T the number of time samples of the response signature. The response signature matrix was then smoothed and each row independently normalized using z score normalization:

$$R_{norm} = \left[\frac{R^T - mean(R)_t}{std(R)_t}\right]^T$$

where subscript *t* denotes the time dimension of the matrix *R* along which the operation has been calculated. Next, we applied PCA to the normalized matrix $R_{norm}$ to reduce the time dimension and obtained a new matrix $NxT_{reduced}$. For clustering analysis, we only kept the first two components with highest explained variance, and applied either k-means or gaussian mixture models algorithm to the data in the 2-dimensional PCA space. The number of clusters was empirically tuned, and the purity of each cluster individually inspected. In the cases where PCA underperformed and failed in reaching a clear discrimination of the response dynamics, we applied the UMAP algorithm for reducing the dimensionality of the time dimension. The clustering was then performed on the data projected onto the first 2 components found by UMAP, analogously to the clustering performed in the PCA space.

### 2.5.14. SNR calculation

To compute the SNR, we estimated the signal and the noise components as proposed by Stringer et al. 2019. We estimated the signal variance $V_{signal}$ of each bouton by averaging over the covariances calculated between all the combination of trial repetitions:

$$V_{signal}(s) = \frac{1}{n}\sum_{i=0}^{n-1}\sum_{j=i+1}^{n} Cov(R_i, R_j)$$

where $n$ is the number of trials for the stimulus $S$, and $R_i$ *and* $R_j$ *are the responses to the* $i^{th}$ *and* $j^{th}$ trial respectively. The noise variance $V_{noise}$ was calculated as the difference between $V_S$ and the average across the within-trial variances calculated for all the repetitions. The SNR was then calculated by taking the ratio between $V_{signal}$ and $V_{noise}$ .

$$V_{noise}(s) = V_{signal}(s) - \frac{1}{n}\sum_{i=0}^{n} Var(R_i)$$

$$SNR(s) = \frac{V_{signal}(s)}{V_{noise}(s)}$$

## 2.5.15. Statistical analysis and quantification

All the statistical comparisons between paired data were performed using paired t-test. Unless otherwise noted, all population data are reported as mean ± SEM, n represents the number of cells analyzed, and N represents the number of animals. Bonferonni correction was applied when multiple hypotheses were tested. The distance between data distributions was quantified using the Kolmogorov–Smirnov test. Significance intervals for RMI distributions was estimated by taking the 95th percentile of the distribution fitted over the shuffled data. All tests and quantifications were performed using Matlab.

### 2.5.15.1. Human psychophysics

*PLR kinetics*

The experiments on PLR kinetics were carried out by Gabriel Peinado Allina, a research fellow in the Ala-Laurila lab with which I collaborated for this part of the project.

*Subjects.* Three male human observers aged 25–35 participated in the study. One observer was one of the authors; the rest were naïve to the purposes of the study and received a small monetary compensation. All subjects had normal uncorrected vision. The study was conducted in accordance with the

principles of the Declaration of Helsinki and the guidelines of the University of Helsinki ethical review board. The participants signed a written informed consent.

*Stimuli*. To approximately match the intensity of the light stimuli utilized in the mouse experiments in terms of photon captured by rod photoreceptors (R*) across mice and humans, the irradiance spectrum (in Watts m-2 nm-1) of the OLED screen utilized for murine experiments was calculated based on the apparent brilliance of the screen measured with a hand-held lux meter, and on the emission spectrum of the OLED screen weighted by the photopic luminosity function (in lumens W-1, CIE 1978) (42). Based on the irradiance spectrum of the screen, the number of R* per mouse rod per second was then estimated as described in (43), considering the optic losses of intraocular media and the collecting area of mouse rods as a function of wavelength, peaking at 0.93 R* um-2 rod-1 hv-1 (44). Based on these calculations, the intensity of a 470 nm light source producing full-field illumination by means of a Ganzfeld bowl was then adjusted to produce a similar number of R* per human rod, calibrated as described in (45). The mean light intensity utilized for human experiments was 1500 R* rod-1 s-1. This light intensity was modulated to produce 3s steps of light matching the relative intensity of those utilized in the murine experiments (1895 R* rod-1 s-1 and 3160 R* rod-1 s-1) or modulated by a square or sinusoid frequency which linearly increased to 100% contrast in 12 cycles.

*Apparatus.* The experiment was run in a pitch-black light-proof room utilizing a Ganzfeld bowl built in house coated with BaSo4 based paint. The light source consisted of a high-power LED with an emission spectrum peaking at 470 nm (Thorlabs, M415L4), further narrowed with a 10 nm full width half-maximum bandpass filter centered to 470 nm (Thorlabs, FBH470-10). The current passing through the LED was precisely controlled by an in house build high-dynamic range LED driver with temporal precision of 10 $\mu$s, controlled by a single-board computer (Raspberry Pi 4, Raspberry Pi Foundation) running custom Python and BASH software. The Pupillary Light Responses were recorded with an infrared camera (RPI HQ cam, Raspberry Pi Foundation) and an 850nm infrared LED estimated to produce less than 10-4 R* rod-1 s-1. Digitized videos of the participants' face were analyzed with a custom Python algorithm to segment out the pupils, and then to determine the pupil radius.

*Procedure*. All subjects were dark adapted during 15 minutes in a pitch-black room at the beginning of every experiment, after which they were allowed to adapt to the 1500 R* rod-1 s-1 background for 5 min. Each stimulus was presented from dimmest to brightest or from slowest to fastest, and each stimulus was presented for 4-7 repetitions. The order in which the stimulus types (steps or frequency ramps) were presented varied across experiments.

### *Visual detection experiment*

*Subjects*. 8 human subjects (4 male and 4 female) aged 20-40 participated in the study, all of them naïve to the purpose of the study. All subjects had normal or corrected vision.

*Stimuli*. The stimulation protocol included a randomized sequence of 8, 3 seconds low-amplitude luminance step (9.5 LUX to 12 LUX) and 8, 3 seconds high-amplitude luminance steps (9.5 LUX to 65 LUX), matching the same luminance values used for the experiment we did in mice. Each trial consisted of 6 sec seconds of baseline luminance (9.5 LUX), followed by a 3 seconds long, step-like luminance increase (to either 12 or 65 LUX). Importantly, the luminance during the 3 seconds step was kept constant until the end of the trial. Prior to the stimulation protocol start, the subjects were habituated to the baseline luminance (9.5 LUX) for 10 seconds.

*Task*. The subjects were informed they would have to perform a visual detection task. The task would consist of detecting minor screen luminance fluctuation happening randomly, at any point, during any of the luminance steps, regardless of the trial type (low or high amplitude luminance change). Subjects were asked to promptly report whenever they perceived the luminance fluctuation by pressing a keyboard key and, importantly, they were not aware that all the luminance steps were made uniform in time. The subjects were allowed to practice in a trial round before performing the actual experiment, in order to get familiar with the task.

*Apparatus*. The visual stimuli were designed using PsychoPy (ref. 57) and presented on a 34.1'' LCD monitor (DELL U3419W). The subjects placed their head on a stabilizer device at 30 cm distance from the monitor. Pupil videography was performed using a NIR-optimized camera (Basler acA1300-60g) mounting a zoom lens (Navitar f=100/F2.8) and the eye was illuminated using an IR lamp. Videos were acquired at 30 hz and the pupil was segmented and analyzed using a custom Python script based on MEYE [114].

# 2.6. Annex

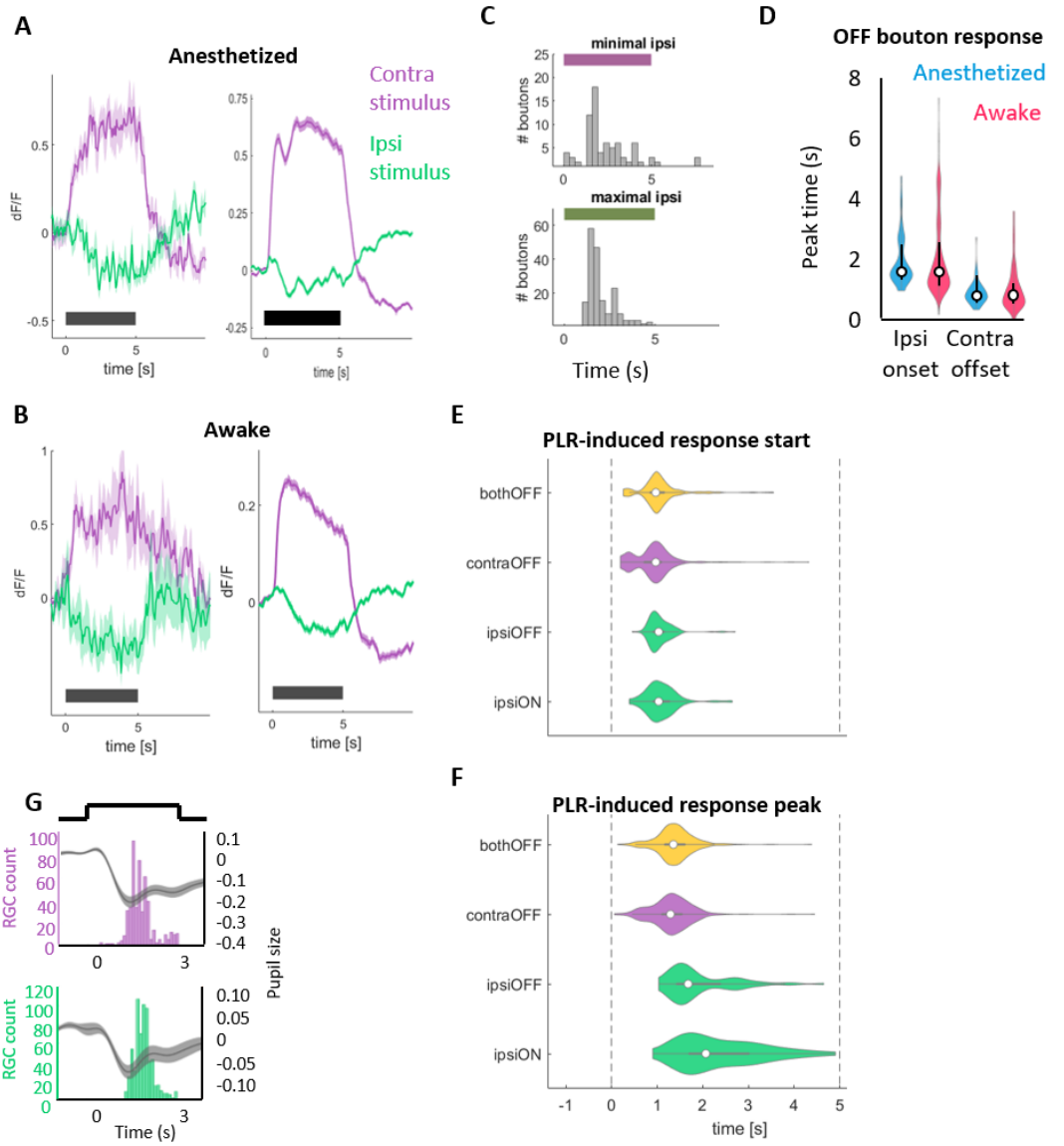


***Figure A2.1: Binocular responses in early visual pathway.***

***A**) Left: example contralateral ON RGC bouton responding to full field flash stimulation to contralateral (violet) or ipsilateral eye (green) Right: ON population response (n=533 boutons, N=5 animals). **B**) Same as A, but in awake animals (n=693 boutons, N=5 animals). **C**) Left: Time of minimal response to ipsilateral stimulation in ipsi-responding ON boutons in anesthetized mice (n=101 boutons, N=5 animals). Right: Time to maximal response to ipsilateral stimulation in ipsi- responding OFF boutons (n=192 boutons, N=5 animals). **D**) Maximal peak latency of OFF boutons responding ipsilateral*

*stimulation (peak during onset) and contralateral stimulation (peak during offset) in awake and anesthetized mice.* ***E****) Beginning of PLR-driven response (in seconds after onset) for OFF RGC boutons responding to binocular (yellow, n=314 boutons), contralateral (purple, n=321 boutons) and ipsilateral (green, n=148 boutons) stimulation and ON RGC boutons responding to ipsilateral stimulation (green, n=59 boutons).* ***F****) Same as E) for the peak of PLR- driven response.* ***G****) Contralateral pupil size change overlaid over peak time of onset response of OFF boutons during contralateral (left) and ipsilateral (right) stimulation.*

***Figure A2.2:***
***PLR modulates responses of ON RGC boutons****.*
***A****) Left: Change in pupil size of the right eye due to direct PLR (purple) and consensual PLR (green). Right: Same as left, but after application of the atropine.* ***B****) Top Left: Heatmap showing all contralateral ON RGC bouton (n=83, N=5) responses to contralateral full-field stimulation (scale -0.1 dF/F to 2 dF/F). Bottom left: Same boutons as in B Top left responding to full field flash to the ipsilateral eye (scale -0.5 dF/F to 0.5 dF/F).* ***C****) Same as B after the application of atropine to contralateral eye (n=71, N=5). C) Left: Population response (mean +- SEM) of boutons presented in B. Response to contralateral (purple) and ipsilateral (green) stimulation. Right: Same as B left, after application of atropine to the contralateral eye.* ***D****) Spearman correlation of response to ipsilateral stimulation and pupil constriction before atropine (green) and after atropine (gray). Two-sample t test p=6.13*10^-5.*

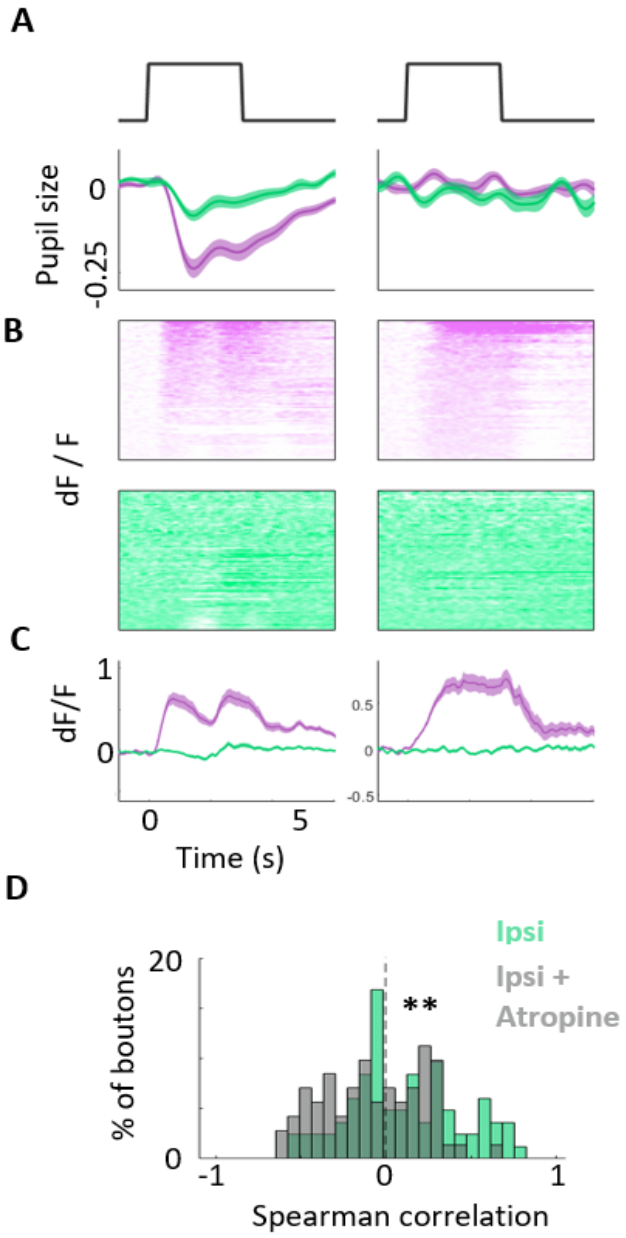

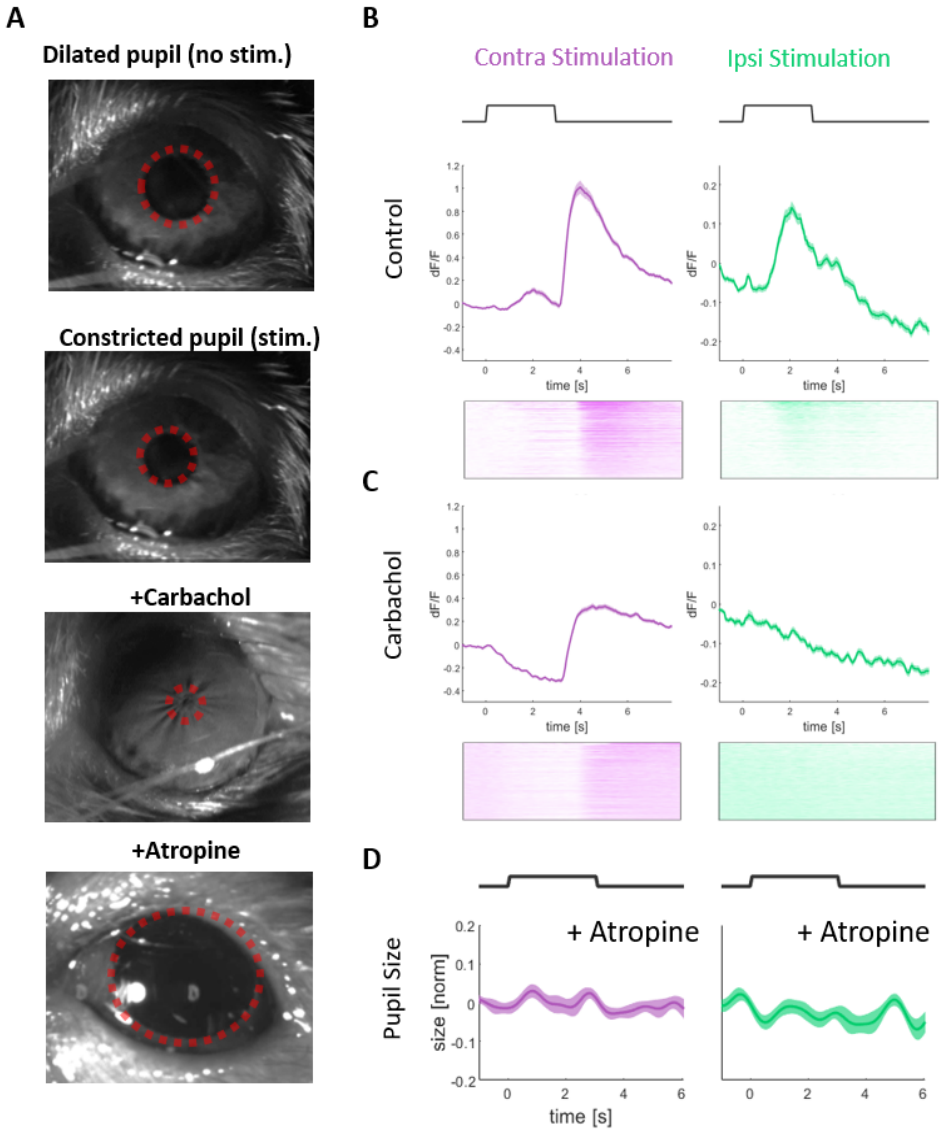


***Figure A2.3: Pharmacological dilation of the Pupil with Atropine, contraction with carbachol.*** ***A****) Example of animal pupil when dilated (top), constricted due to visual stimulation (2nd figure), constricted due to carbachol administration (3rd figure), and dilated due to atropine administration (bottom). Dotted circle indicates approximate extent of pupil opening.* ***B****) Population activity (top) and heatmap (bottom) of OFF RGC activity before Carbachol administration.* ***C****) Same boutons in B after carbachol administration. D) Pupil size after Atropine administration, showing no pupil change to either eye stimulation due to full-field flash. N = 5 animals.*

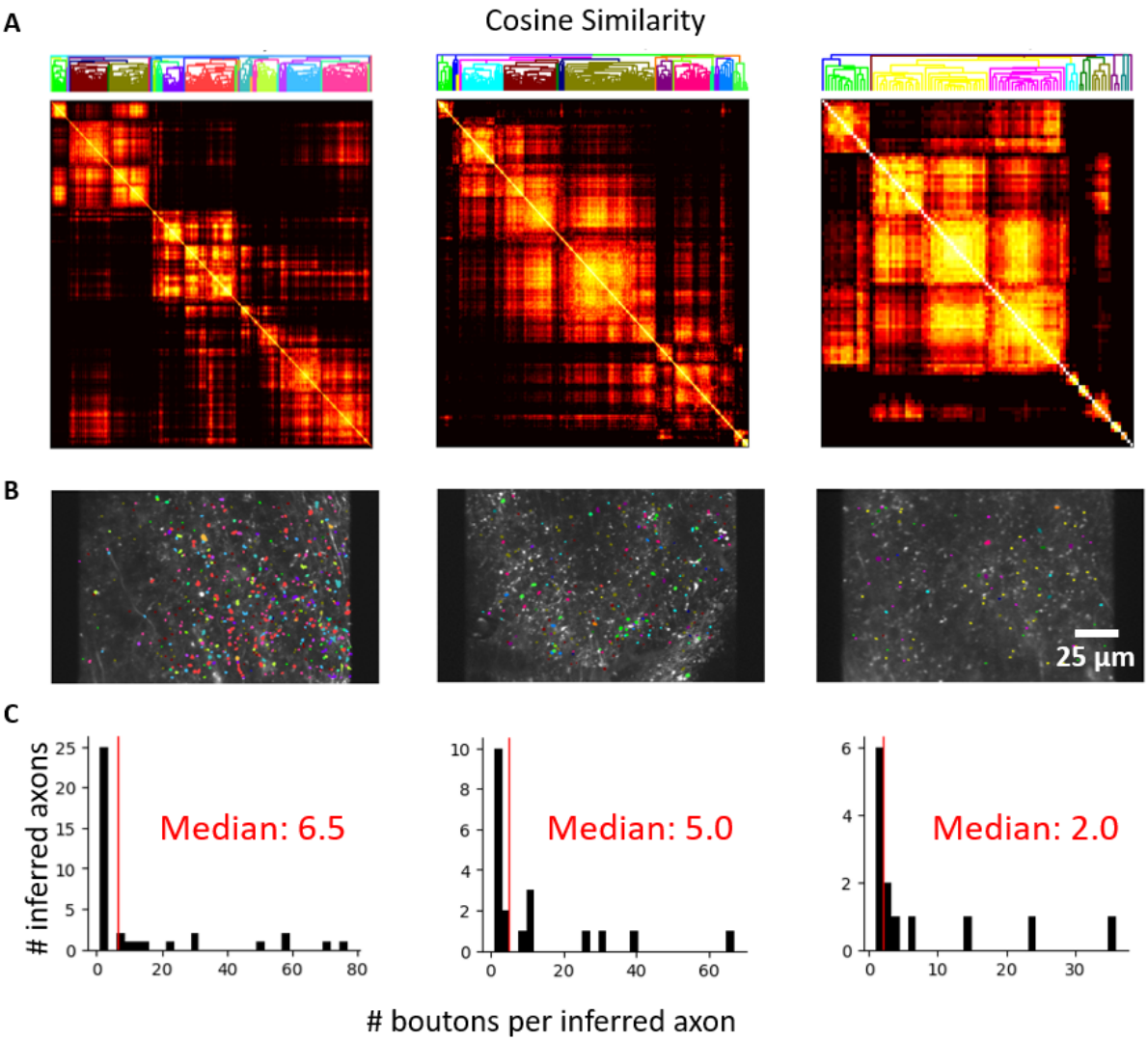


***Figure A2.4: Axon identification analysis performed over 3 different field of views.***
***A****) Bottom: pairwise cosine similarity (1-cosine distance) matrices calculated between the spontaneous activity correlation vectors, which reflects how much different boutons are similar in their correlation with all the other boutons. Top: dendrogram representing the clusters of boutons obtained from the WPGMA linkage clustering using the cosine distance matrix.* ***B****) The 3 field of views used for the analysis. Boutons' masks are color-coded according to the cluster identity.* ***C****) Distributions of the cluster sizes, i.e number of boutons per inferred axon. The red lines are on the median of each distribution.*

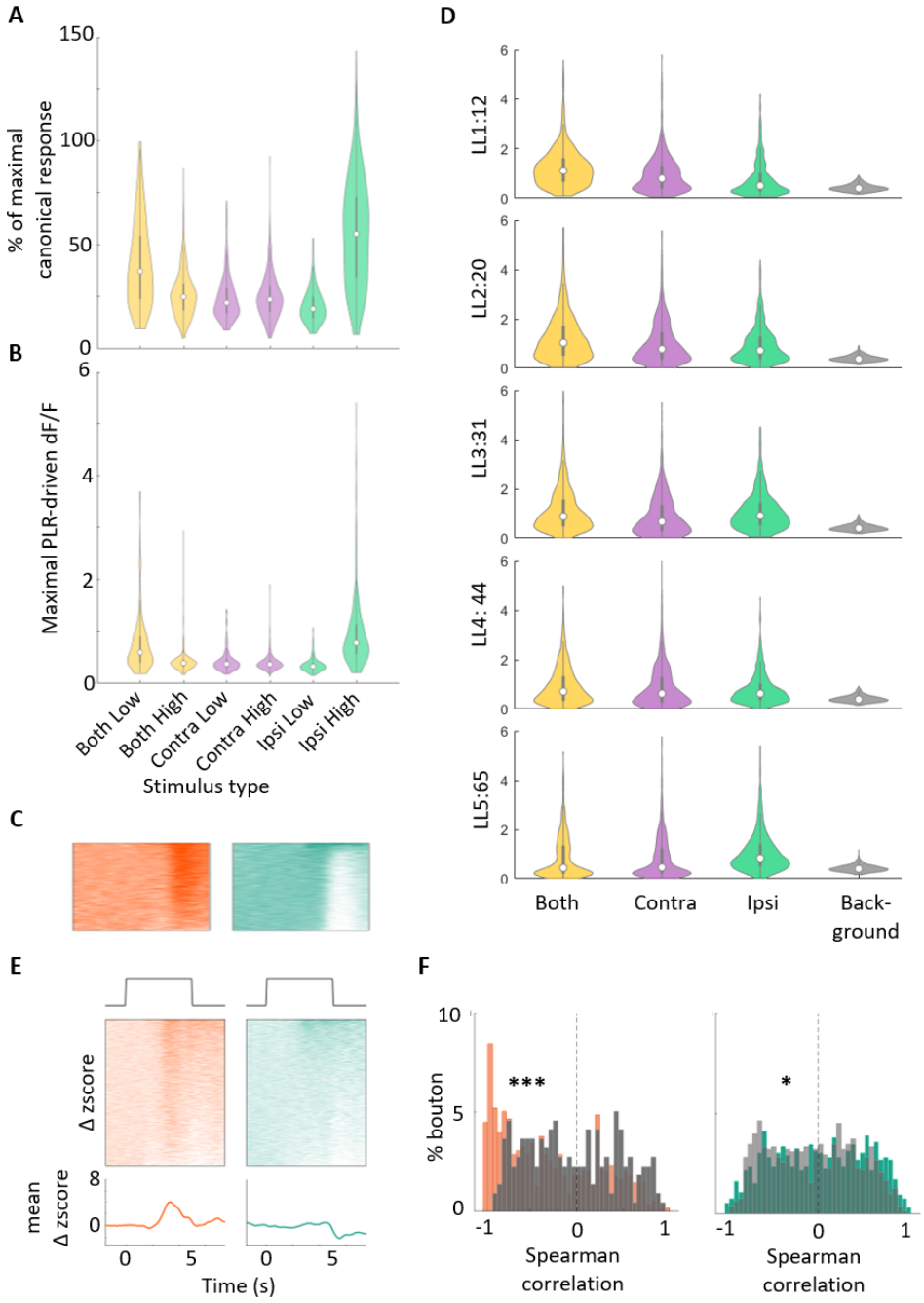


***Figure A2.5.: Contrast-dependent binocular facilitation in RGC boutons***

***A**) Response strength of PLR-driven responses in a subpopulation of OFF RGC boutons (shown in detail in Figure 5). dF/F of PLR-driven response as a percentage of canonical response during low and high contrast binocular (yellow), contralateral (purple), and ipsilateral (green) stimulation. **B**) Same as A, but showing maximal dF/F of PLR driven responses. **C**) Frame-by-frame difference in z-score between response to binocular stimulation and response to ipsilateral stimulation during low-contrast (orange) and high-contrast (green) flash stimulation in the OFF subpopulation further described in figure 5. **D**)*

*Maximal dF/F of PLR-driven response of all contralateral OFF RGC boutons to all luminance steps (LL1: 12 LUX n=714 ; LL2: 20 LUX, n=861; LL3: 31 LUX, n= 911; LL4: 44 LUX, n=909 and LL5: 65 LUX, n=920) during binocular stimulation (yellow), contralateral stimulation (purple) and ipsilateral stimulation (green). Gray violin plot represents negative control, maximal response before stimulation.* ***E****) Top: Frame by Frame difference between z-score of response to binocular stimulation and contralateral stimulation during low contrast (20 LUX, orange) and high contrast (65 LUX, green) stimulation for all OFF boutons. Bottom: Mean of z-score difference shown on top.****F****) Spearman correlation between frame-by-frame binocular facilitation of all OFF boutons (shown in E) and frame-by-frame difference in strength of PLR in corresponding pupil during binocular and monocular stimulation. Left: Low contrast stimulation before (orange) and after atropine (gray), two-sample t-test: p<0.001. Right: Same as left, but high contrast stimulation, two-sample t-test: p=0.026.*

# Chapter 3

## Internal states reshape the geometry of cortical populations dynamics in V1 during sustained sensory drive

## 3.1. Abstract

Neural activity in sensory cortex is strongly influenced by internal brain states such as arousal and behavioural engagement. Previous work has shown that internal state fluctuations modulate amplitude, variability, and correlations of firing rates in cortical populations, with important consequences for sensory encoding. However, most studies have relied on brief, trial-based stimulation paradigms, studying the effect of arousal on trial-averaged stimulus responses and residuals. Here, I investigate how arousal fluctuations modulate population-level activity in primary visual cortex (V1) under sustained visual stimulation. I performed two-photon calcium imaging in layer 4 (L4) and layer 2/3 (L2/3) of mouse V1 while presenting extended epochs of continuous visual stimuli with varying statistical complexity, from simple moving patterns to naturalistic movies. Rather than focusing on trial-averaged responses, we analysed how arousal dynamically reshapes the geometry and dimensionality of ongoing population activity. I found that arousal globally increases neural activity across layers through a low-dimensional shared activity mode, exerting distinct, layer-specific effects on the structure of the population activity. During low-complexity stimulation, arousal has only marginal effects on the structure of L4 populations, with most of the neural variance being explained by the simple stimulus dynamics. In contrast, in superficial layers (L2/3), the shared activity mode induced by arousal is much stronger and captures a large fraction of neural variance, leading – at the seconds timescale - to a significant reduction of population dimensionality

despite increased firing rates. When stimulus complexity is increased using naturalistic movies, arousal leads to a more dramatic dimensionality reduction in both layers, indicating an interaction between sensory richness and state-dependent modulation of the population geometry. Moreover, I found that the alignment between the leading coding directions of arousal and global stimulus statistics (such as mean luminance or motion energy) also varied as a function of stimulus complexity. These findings show how the effect of internal states on cortical populations varies across cortical layers and stimulus complexity, and highlight the importance of continuous, single-trial stimulation paradigms for understanding the relationship between global, low-dimensional state signal and local, sensory-driven population dynamics.

## 3.2. Introduction

The activity of cortical populations in sensory areas is not uniquely driven by the sensory input, but instead it reflects a complex interaction between the incoming sensory information and the ongoing fluctuations in the overall state of the brain [50,116,117]. As a consequence, the same sensory input can generate different patterns of neural activity depending on the current state of the cortical network [38]. Such variability in the stimulus-evoked responses is usually referred to as trial-to-trial variability. Traditionally, this variability has been treated as noise –an unwanted by-product of neural processing that limits the reliability of sensory coding [118]. In classical works, trial-to-trial variability is quantified by averaging the responses over multiple repetition of the same stimulus and analysing the deviations from this stereotypical response, often referred as residual activity [116]. This operation assumes that the neural activity can and should be decomposed in signal – information-rich activity component which should not vary across repetitions of the same stimulus – and residual noise. Within this framework, cortical states are often seen as contextual modulators of stimulus-driven response statistics, such as mean firing rates, response gain or noise correlations [50,64,119]. A large body of work focused on how internal brain states impact these statistics and thus the quality of the sensory representations [28,38,60,58]. For example, it has been shown how transitions from synchronized to desynchronized cortical states, like the one observed between quiescence and behavioural-engagement, are associated with reductions in low-frequency activity and decreases in shared variability and noise correlation, improving the stimulus discriminability at the

population level [28,51]. These observations have led to the idea that internal states regulate the quality of sensory coding and shape the perceptual performances [37]. Particularly, electrophysiological experiments in mice have provided extensive characterization on how fluctuations in the level of arousal can suppress the noise correlations and increase stimulus discriminability in the primary visual cortex [28,60,120]. Related works additionally showed that arousal fluctuations can also alter the dimensionality of stimulus-driven activity, thereby reshaping the geometry of the population responses [57].

However, the vast majority of these studies have relied on trial-based experimental paradigms, in which brief, repeated stimulus presentations are interleaved with periods of baseline activity. Within such paradigms, internal state is typically treated as a contextual variable that modulates trial-averaged responses or residual variability around a mean sensory response. While this approach has been highly informative, it implicitly assumes that ongoing sensory processing can be decomposed into discrete trials, and that internal state acts primarily as a slow modulator of stationary stimulus representations. In naturalistic settings, however, sensory input is continuous rather than episodic, and internal states fluctuate dynamically at timescales different from the one of sensory processing [38]. Under these conditions, the distinction between "evoked" and "spontaneous" activity becomes less clear, and trial-based analysis may obscure important aspects of how population activity is structured in time.

In this project, I move beyond the trial-based framework to investigate how arousal modulates population activity in primary visual cortex (V1) during continuous visual stimulation. Using in vivo two-photon calcium imaging across cortical layers in awake mice, I recorded the activity of neuronal populations in L4 and L2/3 while presenting extended epochs of visual input with varying degrees of complexity, ranging from simple, artificial moving patterns to naturalistic movies. Rather than characterizing the effects of state fluctuations through trial-averaged responses to short stimuli, I analysed how internal states dynamically reshapes the structure, dimensionality, and temporal organization of population activity on minutes-long single trials of continuous stimulation.

Across layers, I show how arousal globally impacts cortical populations through a single, shared activity mode [56,57,121], which increases the overall neural activity. Particularly, my data show that arousal compresses the dimensionality of population activity by increasing the amplitude of pairwise correlations, at the slow (seconds) timescales allowed calcium imaging. Moreover, I report differential effects of arousal between cortical populations in L4 compared with L2/3, with L4 only showing mild perturbations in the structure of the population activity during arousal compared to L2/3 when presenting low-complexity stimuli. However, when turning to naturalistic stimuli, the dimensionality of the population activity is severely impacted in both layers, showing an interaction between stimulus complexity and the extent of the arousal-induced reshaping of population activity. Moreover, I also report how the shared arousal mode and the leading coding direction of a low-dimensional stimulus representation (such as luminance or energy profile) tend to align as a function of the stimulus complexity. This suggests a possible interesting interaction between low-dimensional sensory representations (computed locally) and neuromodulatory signals which carry higher-level, contextual representations of sensory experience (such as novelty) [37,39].

This work highlights the importance of studying cortical computation under continuous, single-trial stimulation paradigms. By analysing how internal states shape the geometry of population activity rather than trial-averaged responses alone, I provide a novel framework for understanding how sensory and internal state signals relate and interact with each other. Specifically, these results suggest that internal state fluctuations: i) continuously shape the geometry of cortical populations in sensory areas and ii) can be aligned with low-dimensional stimulus representations under naturalistic stimulation, showing a dynamic interaction between the information content of local, sensory-driven activity and global state signals.

# 3.3. Results

I investigated the effect of arousal modulation on ongoing cortical dynamics in primary visual cortex while mice were passively viewing different types of prolonged, sustained visual stimuli. The stimulation protocols used lacked a classical trial structure, avoiding sequential repetitions of many short presentations of the stimuli as well as trial averaging, which often assumes stationarity of the visual coding and can obscure the true dynamics of the system. This approach allowed me instead to look at the behaviour of the cortical populations at the minutes-timescales, characterising how the spontaneous fluctuations of arousal state dynamically impact the structure of population activity and interact with stimulus representations.

## 3.3.1. 2-photons calcium imaging in L2/3 and L4 of V1

To investigate how spontaneous arousal fluctuations reshape the ongoing population activity in the primary visual cortex (V1), I performed in vivo 2-photons calcium imaging on awake, head-fixed mice, while providing continuous visual stimulation. The recordings were performed either in transgenic mice expressing genetically encoded calcium indicators in excitatory neurons of layer 4 (L4), or following viral injection targeting excitatory neurons in layer 2/3 (L2/3) (Fig 3.1 a). During the experimental sessions, the animals were free to run on a circular treadmill. Coherently with a large body of work studying internal state modulation of cortical processing, I operationalized arousal using a continuous scalar measure of pupil area [38]. Together with pupil size, speed of locomotion and gaze position were also monitored throughout all the recordings. Visual stimuli were presented using a three-screen apparatus covering a large portion of the visual field, thereby minimizing edge artifacts and approximating more naturalistic visual conditions.

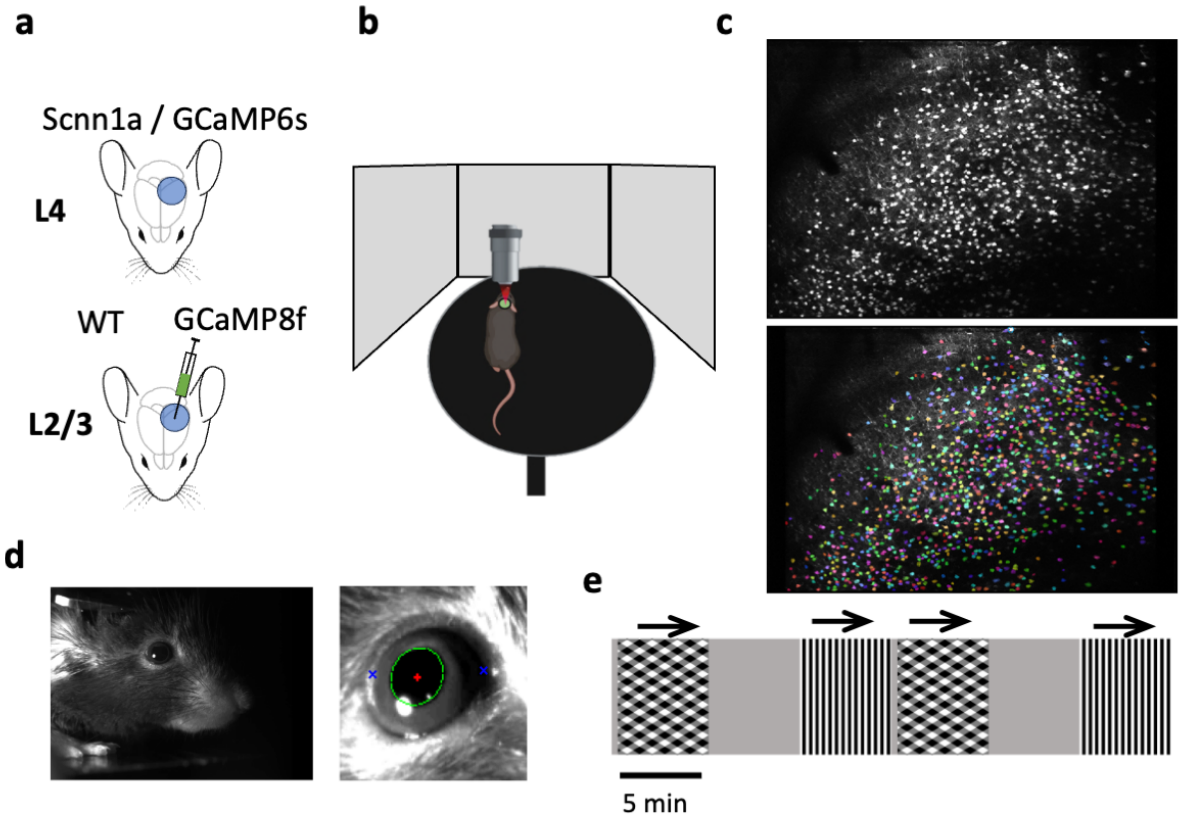


***Figure 3.1: Experimental setup***

***a)*** *Preparations used in this study; top: transgenic Scnn1a line crossed with Ai94-D reporter line, expressing GCaMP6s in excitatory neurons of layer 4 (L4).* ***b)*** *Two photon calcium imaging was performed in head-fixed mice, free to run on a circular treadmill, where the velocity of locomotion was continuously monitored; visual stimuli were presented on three LCD monitors covering most of the animal's visual field.* ***c)*** *Example field of view before (top) and after (bottom) soma segmentation.* ***d)*** *The face of the mouse was constantly monitored throughout the recording; pupil size and gaze position were later extracted and used for subsequent analysis.* ***e)*** *Low complexity stimulus protocol: the protocol consisted in 5 minutes long presentations of: right-drifting plaid pattern, static grey and right-drifting grating pattern. The three stimuli were repeated for 2 times, and 10 seconds of grey background was interleaved between each stimulus repetition.*

Animals were presented with prolonged epochs of a low-complexity stimulus pattern, consisting of a moving plaid pattern (drifting from the left visual field to the right visual field) (P), a static grey background (G), and a moving grating pattern (G), drifting in the same direction as the plaid, as in (Fig 3.1 e). Each stimulus lasted for 5 minutes, with 10 seconds grey screen interstimulus interval. The sequence of stimuli (PGG) was repeated twice.

Importantly, the activity recorded was never averaged across the 2 repetitions of a stimulus, treating them as separate, independent activity periods. Fig 3.2 a and b show the activity recorded during single sessions from L4 and L2/3 while presenting the low-complexity PGG protocol. For each session, I recorded hundreds of neurons either on one or 2 focal planes (1037.5 ± 282.5 SEM in L4, N=4; 849.6 ± 135 SEM in L2/3, N=3), ensuring a good sampling of the excitatory population in each cortical layer. Fig 2.2 a and b show the neuronal activity recorded during example single sessions from L4 and L2/3 while presenting the PGG protocol. When qualitatively comparing the sorted heatmaps of calcium traces, the structure of L4 activity looked tightly bound to the stimulus, with individual subpopulations tracking the different periods of the protocol. This observation was in line with the fact that activity in L4 is mainly driven by thalamic inputs. However, transient, synchronous modulations of the population's activity aligned with arousal and locomotion fluctuation were also visible, supporting the idea that internal states can shape cortical activity already in L4, as previously reported [122]. On the other hand, the structure of activity in L2/3 looked much more impacted by arousal and locomotion events, and less constrained by the stimulus alone. This is was consistent with the vast heterogeneity of cortical afferences driving the activity of the neural populations of L2/3, bringing both sensory and non-sensory information[23].

***Figure 3.2: L4 and L2/3 populations recorded during low-complexity stimulation protocol***

***a)*** *Representative recording session performed in L4; the traces on the top represent, in order, the time course of pupil area (used in this study as a proxy for the instantaneous arousal state), gaze position and running velocity; the heatmap represent the z-scored calcium fluorescence recorded in ~2000 neurons simultaneously; the time windows spanning each stimulus epoch are color-coded in the following way: pink for the plaid stimulus, green for the grey stimulus and blue for the grating stimulus; the bottom row represent the individual stimuli active during each of the stimulus epochs. Stimulus-tuned subpopulations clearly emerged in this layer, and arousal/locomotion fluctuation seems to evoke some synchronous activity.* ***b)*** *Same as a) but for L2/3; here the segregation of stimulus-tuned subpopulations is less clear, but arousal fluctuation seems to drive the population activity much more strongly*

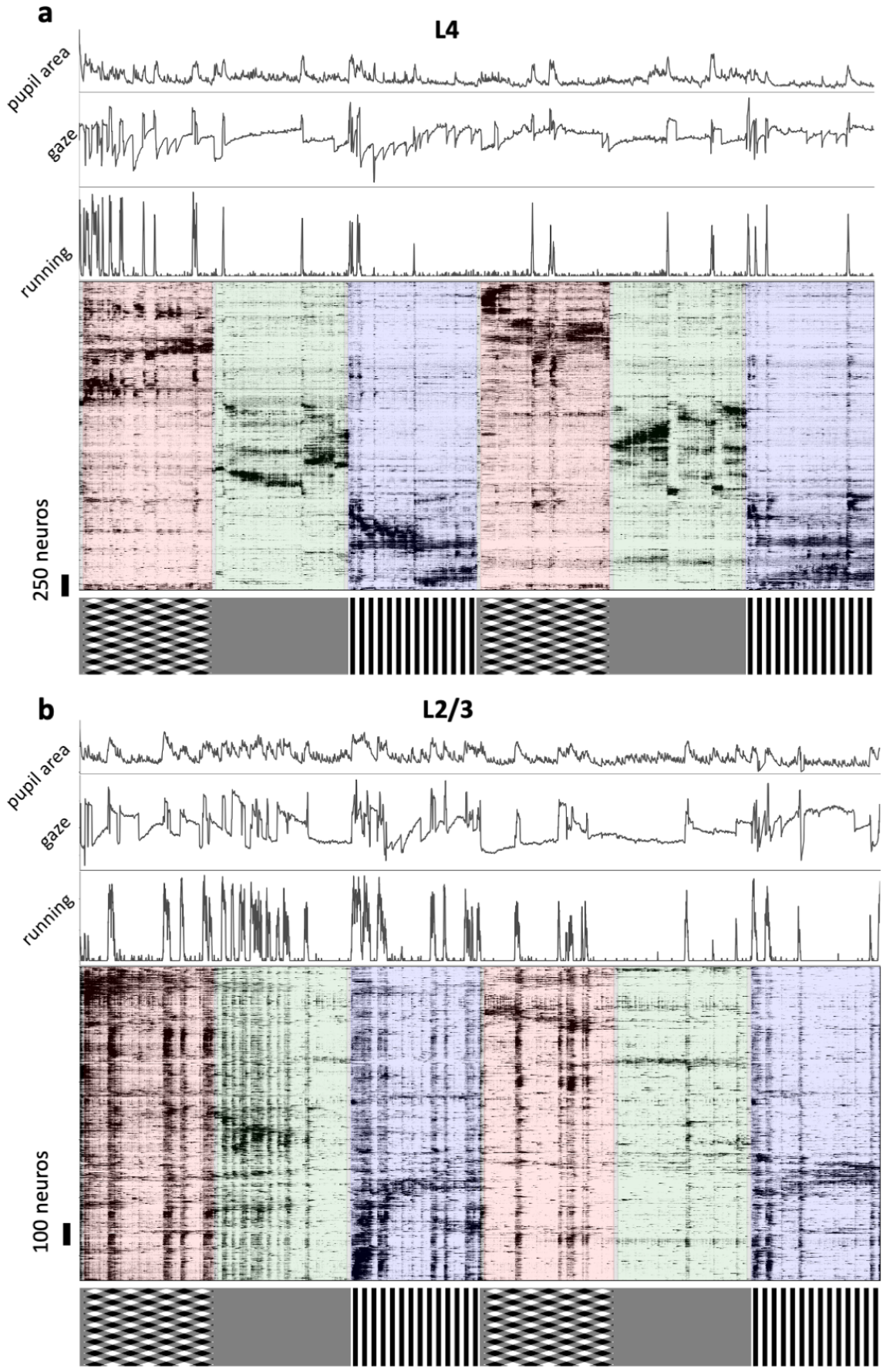
a
L4
pupil area
gaze
running
250 neuros
b
L2/3
pupil area
gaze
running
100 neuros

### 3.3.2. The geometry of population activity in L4 and L2/3 differs during simple, sustained sensory drive

Following the observation that both stimulus drive and arousal fluctuations seem to have profoundly different effects in L4 and L2/3 during continuous visual stimulation, I investigated and compared the geometry of the ongoing population activity recorded in the two layers. To do so, I performed principal component analysis (PCA) separately for L4 and L2/3 populations (see Methods section). PCA provides a compact and interpretable description of the neural population geometry by identifying orthogonal axes that capture maximal shared variance across all the neurons. In both layers, the variance was not equally spread across the eigenspectrum, but instead it was concentrated on the first few dimensions, with the eigenvalues quickly dropping around 0 after the first 10 components (Fig 3.3 c, d).

An explicit estimate of the effective dimensionality can be obtained by calculating the participation ratio (PR), a measure of how the eigenvalues are spread across the components (see 2.5 Methods section). Interestingly, the average fractional participation ration was low in both layers, indicating low-dimensional population activity, but with L2/3 dimensionality (fractional PR = 0.018 ± 0.002 SEM, N=3) being almost 3-folds lower than the one in layer 4 (fractional PR = 0.055 ± 0.01 SE, N=4). Low-dimensional projections of the neural activity onto the first 2 leading PCs also qualitatively differed across layers, and revealed the nature of the difference observed in the eigenspectra. In L4 PC1 and PC2 explained almost an equal amount of variance and correlated with stimulus (Fig 3.3 e, i); the trajectories were segregated in defined stimulus-specific subspaces reflecting reliable encoding of stimulus epochs (plaid, grey or grating, Fig 3.2 a) and, across animals, showed only mild correlations with arousal on PC1 but not on PC2 (Fig 3.3 i). This was also evident when looking at the distribution of the PCs weights, which were normally distributed around 0, indicating different directions in the contributions of the neurons to that component (Fig 3.3 f) – consistent with the idea that stimulus encoding likely requires heterogeneous population activity. In L2/3, conversely, almost all the variance was collapsed onto the first PC, which robustly correlated with arousal but not stimulus time course. Opposed to L4, PC1 weights were all shifted towards same-sign values, reflecting a uniform direction of modulation shared by all the neurons (Fig 3.3 h), compatible with the uniform excitatory effect that arousal-related neuromodulatory signals

exert on the cortical populations in V1 [120,123]. Moreover, logistic decoding of stimulus epochs revealed that this dominant, shared activity mode bares no stimulus information in L2/3 (accuracy=0.42 ± 0.01 SE, N=3), opposed to the PC1 in L4 (accuracy=0.82 += 0.1 SE, N=4).

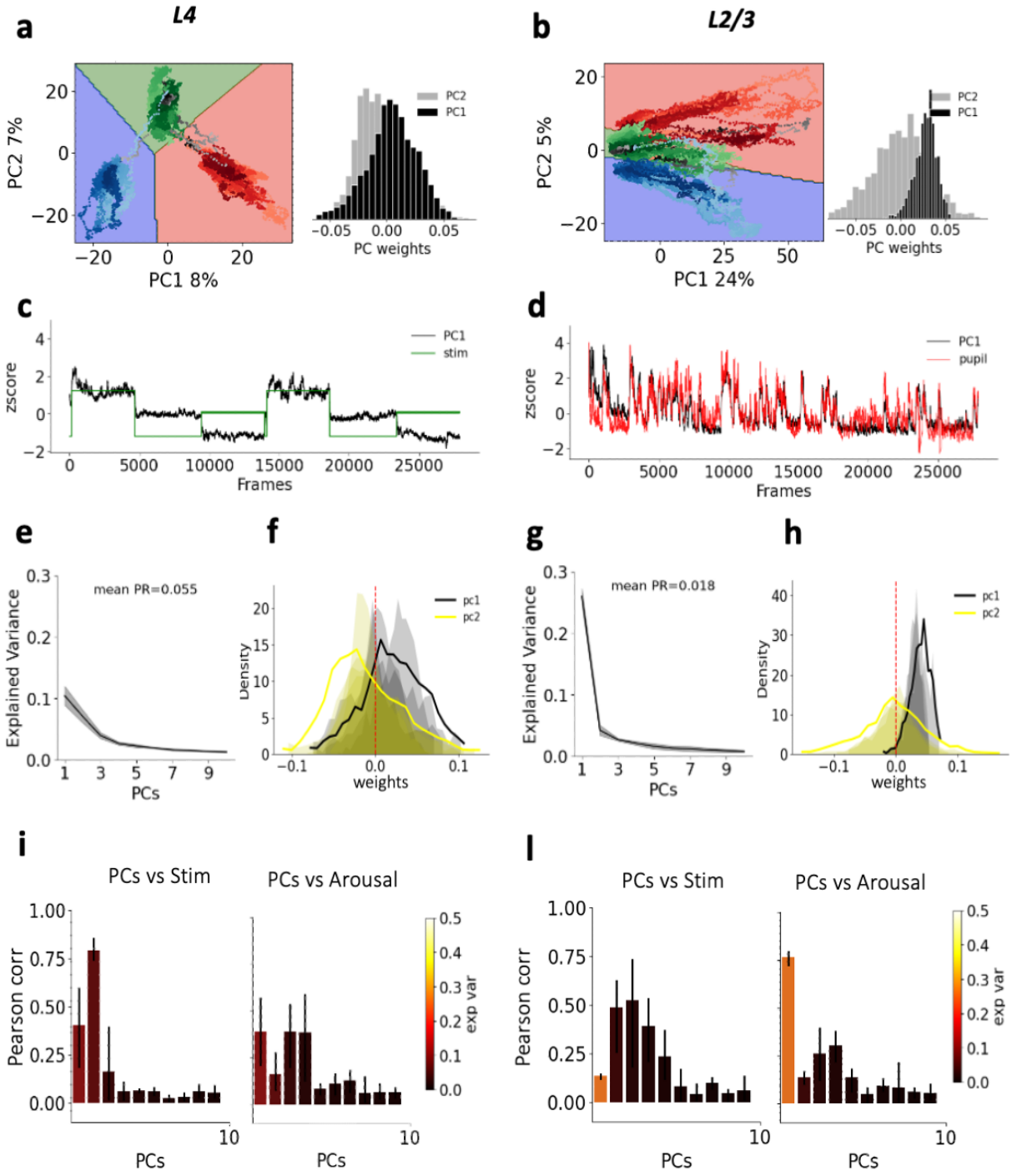

***Figure 3.3 PCA analysis reveals different population geometry in L4 and L2/3***
***a,b)*** *Projection of neural activity onto the first 2 principal components identified by PCA for a representative neural population recorded in L4 (a) and in L2/3 (b). The different epochs of the stimulation protocol are color-coded in the following way: red for plaid epoch, green for the grey epoch and blue for the grating epoch. The coloured subspaces represent the decision boundaries of a multinomial logistic classifier used for decoding the epoch identity only from the first 2 PCs (accuracy=0.97 in L4, accuracy=0.89 in L2/3). The histograms on the right show the distributions of the weights of PC1 (black) and PC2 (grey).* ***c)*** *Black trace: activity of the same L4 neural population showed in a), projected onto its PC1; green trace: time course of stimulus energy, used as a 1-D, continuous scalar measure tracking the protocol progression.* ***d)*** *Same as c but for the L2/3 population showed in b); here the red trace describes the time course of pupil size recorded throughout the stimulation protocol.* ***e,g)*** *Average variance explained by the first 10 PCs for the PCAs independently calculated for all the L4 sessions (e, N=4) and L2/3 (g, N=3); shaded grey area represent the standard deviation for each PC. Average normalized participation ratio is also reported.* ***f,h)*** *Thick lines: average distributions of the PC1 (black) and PC2 (yellow) weights, calculated over all the weights distributions (shaded curves) of the different L4 sessions (f, N=4) and L2/3 (h, N=3).* ***I,l)*** *Histograms reporting the average pearson correlation ± SEM of the neural activity projected onto the first 10 PCs and the stimulus energy or pupil size: each bar represents the average correlation between the 1-D projection onto a single PC versus stimulus or pupil area, averaged across all the sessions recorded in L4 (I, N=4) or in L2/3 (l, N=3); the colour of each bar encodes the amount of variance explained by that PC.*

### 3.3.3. Arousal compresses the dimensionality of the population activity at the second timescale

Following the observation that arousal fluctuations tend to concentrate – especially in L2/3 – the neural variance on a shared activity mode, I then asked whether it can also dynamically reshape the overall dimensionality of the population activity, thus constraining its degrees of freedom. To do that, I quantified the dimensionality of the recorded neural populations separately for periods of low or high arousal, estimating with the PR the number of effective dimensions which significantly contribute to the overall activity. For each session, I selected and concatenated all the timepoints where the pupil area was $< 0.1$ standard deviations above the mean and classified them as *low* arousal state; similarly, timepoints where the pupil size was $> 0.3$ standard deviations above the mean were classified as *high* arousal state and concatenate. I then calculated the PR separately for the two *low* and *high* arousal

matrices, directly estimating the overall dimensionality of the neural populations in the two conditions.

Previous work has shown how arousal modulation in V1 tends to increase the excitability and the firing rates of individual neurons, and how this positive modulation promoted a desynchronized cortical state by reducing the noise correlations between pairs of neurons, effectively increasing the dimensionality and thus improving sensory coding [27,28,38,51,58]. However, I instead found a quite opposite trend.

In L4 neuronal population showed a mild reduction of dimensionality, consistent with the marginal contribution of arousal in driving the neural variance over the leading PCA axis (Fig 3.4 a). Oppositely, L2/3 showed a much more dramatic trend, with the effective dimensionality significatively dropping during the arousal periods compared to the non-arousal (Fig 3.4 b). This result was consistent with the previous observation that arousal seems to drive a single, global activity mode which synchronizes neural activity, and was further confirmed by looking at the correlation structures during low and high arousal, with the strength of the pairwise neuronal correlation increasing during the high arousal periods.

While these results seem, at first glance, to contradict the previous works reporting an exactly opposed trend of how arousal modulates the dimensionality of the population coding, they can actually be reconciled if we make few considerations. First, the strength of correlations is crucially dependent on the arbitrary timescale that the experimentalist assumes is relevant for a particular process [124]. In most of the studies on arousal modulation of cortical processing, the relevant timescale chosen is typically the one underlying fast sensory processing, which operates at the millisecond's timescale. Here however, because of the slow temporal resolution imposed by calcium imaging, I don't access the fast timescale of sensory processing, but instead I can observe the dynamics of the system unfolding at the same timescale of the arousal itself, which fluctuates at the seconds timescales. This means that, while at faster timescales the arousal-induced increase in the population activity promotes fine scale jitters of spike counts and thus neuronal desynchronization, at coarser timescale what emerges is a global and synchronized potentiation of the basal activity.

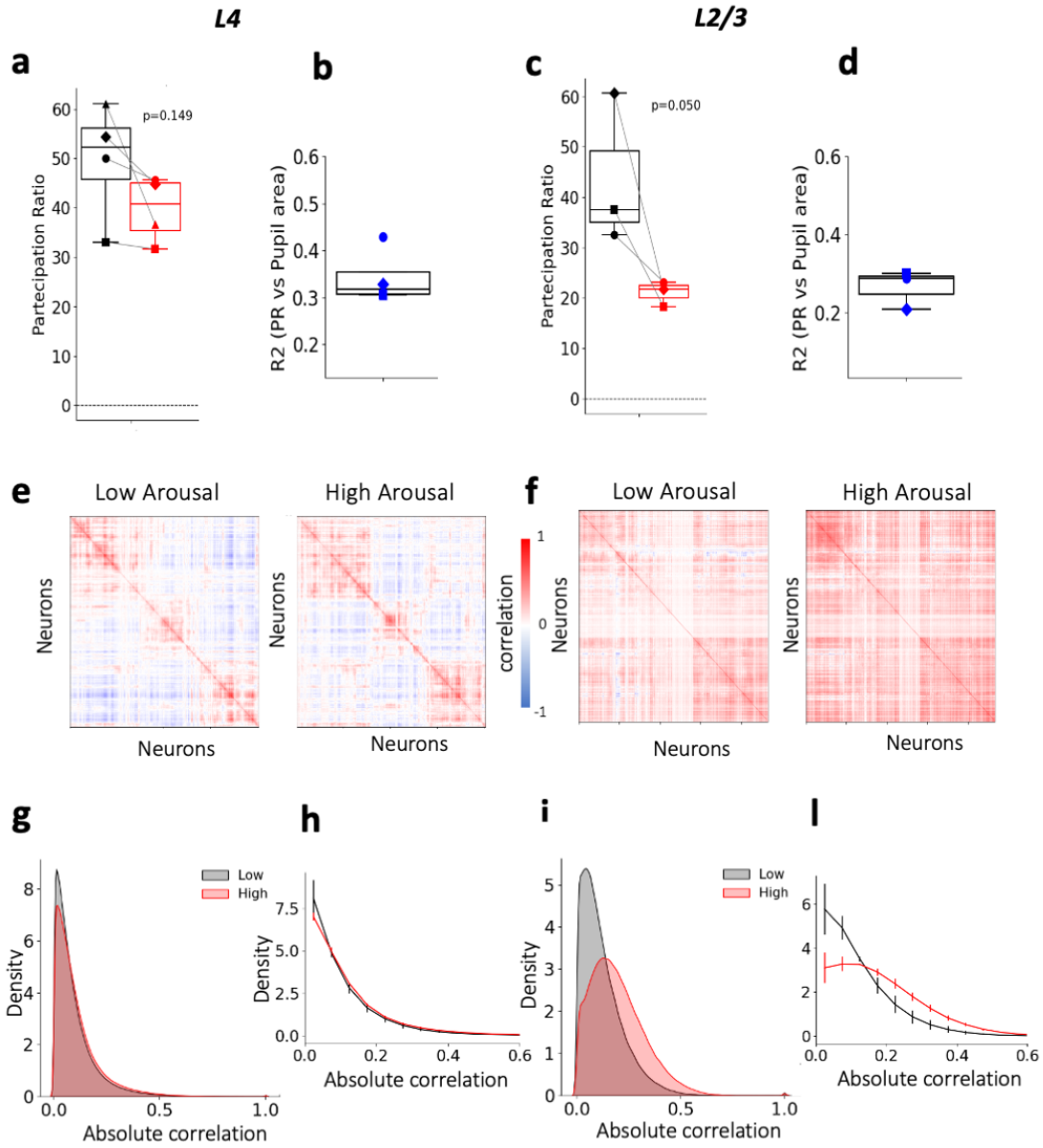


***Figure 3.4: Arousal compresses the dimensionality of population activity***

***a,c)*** *Effective dimensionality of the population activity estimated using the participation ratio on the PCA components, during the periods of low (black box) and high (red box) arousal, for L4 (a, paired ttest p=0.149, N=4) and L2/3 (c, paired ttest=0.05, N=3).* ***b,d)*** *$R^2$ values of a linear model predicting pupil area from the participation ratio values, calculated throughout the recordings using a sliding window of 100 samples (~150 seconds), for the session in L4 (b) and L2/3 (d).* ***e,f)*** *Pairwise correlation matrices calculated between the activity of all the pairs of neurons during the concatenated periods of low (left) and high (right) arousal, for representative sessions recorded in L4 (a) and L2/3 (f).* ***g,i)*** *Distributions of all the absolute pairwise correlation values reported in e) and f) (low arousal in grey, high arousal in red) for L4 (g) and L2/3 (i).* ***h,l)*** *Average distributions calculated, bin by bin, from the absolute pairwise correlation distributions of all the sessions recorded in L4 (h) and in L2/3 (l).*

### 3.3.4. Population encoding of low-complexity sensory input is not impacted by arousal

I showed how arousal shapes the ongoing dynamics of V1 populations by promoting neuronal synchronizations at slow timescales, with L2/3 being particularly affected. A natural question to ask is whether the ability of the population to encode stimulus information can be impaired by this modulation, which effectively reduce the degrees of freedom of the coding space. I fit a logistic linear model during low and high arousal periods separately to predict the stimulus epoch (plaid, grey or grating) from the neural activity recorded during the PGG protocol (Fig 3.5 a). Neither in L4 nor in L2/3, where the arousal-induced compression was more dramatic, the representation of the sensory context was impacted during the high arousal periods (Fig 3.5 b), suggesting the sensory-driven activity and the arousal-driven phasic synchronisation to be largely decorrelated during under this stimulation protocol.

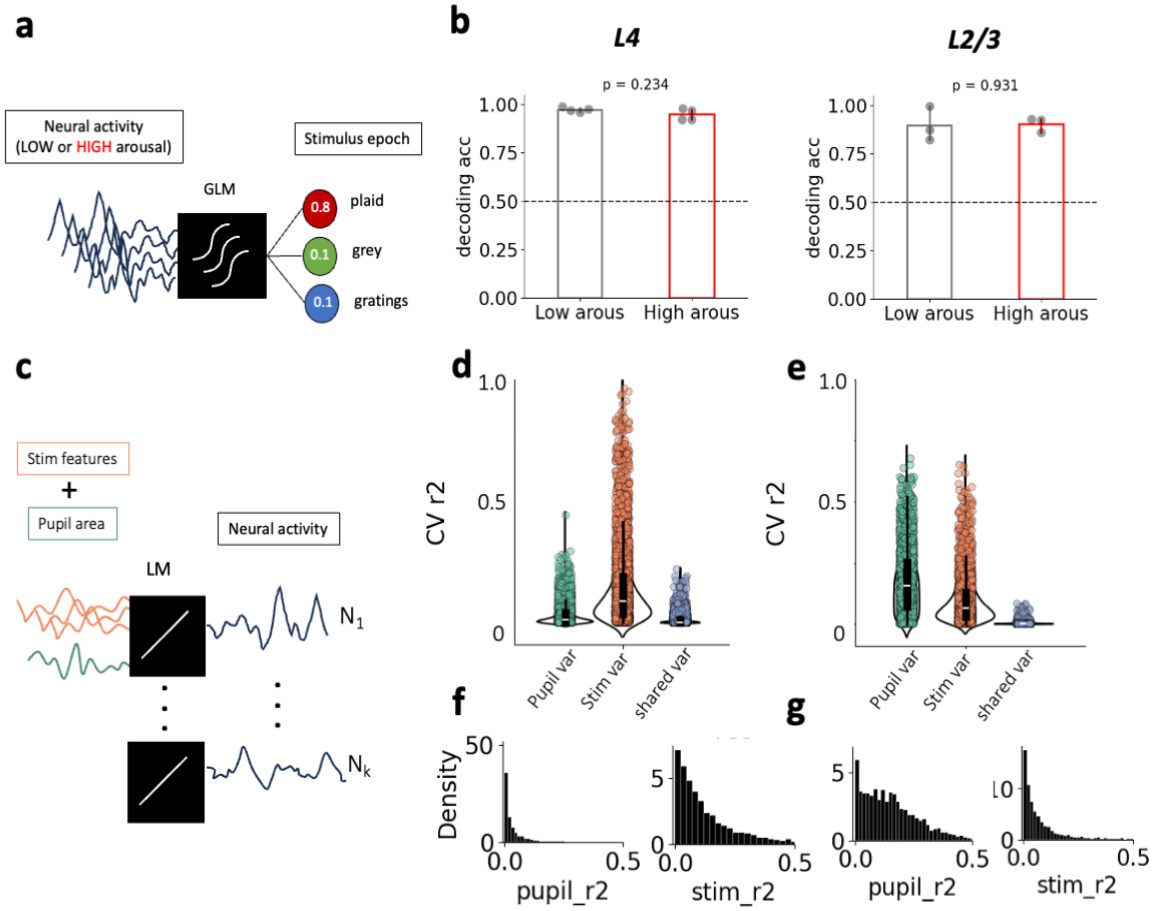


***Figure 3.5 Linear decoding and encoding models***

***a)*** *Schematics of multinomial logistic decoders used for decoding the stimulus epoch (plaif, grey or grating) from the neural activity: the model takes as input the instantaneous population vector at some time t and perform one vs rest classification using a linear model with a sigmoid link function, assigning probabilities at each possible stimulus epoch.* ***b)*** *Decoding accuracies obtained from the logistic decoder using only low (black) or high (red) arousal timepoints, for all the sessions recorded inL4 (left panel) and in L/3 (right panel); p-values from paired ttest are also reported.* ***c)*** *Schematics of the linear encoding models used for performing variance partitioning analysis: three linear models were built: a full model predicting single neuros activity from both stimulus features and pupil size fluctuations, a reduced model predicting single neurons activity from only stimulus features and a second reduced model predicting single neurons activity only from pupil size fluctuations. The three models were then used for estimating the amount of unique variance explained by the stimulus, by the pupil size and the amount of variance that couldn't be unambiguously attributed to either stimulus and pupil, namely shared variance. Panel* ***d)*** *reports the amounts of such variance partitions obtained for each neuron of all the recordings performed in L4, while panel* ***e)*** *reports the same quantification for L4. The same distributions of pupil and stimulus cross-validated variance partitions are reported as histograms in panel* ***f)*** *for L4 and in panel* ***g)*** *for L2/3.*

To further test this, I performed an analysis of the neural variance by isolating the unique contributions of pupil size fluctuation and stimulus. I fit three separate linear encoding models (Fig 3.5 c, see 2.5 Methods section), predicting the activity of each neuron from i) stimulus features only, ii) pupil size only and iii) both stimulus features and pupil size. The fit stimulus-reduced, pupil-reduced and full models were then used to estimate the unique variance explained by stimulus and arousal, and, importantly, the variance shared by the two sets of variables. Coherently to what the PCA analysis revealed previously, for the neurons sampled in L4 most of the variance was uniquely attributed to the stimulus, while in L2/3 it was almost equally distributed between stimulus and arousal. Importantly, In both layers the shared variance was low, indicating that stimulus and arousal independently contributed to driving neural activity (Fig 3.5 d,e).

This last finding suggested that the encoding of slow-changing sensory context and the arousal-driven, low-dimensional shared activity mode I previously described should largely be orthogonal. I then directly addressed it by calculating the angle between the two 1-D neural axes encoding either a 1-D representation of the stimulus (global energy, see 3.5 Methods section) or arousal (Fig 3.6, a,c). Using cross-validated partial least square regression (PLS, see 2.5 Methods section), I estimated the coefficients of such axes for which the projected neural activity better correlated with either pupil size or with stimulus (Fig 3.6 b). I then computed the angle between the two subspaces and estimated the amount of collinearity. In both layers, I found low but significant collinearity ($0.27 \pm 0.04$ SE, N=4 in L4; $0.33 \pm 0.2$ SEM in L2/3, N=3). This confirmed the results from the variance partitioning analysis, showing that the representations of slow-changing sensory context and arousal state are largely independent (Fig 3.6 d). I argue that the small observed collinearity between the two axes might be likely attributed to the increase in arousal that was consistently triggered at the transitions between stimulus epochs in almost all the sessions.

***Figure 3.6 Subspace similarity analysis***

***a)*** *Schematics representing the time course of population activity as a trajectory in a K-dimensional state space (black trajectory), where K is the number of neurons composing the population; the orange and green axes represent, respectively, a 1-D stimulus subspace and a 1-D arousal subspace, defined within the full neural state space.* ***b)*** *Black traces represent the neural activity projected onto the 1-D stimulus axis (top traces) or the 1-D arousal axis (bottom traces) found through cross-validate PLS, from a representative session of L4 (left panel) an L2/3 (right panel); projections on the stimulus subspace were overlayed with the time course of stimulus energy (orange traces), while projections on the arousal subspace were overlayed with the time course of pupil size fluctuations (green traces).* ***c)*** *Schematics representing the subspace similarity analysis, where the cosine angle was calculated between the 1-D stimulus and arousal axes to measure collinearity.* ***d)*** *Boxplots representing the subspaces similarities (ranging from 0 to 1) calculated on all the sessions in L4 (left panel) and L2/3 (right panel); shuffle controls were performed by scrambling either the stimulus or the pupil size prior to PLS fitting and then calculating the cosine angle between the shuffled PLS axis; this operation was repeated 10 times and then the average angle was taken; p-values from paired ttest are also reported.*

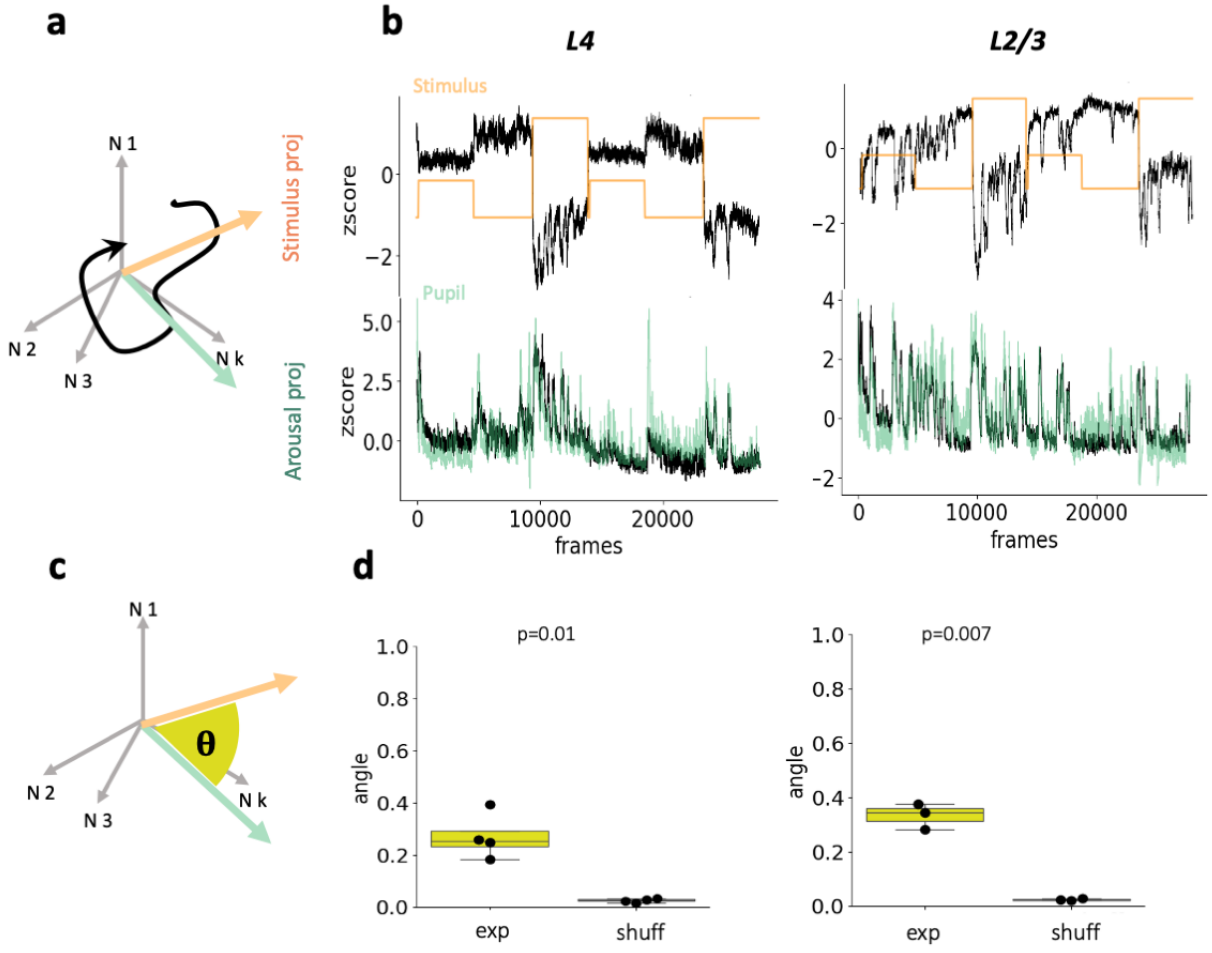

### 3.3.5. Naturalistic stimulation increases arousal-induced dimensionality compression and aligns stimulus-arousal subspaces

In the previous paragraphs I characterized how spontaneous arousal fluctuations affect the structure of the ongoing activity of neural populations during a constant, low-complexity stimulus drive, but what happens during more naturalistic stimulation? To address this question, I recorded the activity of the same neuronal populations while presenting two different naturalistic stimuli. The first one consisted in an uninterrupted, 5 minutes long video showing a countryside view from a train window, with static camera (TRAIN); the second consisted in ~4 minutes showing the single-shot opening scene from the movie "Touch of evil" (TOE, Orson Welles, 1958), often used in visual neuroscience for providing short (usually ~1 sec) naturalistic stimulation.

As expected, the two naturalistic stimuli evoked qualitatively different population responses in L4 and L2/3 (Fig 3.7 a, b). Like for the simple stimulus with plaid-grey-gratings (PGG), the neural activity in L4 looked more heterogeneous and desynchronized compared to L2/3, where in turn arousal synchronously potentiated the overall population activity through a one-dimensional, shared activity mode captured by PC1 (Fig 3.7, f). Interestingly, for the TRAIN stimulus, PC1 jointly correlated with both arousal and global stimulus statistics such as mean luminance, both in L4 (Fig 3.7 c, e) and, more mildly, in L2/3 (Fig 3.7 d,f).

Analysis of population dimensionality during low/high arousal periods in L4 showed a sharp increase in the effective dimensionality of the population code during naturalistic stimulation, with TOE stimulus showing maximal PR values during low arousal. Notably, the amount of reduction in the effective dimensionality during high arousal seemed also to scale with stimulus complexity, suggesting a possible interaction between stimulus richness and arousal-induced compression of the population activity (Fig 3.8 a). Conversely, in L2/3 such relationship seemed to be weaker, with arousal impacting the effective dimensionality similarly across stimulus complexity (Fig 3.8, b).

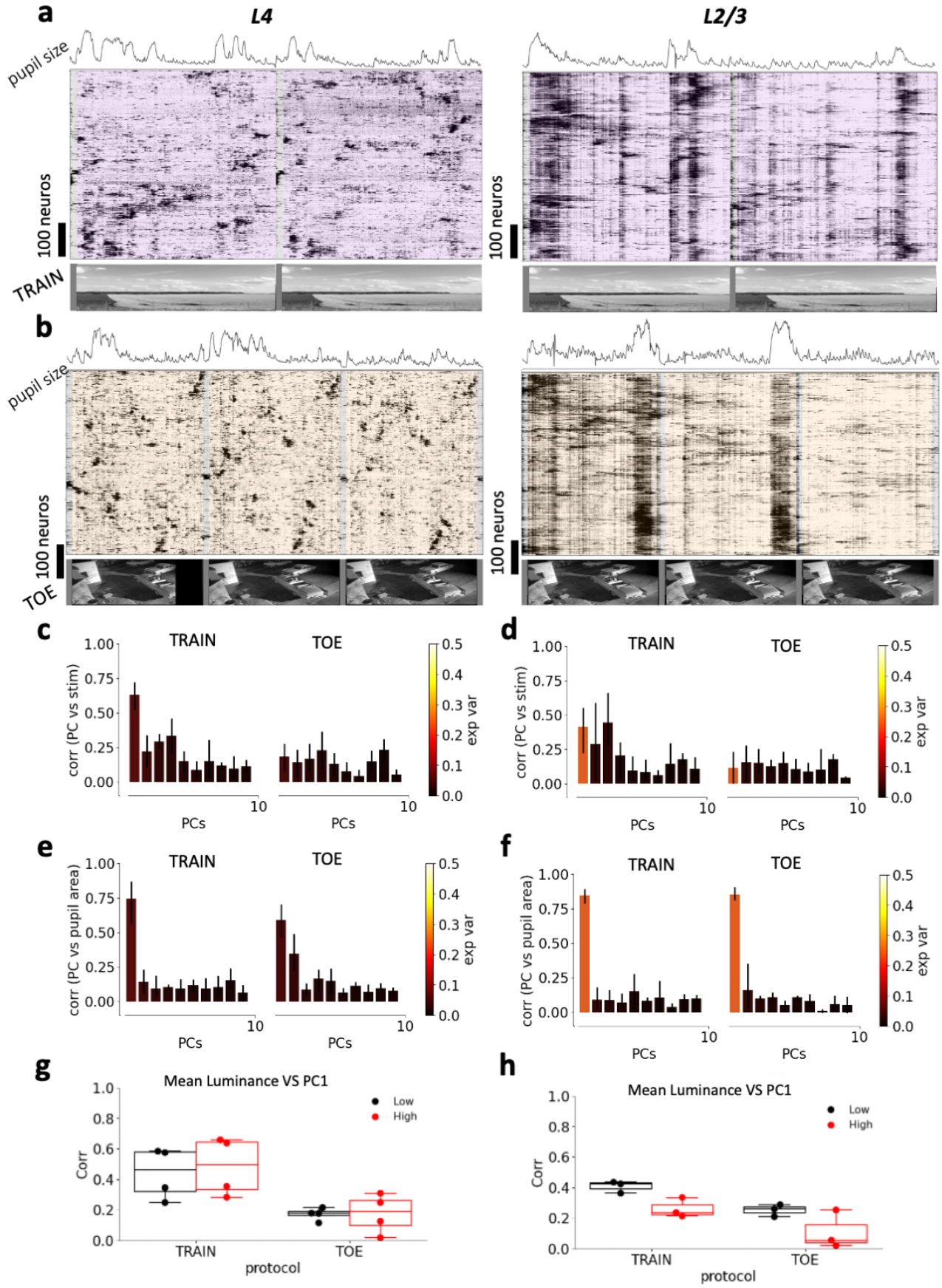
a
L4
L2/3
pupil size
100 neuros
TRAIN
b
pupil size
100 neuros
TOE
c
TRAIN
TOE
corr (PC vs stim)
exp var
PCs
d
TRAIN
TOE
corr (PC vs stim)
exp var
PCs
e
TRAIN
TOE
corr (PC vs pupil area)
exp var
PCs
f
TRAIN
TOE
corr (PC vs pupil area)
exp var
PCs
g
Mean Luminance VS PC1
Low
High
Corr
TRAIN
TOE
protocol
h
Mean Luminance VS PC1
Low
High
Corr
TRAIN
TOE
protocol

***Figure 3.7 L4 and L2/3 populations activity during sustained, naturalistic stimulation***
***a)*** *Heatmaps reporting the z-scored neural activity of ~ 500 neurons recorded simultaneously in a representative session of L4 (left panel) and L2/3 (right panel), while presenting two repetitions of the TRAIN naturalistic stimulus. Black traces on top of the heatmaps represents the fluctuations of pupil size, while the schematics below the heatmaps represent the epochs of the stimulation protocol.* ***b)*** *Same as a) but for the TOE naturalistic stimulus.* ***c,d)*** *Barplots reporting the average pearson correlation (± sd) between the 1-D neural activity projected onto each of the first the PC and stimulus (global mean luminance); the average was calculated using all the sessions recorded in L4 (c, N=4) and in L2/3 (d, N=3); the colour of each bar is indicative of how much variance that specific PC explained.* ***e,f)*** *Same as c,d) but reporting the correlation between the PC projections and the pupil size time course.* ***g,h)*** *Boxplots reporting the absolute correlation coefficients between the neural activity projected onto PC1 and the stimulus mean luminance; the PCs and correlation coefficients were separately calculated for the concatenated periods of low (black boxes and dots) and high (red boxes and dots) arousal, for the different protocols and for L4 (g, N=4) and L2/3 (h, N=3) animals.*

Variance partitioning through linear encoding models showed a larger amount of unique stimulus variance compared to arousal-related variance in L4, and a more equal variance partitioning between stimulus and arousal in L2/3, coherently to what was found previously for the PGG stimulus (Fig 3.8, c, d). The models were trained both using fine-scale and coarse stimulus statistics, yielding similar results. Interestingly, I also observed a general increase in the amount of shared variance between stimulus and pupil size variables in both layers, exception made for TOE stimulus in L4, indicating a possible overlap between arousal state and stimulus representations. To test this, I performed a PLS regression as previously done for PGG, obtaining two 1-D subspaces where the projected activity correlated well, respectively, with arousal fluctuations and a single, global stimulus statistics such as mean luminance. Surprisingly, I found that the overlap between the two neural axis was in general consistently larger than the one found with the PGG stimulus. The TRAIN stimulus, particularly, showed very high collinearity between the mean luminance axis and the arousal axis (similar results were found using stimulus energy instead of mean luminance as 1-D stimulus statistics). This finding suggested that under naturalistic stimulation, the spontaneous fluctuations in the arousal state, and in turn the low-dimensional activity mode it generates in V1 populations, can track and correlate with low-dimensional stimulus representations.

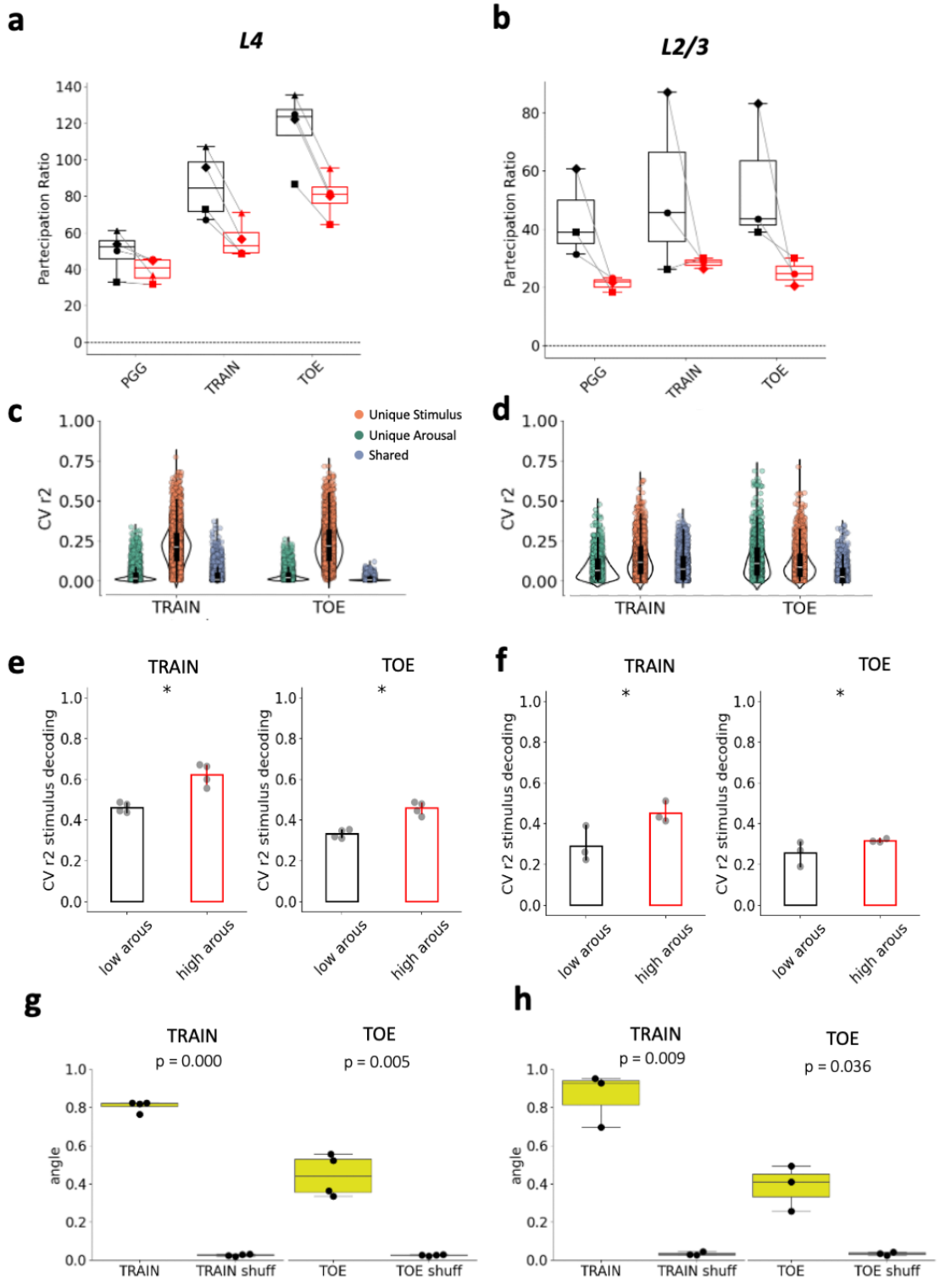


***Figure 3.8 Analysis of dimensionality, variance partitioning and subspaces alignment in cortical populations during sustained, naturalistic sensory drive.***

***a,b)*** *Analysis of the effective dimensionality of the population activity, estimated by the participation ratio calculated over the PCA components, during low-complexity (PGG), TRAIN and TOE stimulation*

*protocols, during low (black boxes) or high (red boxes) arousal periods. We can appreciate how the effective dimensionality clearly tends to scale with stimulus complexity in L4 (a) and less in L2/3 (b); Also, the amount of arousal-induced dimensionality reductions seems to increase for more complex stimuli in L4, while always reach relatively low, baseline values in L2/3.*
***c,d)*** *Variance partitioning analysis as described in Fig 3.5c, performed at the single-neuron resolution over the recorded neural activities during the TRAIN and the TOE protocols, separately for L4 (c) and for L2/3 (d); notably, the amount of shared variance generally increased in both layers, except for the TOE protocol in L4.* ***e,f)*** *Cross-validated performances of a linear model trained to decode the stimulus features from the raw neural activity, for both the naturalistic stimuli TRAIN and TOE.* ***g,h)*** *Analysis of the similarity between the 1-D stimulus axis (PLS over the global mean luminance or energy) and 1-D arousal axis (PLS over pupil size), as for Fig 3.6; compared to the low-complexity PGG protocol, both naturalistic protocols generated higher collinearity between the two subspaces, with the TRAIN protocol generating almost perfect overlap.*

In fact, there was a generally good correlation between the time course of pupil size and some of the global stimulus statistics in both the L4 and L2/3 datasets (particularly mean luminance and motion energy, Fig 3.9 a, b). Importantly, the pupil size fluctuations driving such correlation were large and also correlated with locomotion speed, thereby suggesting that were likely representative of arousal state fluctuation rather than simple light reflex dynamics (Fig 3.9 c, d). To further exclude the possibility that the collinearity between the stimulus and arousal axes could be trivially explained by PLR-induced responses, I repeated the subspace analysis using locomotion speed instead of pupil size as arousal proxy. The results didn't change qualitatively, with the TRAIN protocol showing high degree of collinearity between the two 1-D axes (Fig 3.9 e, f). Moreover, it is important to note that the correlation between the PC1 projection and mean luminance was present also during periods of low-arousal, suggesting that the representation of such global stimulus statistics was not just inherited by the arousal modulation (Fig 3.7 g, h). From this perspective, during engaging and rich sensory experience, V1 populations could be able to simultaneously represent i) high-dimensional, local features through a fast, high-dimensional population code (the classic form of visual encoding, not currently characterized in this study), and ii) low-dimensional, higher-level statistics of the sensory input through a slower, low-dimensional population activity mode. The collinearity I found between the 1-D subspaces underlying the representations of global stimulus statistics (likely locally computed) and arousal state (carried by the noradrenergic system) suggests that information is shared between the two processes, opening the question of how these two systems may interact and influence each other.

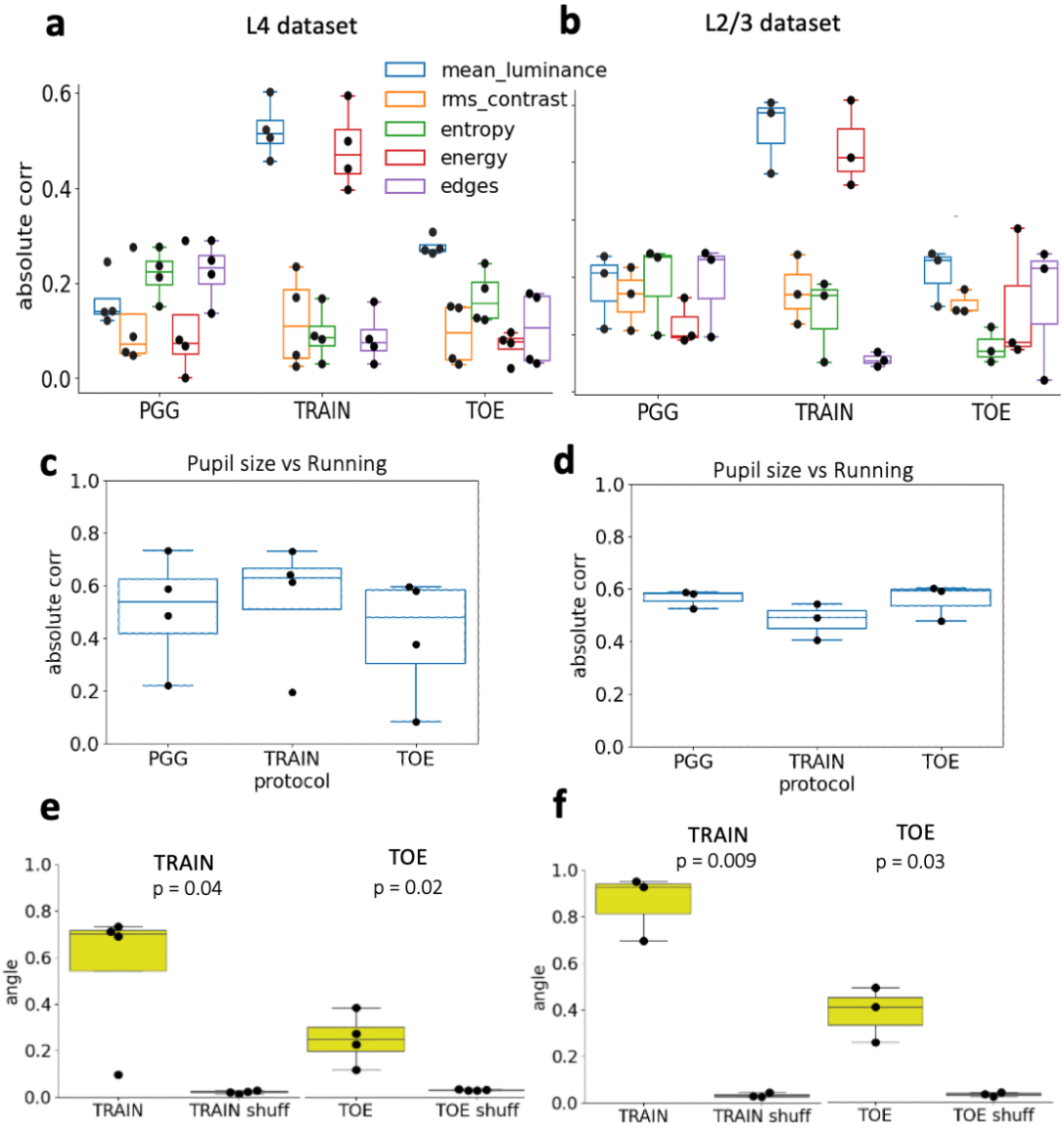


***Figure 3.9 Correlations between sensory and arousal-related variables.***
***a,b)*** *Boxplots showing the absolute correlation between the time course of different stimulus statistics (calculated over the each frame of the different stimulation protocols) and the time course of pupil size. Interestingly, for the naturalistic stimuli TRAIN and TOE, the energy and mean luminance time courses correlated with pupil fluctuation. Since the amplitude of the pupil fluctuations was large and generally correlated with locomotion speed as reported in* ***c)*** *and* ***d)****, I exclude the possibility that they were simply driven by the light pupillary reflex, but instead reflected internal arousal fluctuation. Such correlation between sensory features and arousal fluctuations can, at least partially, explain the high collinearity observed between the stimulus and arousal subspaces.* ***e,f)*** *Boxplot showing the angles between the 1-D stimulus and arousal subspaces for the TRAIN and TOE protocol, independently calculated for each session recorded in L4 (e) and in L2/3 (f); in this case the arousal axis was identified by using locomotion speed instead of pupil size, excluding the possibility that the collinearity between the subspaces could be trivially explained by PLR-induced response*

## 3.4. Discussion

In this study, I investigated how arousal and locomotion reshape population activity in mouse primary visual cortex (V1) during sustained, continuous visual stimulation. Moving beyond trial-averaged paradigms, I analysed the geometry and dimensionality of ongoing population activity across cortical layers while presenting stimuli of varying complexity. I found that arousal drives a single shared activity mode that globally increases activity across layers, but reorganizes population geometry in a layer- and stimulus-dependent manner. While L4 activity remains largely dominated by stimulus dynamics under simple stimulation, superficial layers (L2/3) exhibited strong arousal-related dimensionality compression, challenging the classic notion of arousal always expanding the dimensionality of the population activity. Under naturalistic stimulation, arousal-related activity becomes increasingly aligned with low-dimensional stimulus representations in both layers, suggesting that state-dependent modulation can track higher-order stimulus features. These findings extend current views of state-dependent sensory processing by revealing how internal states dynamically reshape cortical population geometry under continuous sensory drive.

A large body of work has demonstrated that arousal modulates firing rates, variability, and noise correlations in visual cortex [28,38,58,60]. These studies, however, have primarily relied on brief, repeated stimulus presentations, characterizing state effects via trial-averaged responses and residual fluctuations. Within this framework, internal state is typically treated as a contextual modulator of stimulus encoding. Continuous stimulation, on the other hand, can reveal a complementary picture. Under sustained sensory drive, neural activity cannot be decomposed cleanly into "signal" and "noise" or "evoked" and "spontaneous" components. Instead, stimulus dynamics and state fluctuations coexist on overlapping timescales. By analysing single-trial population trajectories, I showed that arousal does not merely scale stimulus responses, but reshapes the geometry of population activity over seconds-long windows. These results can complement the previous works on arousal modulation of sensory coding, suggesting that under continuous stimulation, state-related dynamics actively restructure the neural manifolds rather than simply altering the background variability.

The datasets I collected reveal striking laminar differences in how arousal shapes population geometry. In layer 4, neural variance during simple stimulation is largely explained by stimulus dynamics, and arousal contributes only marginally to the dominant population dimensions. In contrast, superficial layers exhibit a strong low-dimensional shared mode tightly coupled to arousal. This laminar dissociation is consistent with known circuit architecture. Layer 4 receives dense thalamocortical input and is traditionally viewed as the principal feedforward input layer [20]. Superficial layers integrate feedforward input with long-range corticocortical and neuromodulatory afferents [125]. Particularly, neuromodulatory projections from locus coeruleus, basal forebrain, and other systems preferentially target superficial layers [27,120], providing a plausible anatomical substrate for stronger state-dependent modulation of neural activity in L2/3. My findings therefore support the idea that internal state signals are differently integrated along the cortical hierarchy, exerting stronger influence in layers specialized for integrative and recurrent processing.

A central observation of this study is that arousal reduces population dimensionality at slow timescales in superficial layers, despite increasing overall activity. At first glance, this appears to contradict prior work reporting that arousal desynchronizes cortical activity, reduces correlations, and increases effective dimensionality [51,60]. I propose that this discrepancy reflects a fundamental timescale dependence. Electrophysiological studies typically assess correlations and dimensionality at millisecond resolution, capturing fast fluctuations in spike timing. In contrast, calcium imaging integrates activity over longer windows, better revealing slower activity modes. At fine timescales, arousal reduces shared variability and decorrelates spike counts, increasing high-frequency coding capacity. At slower timescales, however, arousal introduces a coherent low-dimensional modulation that dominates variance and compresses the population activity. Thus, arousal does not uniformly expand or compress dimensionality. Instead, it reorganizes activity across temporal scales: enhancing high-dimensional fast sensory coding while simultaneously embedding a slow, low-dimensional global mode. This interpretation reconciles my findings with prior results showing arousal inducing a desynchronized cortical state, and suggests that dimensionality is not a fixed property of cortical circuits but depends critically on temporal coarse-graining.

Another interesting observation emerged from this work is that under simple stimuli, the dominant low-dimensional stimulus representation remains largely orthogonal to the arousal mode, indicating that global stimulus encoding and state modulation are separable dimensions. However, when stimulus complexity increases (e.g., naturalistic movies), the global stimulus axis becomes more aligned with the arousal-related shared mode. This alignment suggests that arousal-related modulation can track low-dimensional global features of the stimulus, such as major qualitative transitions in the visual scene, which I speculate could be linked to sensory predictability and novelty. Supporting this hypothesis, neuromodulatory systems, particularly noradrenergic system, have been implicated in signalling salience, uncertainty, and environmental volatility [37]. Moreover, pupil-linked arousal fluctuations have been shown to directly correlate with stimulus salience and surprise [39].

Following these observations and putting them in the context of this work, one could say that the arousal-related global state signal embeds in V1 population geometry a low-dimensional representation of environmental predictability. During the PGG stimulation, which features long (5 minutes) epochs of highly repetitive visual input, the arousal events did not correlate with stimulus statistics, potentially meaning that the arousal system was driven by other (more informative) sensory modalities. During the TRAIN protocol, however, the fluctuations in the arousal state correlated well with low-dimensional statistics of the stimulus such as mean luminance and motion energy, which reflected in high alignment of the coding subspaces. During the TOE protocol, the correlations between stimulus and arousal decreased again, together with the alignment of the relative subspaces. This trend is particularly interesting if we consider the effect that a sensory input can have on a neural population: if the information content of the input can be compressed, then the resulting neural representation can be low-dimensional, with many neurons covarying together, avoiding wasteful high-dimensional population activity which would not improve the encoding. On the other side, if the sensory input is not compressible it cannot be represented with a low-dimensional population code without losing information, and thus needs a population code with more degrees of freedom, enabling explicit and parallel representations of multiple features. I speculate that if the stimulus is engaging and evolves with some degree of unpredictability and its relevant dynamics (like sudden, unexpected transitions) can be represented with a low-dimensional population code (such as low-dimensional activity tracking the mean luminance profile), the resulting low-dimensional signal could more easily

propagate to other areas and embed the same, low-dimensional representation of the environmental volatility. This notion is in line with evidence on how low-dimensional activity states propagates throughout the cortex, creating spatial-temporal patterns of correlated activity[56,62,126]. In the case of the TRAIN stimulus, the unpredictable changes in the stimulus content can be well approximated simply by the mean luminance transitions (the flow of motion is constant and unidirectional, and the overall spatial structure of the stimulus is conserved in time); this could make the low-dimensional luminance encoding to be used as a general proxy for meaningful changes in the environment, as the measured correlation between mean luminance, neural activity and arousal suggests. When it comes to the TOE protocol, however, this does not happen: under this framework, I speculate that since the information content of the stimulus is in this case highly complex and thus harder to compress, the population activity in V1 mostly fails in creating low-dimensional modes that can effectively track the stimulus volatility. This framework tries to link the emergence of internal states to the notion of (sensory) input compressibility leading to local low-dimensional activity.

While these ideas are largely speculative, they could be tested by designing experiments and analysis approaches to: i) better characterize stimulus compressibility and its relationship with the emergence of stimulus-driven low-dimensional activity, ii) check the consistency of the correlation between arousal dynamics and low-dimensional sensory representations, iii) track the propagation of such low-dimensional signals across different stages of the sensory processing and iii) perturb the neuromodulatory system to test its role in the signal propagation and reinforcement.

Moreover, several important improvements can still be made to increase the quality and interpretability of the presented findings. First, neural activity was measured using two-photon calcium imaging, which inherently imposes temporal filtering due to the kinetics of calcium indicators. As a consequence, the analyses primarily capture population dynamics at slow timescales (hundreds of milliseconds to seconds), avoiding a direct comparison with the previous electrophysiological studies showing fast decorrelation effects [51,60]. Integrating the current dataset with electrophysiological recordings could therefore be highly beneficial to fully characterize how arousal reorganizes population geometry across temporal scales. Second, arousal was inferred through behavioural proxies (e.g., locomotion, pupil dynamics), which correlate strongly with neuromodulatory activity but do not provide direct

measurement or causal manipulation of specific neuromodulatory systems. The interpretation that low-dimensional shared modes reflect noradrenergic or cholinergic influences is consistent with prior work [37,39,27], but remains indirect. Future studies combining large-scale imaging with targeted manipulation of neuromodulatory nuclei would allow causal testing of whether the observed low-dimensional mode is driven by specific neuromodulatory afferences.

Despite these limitations, the present work establishes that internal state signals are embedded in cortical population activity as dominant low-dimensional modes which interact with sensory representations in a stimulus- and layer-dependent manner. Moreover, such activity modes operate at coarser temporal and functional scales than those characterizing canonical sensory coding, providing a possible substrate for hierarchical encoding of sensory information. By shifting from trial-averaged analyses to characterisation of continuous population geometry, this study provides a framework for investigating how cortical circuits multiplex information across temporal scales and integrate sensory and non-sensory signals under naturalistic conditions.

# 3.5. Methods

## 3.5.1. Experimental procedures

All the experiments were carried out in accordance with European Union Directive 2010/63/EU and under the approval of the EMBL Animal Use Committee and the Italian Ministry of Health License 23- 004_RM_SR. C57BL/6-J mice were used in the study.

### 3.5.1.1. Brain injections

To label V1 excitatory neurons in L2/3, 200 nl of AAV9-hSyn-GCaMP8f ($1x10^{13}$ vg, Addgene), was injected in the V1 area of the right hemisphere. Mice were first anesthetized using FMM (10 ul/g bw, formulation as described above) and head-fixed in a stereotaxic frame, while keeping the body temperature to 37°C using a heating pad. The hairs were removed and the skin cleaned with iodopovidone (betadine, Pharmavola, cat. 023907292). After performing a single incision with a scalpel, the skull was exposed, cleaned with 0.9% saline and aligned. Three small holes were made around a centre point at -3.80 AP, -1.30 ML with a 30G needle, taking care of not piercing the dura, above the V1 area of the right hemisphere. 100 nl of virus were then delivered in each hole at ~500 um from the dura through a pulled glass needle using an automatic injector (Nanoliter 2020 injector, WPI cat. 300704), at a flow rate of 10 nl/s. The glass needle was kept in place for 5 minutes after each injection. After the injections, the skin was sutured. Animals were then injected subcutaneously with buprenorphine and allowed to recover.

### 3.5.1.2. Cranial window implantation

After 4 weeks from the brain injection, a cranial window was opened above the surface of V1, to allow 2-photon recordings of V1 cell bodies. Mice were anesthetized with FMM (10 ul/g bw) and placed on a heating pad set to 37°C on a stereotaxic apparatus. After the hairs were removed and the skin cleaned with iodopovidone (betadine), the skull was exposed and aligned. A 4 mm diameter craniotomy was drilled above the right V1 area, cantered at -3.80 antero-posterior and -1.3 medio-lateral from bregma. The medial and posterior sinus were used as landmarks, marking the medial and posterior edges of the craniotomy. A glass coverslip was gently pushed on the surface of the cortex, and then glued to the skull using cyanoacrylate glue. The head plate was then positioned and fixed using dental cement. At the end of the surgery, mice were injected subcutaneously with 10% buprenorphine, and allowed to recover for 5-7 days.

### 3.5.1.3. 2-photons calcium imaging

2-photon calcium imaging was performed using a resonant scanning 2-photons microscope (Neurolabware, custom designed) with a 16x, 0.80 NA, 3.0 mm WD water-dipping objective (Nikon, cat. MRP07220). GCaMP molecules were excited using a Ti:Sapphire laser (Coherent, Chameleon Vision II, 80 MHz) at 920 nm and images were collected using Scanbox software (Neurolabware) at 15.6 Hz 655 x 510 pixels/frame. The recordings were performed at 1 or 1.4 digital zoom. For all the sessions with the PGG stimulus, the recordings were performed at two focal planes in order to increase the number of recorded neurons, using an electric-tuneable lens and reducing the framerate at 7.8 Hz. The imaging planes were spaced around 90 um. In order to avoid light from the stimulation to leak into the PMTs during the recording, all the three LCD monitors composing the stimulation apparatus were modified by gating the backlight driver circuit using a TLL coming from the resonant scanner. In this way, we forced the monitors to flicker and to turn on only during the retrace periods of scanner, i.e. when there was no excitation and the PMT was not acquiring.

#### 3.5.1.4. Data preprocessing

The raw fluorescence video were first registered for motion correction on the x/y plane and then the cell masks were extracted using Suite2p [127]. The segmentation of the cell bodies was performed using Cellpose [115]on the mean projection of the registered video. For the recording with multiple planes, Suite2p was use in multiplane mode; following the independent processing of the planes, the extracted traces were then aligned, up-sampled at 15.6 Hz and finally combined in a single neural matrix for further data analysis. Importantly, the neural traces used were not filtered according to stimulus responsivity, but only by the quality of the morphological properties of the mask, which was manually checked during segmentation. This ensured a more comprehensive and unbiased analysis of the recorded population, agnostic to the tuning properties of individual neurons.

#### 3.5.1.5. Videography and pupil tracking

During the calcium imaging sessions, behavioural videos were also recorded in order monitor the pupil size fluctuations and gaze position during of the eye contralateral to the imaged hemisphere. To do so, I used a camera equipped with a NIR-enhanced CMOS sensor (Basler acA1300-60gmNIR), a 100 mm f/2.8 lens (MVL100M23, Thorlabs) and a 850 nm bandpass filter (Thorlabs, cat. FBH850-40) placed between the sensor and the objective lens. The eye was illuminated using an infrared lamp, and a short-pass dichroic mirror (Edmund Optics, cat. 69-219) was placed in front the eye for redirecting the NIR light to the cameras, positioned behind the animal. This was necessary in order not to obstruct the visual field of the animal with the camera body. The acquisition of each frame of the camera was synchronized with the acquisition of the frames of the microscope, aligning the eye videos with the 2 photons recording. The video was then pre-processed in orded to adjust luminance and contrast for optimizing the pupil and eye segmentation, performed using a custom made Python script, based on a pre-trained CNN developed by [114]. The pupil area was calculated by fitting an ellipse to the mask predicted by the algorithm. The corners of the eye were also tracked, and used to estimate the absolute area of the pupil in $mm^2$, as well as the relative horizontal gaze excursions around the centre of the eye in mm.

### 3.5.1.6. Locomotion tracking

During each experimental session the running speed of the animal on the circular treadmill was also measured. To do so, I coupled an optical rotational encoder to the wheel of the treadmill. This device generates an analogue signal encoding the period of its rotation that is sent to an Arduino board, which I programmed for estimating the instantaneous velocity in cm/s. The logging of the instantaneous treadmill velocity was controlled by the same sync TTL generated by the microscope at 1x framerate which was used for driving the behavioural camera acquisition, effectively synching all the three data streams.

### 3.5.1.7. Visual stimulation

The visual stimuli were shown on a stimulation apparatus composed of three LCD monitors (Dell SE2222H 21.5" 1920x1080, 60Hz) surrounding the mouse and covering most of the visual field. The centre of each monitor was set at ~30 cm from the head of the animal. All the stimuli were rendered and projected using a custom-built python program based on OpenGL and PyQt packages. For each stimulus, the textures were stored as uncompressed, raw matrices for avoiding any latency during the rendering. The sync TTL generated by the microscope at 2x the framerate (~30 Hz) was then used for driving the rollout of each frame, ensuring proper synchronizations with all the other data acquisition systems.

The stimulation protocols used in this study included the following:

**PGG**

This was the low-complexity stimulation protocol, composed of three different stimuli: a moving Plaid pattern, a static Grey background and a moving, vertical Grating pattern, each one lasting 5 minutes. The plaid pattern was built by overlapping two grating patterns (sf=0.13) drifting in opposite

vertical directions, with orientations 110 and 80 degrees respectively, forming an angle of 20 degrees between each grating component. The second component was set with a transparency value of 0.5. This resulted in a plaid pattern composed by white, black and grey rhombus stably drifting horizontally from left to right. The grey stimulus background simply consisted in a static, full field background with a luminance set to ~30 LUX. Finally, the moving grating stimulus consisted in a vertical grating pattern (sf=0.13) drifting from left to right at 2 cycles/s. The stimuli textures were first generated using the Psychopy package and then saved as uncompressed matrices. Finally, the protocol was assembled by concatenating the three stimuli in the following sequence: Plaid-Gray-Grating-Plaid-Gray-Grating; 10 seconds of static grey background were interleaved between each stimulus repetition as interstimulus interval.

**TRAIN**

This was the first naturalistic stimulus, generated by using a free movie recorded from the side window of a moving train. The reason why I chose this video was to have a stimulus with a statistical complexity that would place it somewhat in between an artificial, simple stimulus such as the PGG and a full, complex naturalistic stimulus. In fact, the video was characterized by a constant, unidirectional optical flow (from right to left), and there was a quite stable spatial and temporal distribution of pixel intensities (the upper half pixels in each frame was generally brighter than the lower half, because of the sky/ground separation); however, random, sudden perturbations of these statistics occurred when natural elements such as trees or buildings sporadically entered the field of view, unpredictable stimulus dynamics typical of naturalistic scenes. Also in this case, the stimulus lasted 5 minutes, and the protocol consisted in 2 repetitions of the stimulus, interleaved by 10 seconds of grey background.

**TOE**

This stimulus featured the full opening scene of the movie "Touch of evil" (Orson Welles, 1958), widely used in the visual neuroscience field as naturalistic stimulus, even though only small sections of the scene are usually used. The full scene is a ~4 minutes-long, uncut scene filmed in a single, continuous shot. The video is characterized by naturalistic elements moving in different directions, at different velocities and with highly complex spatial-temporal

distributions of pixel intensities. These features, together with the fact that the all the visual features evolve smoothly in time without sudden interruptions due to scene cuts, make this video ideal for providing a complex stimulation which closely mirrors the statistics of natural viewing. The protocol was assembled by concatenating three repetitions of the stimulus, interleaved by 10 seconds of grey background.

### 3.5.2. Data Analysis

All the data analysis performed in this work was performed with custom-written python scripts, mainly based on the numpy, sklearn and scipy packages.

#### 3.5.2.1. PCA analysis

PCA is a powerful and highly interpretable tool for exploring the intrinsic structure of neural population dynamics. In this study it was used in its classic form by performing the eigen decomposition of the covariance matrices of neural activity through singular value decomposition (SVD). PCA thus provides an orthogonal linear decomposition of the neural state space, revealing the dominant axes along which population activity varies and quantifying the fraction of total variance captured by each axis. Changes in the spectrum of eigenvalues reflect reshaping of the population manifold; generally, a dominant first eigenvalue indicates the presence of a strong low-dimensional shared mode, while a flatter spectrum indicates higher-dimensional, distributed coding. In the context of this study, PCA was used to separate independent (input-driven) modes of activity of a neural population. This was helpful for identifying, without any priors or assumptions, low-dimensional shared fluctuations across neurons driven by either stimulus or internal states, as well as providing a basis for estimating the effective dimensionality of the population activity. For each recording session and condition, neural activity was organized into a data matrix

$$\mathbf{X} \in \mathbb{R}^{\mathbf{T}\times\mathbf{N}}$$

where T is the number of timepoints, N is the number of neurons and $X_{ti}$ represent the activity of neuron i at time t. The activity of each neuron was then z-scored prior to PCA

$$z_i = \frac{(x - \bar{x}_i)}{\sigma(x_i)}$$

where $\bar{x}_i$ is the mean over time of the neuron $x_i$ and $\sigma(x_i)$ is its standard deviation. This step leads PCA to effectively give the eigen decomposition of the sample correlation matrix R instead of the raw covariance matrix, defined as

$$R = \frac{1}{n-1} Z^T Z$$

PCA was then computed and the neural activity was projected onto the first 2 PCs for visualiz
or arousal state was carried by each PC, I computed the Pearson correlation values between sti
analysed PCs.

### 3.5.2.2. Dimensionality analysis

While PCA reveals the ordered structure of variance across orthogonal axes, it does not by itself provide a single scalar estimate of dimensionality. In the context of this study, I sought to quantify how arousal reshapes the geometry of population activity, specifically whether it expands or compresses the effective dimensionality of the neural manifold. To quantify the effective dimensionality of neural population activity, I then computed the participation ratio (PR) of the eigenvalue spectrum obtained from PCA. This measure provides a continuous estimate of how many dimensions effectively contribute to the variance of the population activity.

Let $\{\lambda_1, \lambda_2, \ldots, \lambda_N\}$ be the sequence of the eigenvalues of the covariance matrix of neural activity obtained from PCA, order by magnitude, then the participations ratio PR is defined as:

$$PR = \frac{\left(\sum_{k=1}^{N} \lambda_k\right)^2}{\sum_{k=1}^{N} \lambda_k{}^2}$$

The participation ratio provides an intuitive description of how the eigenvalues are spread across the components: if variance is equally distributed across d components and is zero elsewhere, then

$$PR = d$$

if variance is entirely concentrated on a single dimension, then

$$PR = 1$$

If instead the eigenvalues are equally spread over all the components meaning that the variance is evenly distributed across all the N dimensions, then

$$PR \approx N$$

In this study, PR was computed either on the entire time course of population activity, or separately for the activity during high or low arousal periods. In order to do that, I extracted the $T_{LOW}$ timepoints where pupil area was < 0.1 standard deviations above the mean for the low-arousal condition, and the $T_{HIGH}$ timepoints where it was > 0.3 for the high-arousal condition. In order to ensure a balanced representation of the two conditions, I randomly resampled from the condition with higher number of time points, and assembled the two matrices

$$X_{LOW} \in \mathbb{R}^{T_{L.,H} \times N}$$
$$X_{HIGH} \in \mathbb{R}^{T_{L,H} \times N}$$

where

$$T_{L,H} = \min(T_{LOW}, T_{HIGH})$$

PCA was then on the standardized matrices $X_{LOW}$ and $X_{HIGH}$ separately, and the effective the dimensionality was calculated.

#### 3.5.2.3. Pairwise correlations

In order to directly visualize how the correlation structure was impacted by arousal I also looked at the pairwise correlation matrices of the different sessions. To do that I calculated the Pearson product-moment coefficients between the activity of each pair of neurons during low or high arousal periods, defined as the normalized covariance matrix of $X_{LOW}$ and $X_{HIGH}$ matrices respectively. The average distribution of the absolute correlation coefficients was also calculated across the L4 and L/3 sessions, in order to have a statistic on the effect of arousal for the two datasets.

#### 3.5.2.4. Logistic decoders of stimulus epochs

To quantify how well stimulus epochs of the PGG protocol could be discriminated from population activity, we trained logistic regression classifiers. Given the instantaneous population vector $x(t) \in \mathbb{R}^N$, logistic regression models the probability of belonging to class $y \in \{0,1\}$ as

$$P(y = 1 | x) = \sigma(w^T x + b)$$

where $w \in \mathbb{R}^N$ is the weight vector, b is the bias and $\sigma(z)$ is the logistic function

$$\sigma(z) = \frac{1}{1 + e^{-z}}$$

The stimulus epochs (paid, grey and gratings) were encoded with integer values, generating a sequence of stimulus labels $S^{T\times 1} \in [0,1,2]$, which was then split into $S_{LOW}$ and $S_{HIGH}$ according to the timepoints used for building $X_{LOW}$ and $X_{HIGH}$.

The models were fit using the OneVsRest strategy implemented in the scikit-learn package, effectively fitting a classifier for each class.

For each condition, the models were trained on the timepoints belonging to the first half of the protocol (first repetitions of the three epochs) and tested on the timepoints belonging to the second half. Finally, the accuracy of each classifier was quantified as

$$acc = \frac{1}{n}\sum_{i=0}^{n} 1(\hat{y}_i = y_i)$$

where n is the number of classified samples and $y_i$ and $\hat{y}_i$ are the true and the predicted epoch labels at the sample *i*.

### 3.5.2.5. Linear encoding models and variance partitioning analysis

To quantify how much variance in the recorded neural activity could be explained by stimulus and arousal variables, I fit linear encoding models. The encoding models allowed for an explicit decomposition of the neural variance into the independent contribution coming from arousal and stimulus, as well as estimating the amount of shared variance which cannot unambiguously attributed to either one or the other.

For each neuron i, the activity was modelled as

$$x_i(t) = \beta_{s,i}^T s(t) + \beta_{a,i}^T a(t) + \varepsilon_i(t)$$

where s(t) are the stimulus regressors, a(t) is the arousal regressor and ε(t) is the residual error. Compactly,

$$x_i = Z\beta_i + \varepsilon_i$$

with the design matrix Z = [SA]. Regression coefficients were estimated via ordinary least squares:

$$\hat{\beta}_i = (Z^T Z)^{-1} Z^T x_i$$

Explained variance was quantified using coefficient of determination for each neuron i:

$$R_i^2 = \frac{\sum_t \left(x_i(t) - \hat{x}_i(t)\right)^2}{\sum_t \left(x_i(t) - \bar{x}_i\right)^2}$$

where $\hat{x}_i(t)$ and $\bar{x}_i$ are the predicted activity of neuron i at time t and the mean activity of neuron I, respectively. To compute the unique contribution to neural variance, three separate models were fit: a full model including both stimulus and arousal regressors, a stimulus model including only stimulus regressors and an arousal model including only the arousal regressor. The unique variance for stimulus and pupil were then calculated as

$$R^2_{\text{unique stimulus}} = R^2_{\text{full}} - R^2_{\text{arousal}}$$

and

$$R^2_{\text{unique arousal}} = R^2_{\text{full}} - R^2_{\text{stimulus}}$$

while the shared variance was defined as

$$R^2_{\text{shared}} = R^2_{\text{full}} - R^2_{\text{stimulus}} - R^2_{\text{arousal}}$$

The stimulus regressors used consisted in 5 different statistics computed on each frame of all the stimulation protocols as it was done in [128]; such features included:

*Mean Luminance*, defined as the average pixel intensity μ(I) for the image frame I.

*Contrast*, defined as the standard deviation of pixel intensities σ(I) for the image frame I

*Entropy*, to assess the average information content within each image frame, calculated based on the sample probabilities ($p_i$) of pixel values for the image frame I as

$$H[I] = -\sum_{i=0}^{n_{pixels}} p_i \log_2(p_i)$$

*Energy*, defined as the sum of the absolute difference between the intensities of two consecutive frames

$$E[I] = \sum_{i=0}^{n_{pixels}} |I(t) - I(t-1)|$$

*Edges*, quantified as the fraction of pixels that contribute to edges within a given image frame I; first, the image was convolved with a 5x5 2D gaussian kernel with $\sigma = 5$; The smoothed image was then filtered with the multi-stage edge detector Canny implemented within the cv2 python library. Finally, the image resulting image was binarized and the average was taken, resulting in a fractional quantification of the number of pixels belonging to an edge.

The stimulus design matrix was built by stacking the time series of these statistics calculated separately for 24, non-overlapping squared regions spanning the whole frame image I. For arousal, only pupil size was used as regressor. The activity of each neuron was then independently modelled and the $R^2$ values averaged across runs of a 5-fold cross validation scheme.

### 3.5.2.6. PLS regression and subspaces analysis

Partial Least Squares (PLS) regression was used to find low-dimensional (1-D) coding subspaces for stimulus and arousal signals. While PCA captures variance in neural activity alone, PLS identifies dimensions that maximize covariance between neural activity and external variable. This approach allowed for extracting stimulus-aligned and arousal-aligned subspaces, and to

quantify the alignment between the two.

Given the neural activity matrix $X \in R^{T \times N}$ and the target matrix $Y \in R^{T \times M}$, PLS finds the weight vectors **w** and **c** maximizing covariance:

$$\max_{w,c} \mathrm{Cov}(Xw, Yc)$$

1-D, global stimulus statistics (energy or mean luminance) were used for identifying stimulus coding directions, while either pupil size or locomotion speed were used to find the arousal's. The regression was evaluated by averaging the $R^2$ values across runs of a 5-fold cross-validation and the axes orthonormalized prior to projection and alignment analysis. To quantify alignment between stimulus and arousal subspaces, then computed the cosine similarity between the leading PLS weight vectors:

$$\cos\theta = \frac{w_s^T w_a}{\|w_s\| \|w_a\|}$$

where $w_s$ is the stimulus-aligned axis and $w_a$ is the arousal-aligned one. Values near 0 indicate orthogonality, while values near 1 indicate collinearity. This approach revealed a possible interaction between the alignment of low-dimensional arousal and stimulus subspaces and the quality of sensory input.

# Bibliography


(1) Lapanja, T.; Micheli, P.; González-Guerra, A.; Radomskyi, O.; De Franceschi, G.; Muraveva, A.; Attinger, A.; Roth, C. N.; Tripodi, M.; Boissonnet, T.; Sabbadini, M.; Jüttner, J.; Ala-Laurila, P.; Keller, G.; Allina, G. P.; Asari, H.; Rompani, S. B. Pupil Size Modulation Drives Retinal Activity in Mice and Shapes Human Perception. *Nat. Commun.* **2025**, *16* (1), 7334. https://doi.org/10.1038/s41467-025-62736-4.

(2) Wässle, H. Parallel Processing in the Mammalian Retina. *Nat. Rev. Neurosci.* **2004**, *5* (10), 747–757. https://doi.org/10.1038/nrn1497.

(3) Hartline, H. K. The Response of Single Optic Nerve Fibers of the Vertebrate Eye to Illumination of the Retina. *Am. J. Physiol.-Leg. Content* **1938**, *121* (2), 400–415. https://doi.org/10.1152/ajplegacy.1938.121.2.400.

(4) Kuffler, S. W. Discharge Patterns and Functional Organization of Mammalian Retina. *J. Neurophysiol.* **1953**, *16* (1), 37–68. https://doi.org/10.1152/jn.1953.16.1.37.

(5) Werblin, F. S.; Dowling, J. E. Organization of the Retina of the Mudpuppy, Necturus Maculosus. II. Intracellular Recording. *J. Neurophysiol.* **1969**, *32* (3), 339–355. https://doi.org/10.1152/jn.1969.32.3.339.

(6) Fried, S. I.; Münch, T. A.; Werblin, F. S. Mechanisms and Circuitry Underlying Directional Selectivity in the Retina. *Nature* **2002**, *420* (6914), 411–414. https://doi.org/10.1038/nature01179.

(7) Baden, T.; Berens, P.; Franke, K.; Rosón, M. R.; Bethge, M.; Euler, T. The Functional Diversity of Retinal Ganglion Cells in the Mouse. *Nature* **2016**, *529* (7586), 345–350. https://doi.org/10.1038/nature16468.

(8) Sherman, S. M.; Guillery, R. W. The Role of the Thalamus in the Flow of Information to the Cortex. *Philos. Trans. R. Soc. Lond. B. Biol. Sci.* **2002**, *357* (1428), 1695–1708. https://doi.org/10.1098/rstb.2002.1161.

(9) Casagrande, V. A.; Boyd, J. D. The Neural Architecture of Binocular Vision. *Eye* **1996**, *10* (2), 153–160. https://doi.org/10.1038/eye.1996.40.

(10) Sherman, S. M.; Wilson, J. R.; Guillery, R. W. Evidence That Binocular Competition Affects the Postnatal Development of Y-Cells in the Cat's Lateral Geniculate Nucleus. *Brain Res.* **1975**, *100* (2), 441–444. https://doi.org/10.1016/0006-8993(75)90498-9.

(11) Reese, B. E. "Hidden Lamination" in the Dorsal Lateral Geniculate Nucleus: The Functional Organization of This Thalamic Region in the Rat. *Brain Res.* **1988**, *472* (2), 119–137. https://doi.org/10.1016/0165-0173(88)90017-3.

(12) Godement, P.; Salaün, J.; Imbert, M. Prenatal and Postnatal Development of Retinogeniculate and Retinocollicular Projections in the Mouse. *J. Comp. Neurol.* **1984**, *230* (4), 552–575. https://doi.org/10.1002/cne.902300406.

# Bibliography


(13) Bickford, M. E. Thalamic Circuit Diversity: Modulation of the Driver/Modulator Framework. *Front. Neural Circuits* **2015**, *9*, 86. https://doi.org/10.3389/fncir.2015.00086.

(14) Rompani, S. B.; Müllner, F. E.; Wanner, A.; Zhang, C.; Roth, C. N.; Yonehara, K.; Roska, B. Different Modes of Visual Integration in the Lateral Geniculate Nucleus Revealed by Single-Cell-Initiated Transsynaptic Tracing. *Neuron* **2017**, *93* (4), 767-776.e6. https://doi.org/10.1016/j.neuron.2017.01.028.

(15) Billet, S.; Cant, N. B.; Hall, W. C. Cholinergic Projections to the Visual Thalamus and Superior Colliculus. *Brain Res.* **1999**, *847* (1), 121–123. https://doi.org/10.1016/s0006-8993(99)01900-9.

(16) Papadopoulos, G. C.; Parnavelas, J. G. Distribution and Synaptic Organization of Serotoninergic and Noradrenergic Axons in the Lateral Geniculate Nucleus of the Rat. *J. Comp. Neurol.* **1990**, *294* (3), 345–355. https://doi.org/10.1002/cne.902940304.

(17) McCormick, D. A. Neurotransmitter Actions in the Thalamus and Cerebral Cortex and Their Role in Neuromodulation of Thalamocortical Activity. *Prog. Neurobiol.* **1992**, *39* (4), 337–388. https://doi.org/10.1016/0301-0082(92)90012-4.

(18) Reggiani, J. D. S.; Jiang, Q.; Barbini, M.; Lutas, A.; Liang, L.; Fernando, J.; Deng, F.; Wan, J.; Li, Y.; Chen, C.; Andermann, M. L. Brainstem Serotonin Neurons Selectively Gate Retinal Information Flow to Thalamus. *Neuron* **2023**, *111* (5), 711-726.e11. https://doi.org/10.1016/j.neuron.2022.12.006.

(19) Fei, Y.; Luh, M. Y.; Ontiri, A.; Ghauri, D.; Hu, W.; Liang, L. Coordination of Distinct Sources of Excitatory Inputs Enhances Motion Selectivity in the Mouse Visual Thalamus. *Neuron* **2025**, *113* (20), 3441–3457.

(20) Douglas, R. J.; Martin, K. A. C. NEURONAL CIRCUITS OF THE NEOCORTEX. *Annu. Rev. Neurosci.* **2004**, *27* (Volume 27, 2004), 419–451. https://doi.org/10.1146/annurev.neuro.27.070203.144152.

(21) Scala, F.; Kobak, D.; Shan, S.; Bernaerts, Y.; Laturnus, S.; Cadwell, C. R.; Hartmanis, L.; Froudarakis, E.; Castro, J. R.; Tan, Z. H.; Papadopoulos, S.; Patel, S. S.; Sandberg, R.; Berens, P.; Jiang, X.; Tolias, A. S. Layer 4 of Mouse Neocortex Differs in Cell Types and Circuit Organization between Sensory Areas. *Nat. Commun.* **2019**, *10* (1), 4174. https://doi.org/10.1038/s41467-019-12058-z.

(22) Lien, A. D.; Scanziani, M. Tuned Thalamic Excitation Is Amplified by Visual Cortical Circuits. *Nat. Neurosci.* **2013**, *16* (9), 1315–1323. https://doi.org/10.1038/nn.3488.

(23) Harris, K. D.; Shepherd, G. M. G. The Neocortical Circuit: Themes and Variations. *Nat. Neurosci.* **2015**, *18* (2), 170–181. https://doi.org/10.1038/nn.3917.

(24) Niell, C. M.; Stryker, M. P. Highly Selective Receptive Fields in Mouse Visual Cortex. *J. Neurosci.* **2008**, *28* (30), 7520–7536. https://doi.org/10.1523/JNEUROSCI.0623-08.2008.

(25) Mazo, C.; Baeta, M.; Petreanu, L. Auditory Cortex Conveys Non-Topographic Sound Localization Signals to Visual Cortex. *Nat. Commun.* **2024**, *15* (1), 3116. https://doi.org/10.1038/s41467-024-47546-4.

(26) Petro, L. S.; Paton, A. T.; Muckli, L. Contextual Modulation of Primary Visual Cortex by Auditory Signals. *Philos. Trans. R. Soc. B Biol. Sci.* **2017**, *372* (1714), 20160104. https://doi.org/10.1098/rstb.2016.0104.
(27) Fu, Y.; Tucciarone, J. M.; Espinosa, J. S.; Sheng, N.; Darcy, D. P.; Nicoll, R. A.; Huang, Z. J.; Stryker, M. P. A Cortical Circuit for Gain Control by Behavioral State. *Cell* **2014**, *156* (6), 1139–1152. https://doi.org/10.1016/j.cell.2014.01.050.
(28) Niell, C. M.; Stryker, M. P. Modulation of Visual Responses by Behavioral State in Mouse Visual Cortex. *Neuron* **2010**, *65* (4), 472–479. https://doi.org/10.1016/j.neuron.2010.01.033.
(29) Russell, L. E.; Fişek, M.; Yang, Z.; Tan, L. P.; Packer, A. M.; Dalgleish, H. W. P.; Chettih, S. N.; Harvey, C. D.; Häusser, M. The Influence of Cortical Activity on Perception Depends on Behavioral State and Sensory Context. *Nat. Commun.* **2024**, *15* (1), 2456. https://doi.org/10.1038/s41467-024-46484-5.
(30) Jiang, X.; Shen, S.; Cadwell, C. R.; Berens, P.; Sinz, F.; Ecker, A. S.; Patel, S.; Tolias, A. S. Principles of Connectivity among Morphologically Defined Cell Types in Adult Neocortex. *Science* **2015**, *350* (6264), aac9462. https://doi.org/10.1126/science.aac9462.
(31) Cauller, L. J.; Connors, B. W. Synaptic Physiology of Horizontal Afferents to Layer I in Slices of Rat SI Neocortex. *J. Neurosci.* **1994**, *14* (2), 751–762. https://doi.org/10.1523/JNEUROSCI.14-02-00751.1994.
(32) Larkum, M. E.; Zhu, J. J.; Sakmann, B. A New Cellular Mechanism for Coupling Inputs Arriving at Different Cortical Layers. *Nature* **1999**, *398* (6725), 338–341. https://doi.org/10.1038/18686.
(33) Thomson, A. M. Neocortical Layer 6, A Review. *Front. Neuroanat.* **2010**, *4*, 13. https://doi.org/10.3389/fnana.2010.00013.
(34) Sherman, S. M.; Guillery, R. W. Distinct Functions for Direct and Transthalamic Corticocortical Connections. *J. Neurophysiol.* **2011**, *106* (3), 1068–1077. https://doi.org/10.1152/jn.00429.2011.
(35) Campbell, F. W.; Gregory, A. H. Effect of Size of Pupil on Visual Acuity. *Nature* **1960**, *187* (4743), 1121–1123. https://doi.org/10.1038/1871121c0.
(36) Lykstad, J.; Reddy, V.; Hanna, A. Neuroanatomy, Pupillary Dilation Pathway. In *StatPearls*; StatPearls Publishing: Treasure Island (FL), 2025.
(37) Aston-Jones, G.; Cohen, J. D. AN INTEGRATIVE THEORY OF LOCUS COERULEUS-NOREPINEPHRINE FUNCTION: Adaptive Gain and Optimal Performance. *Annu. Rev. Neurosci.* **2005**, *28* (Volume 28, 2005), 403–450. https://doi.org/10.1146/annurev.neuro.28.061604.135709.
(38) McGinley, M. J.; Vinck, M.; Reimer, J.; Batista-Brito, R.; Zagha, E.; Cadwell, C. R.; Tolias, A. S.; Cardin, J. A.; McCormick, D. A. Waking State: Rapid Variations Modulate Neural and Behavioral Responses. *Neuron* **2015**, *87* (6), 1143–1161. https://doi.org/10.1016/j.neuron.2015.09.012.
(39) Reimer, J.; Froudarakis, E.; Cadwell, C. R.; Yatsenko, D.; Denfield, G. H.; Tolias, A. S. Pupil Fluctuations Track Fast Switching of Cortical States during Quiet Wakefulness. *Neuron* **2014**, *84* (2), 355–362. https://doi.org/10.1016/j.neuron.2014.09.033.

# Bibliography


(40) Joshi, S.; Li, Y.; Kalwani, R. M.; Gold, J. I. Relationships between Pupil Diameter and Neuronal Activity in the Locus Coeruleus, Colliculi, and Cingulate Cortex. *Neuron* **2016**, *89* (1), 221–234. https://doi.org/10.1016/j.neuron.2015.11.028.

(41) Markwell, E. L.; Feigl, B.; Zele, A. J. Intrinsically Photosensitive Melanopsin Retinal Ganglion Cell Contributions to the Pupillary Light Reflex and Circadian Rhythm. *Clin. Exp. Optom.* **2010**, *93* (3), 137–149. https://doi.org/10.1111/j.1444-0938.2010.00479.x.

(42) Mathôt, S.; Van der Stigchel, S. New Light on the Mind's Eye: The Pupillary Light Response as Active Vision. *Curr. Dir. Psychol. Sci.* **2015**, *24* (5), 374–378. https://doi.org/10.1177/0963721415593725.

(43) Mathot, S. Pupillometry: Psychology, Physiology, and Function. *J. Cogn.* **2018**, *1* (1). https://doi.org/10.5334/joc.18.

(44) Kahneman, D.; Beatty, J. Pupil Diameter and Load on Memory. *Science* **1966**, *154* (3756), 1583–1585. https://doi.org/10.1126/science.154.3756.1583.

(45) Murphy, P. R.; O'Connell, R. G.; O'Sullivan, M.; Robertson, I. H.; Balsters, J. H. Pupil Diameter Covaries with BOLD Activity in Human Locus Coeruleus. *Hum. Brain Mapp.* **2014**, *35* (8), 4140–4154. https://doi.org/10.1002/hbm.22466.

(46) Reimer, J.; McGinley, M. J.; Liu, Y.; Rodenkirch, C.; Wang, Q.; McCormick, D. A.; Tolias, A. S. Pupil Fluctuations Track Rapid Changes in Adrenergic and Cholinergic Activity in Cortex. *Nat. Commun.* **2016**, *7* (1), 13289. https://doi.org/10.1038/ncomms13289.

(47) Cazettes, F.; Reato, D.; Morais, J. P.; Renart, A.; Mainen, Z. F. Phasic Activation of Dorsal Raphe Serotonergic Neurons Increases Pupil Size. *Curr. Biol.* **2021**, *31* (1), 192-197.e4. https://doi.org/10.1016/j.cub.2020.09.090.

(48) Preuschoff, K.; 't Hart, B. M.; Einhäuser, W. Pupil Dilation Signals Surprise: Evidence for Noradrenaline's Role in Decision Making. *Front. Neurosci.* **2011**, *5*, 115. https://doi.org/10.3389/fnins.2011.00115.

(49) The Role of Active Forebrain and Humoral Systems in Sleep Control. In *Brain Control of Wakefulness and Sleep*; Steriade, M., McCarley, R. W., Eds.; Springer US: Boston, MA, 2005; pp 561–610. https://doi.org/10.1007/0-387-26270-9_13.

(50) Harris, K. D.; Thiele, A. Cortical State and Attention. *Nat. Rev. Neurosci.* **2011**, *12* (9), 509–523. https://doi.org/10.1038/nrn3084.

(51) Cohen, M. R.; Maunsell, J. H. Attention Improves Performance Primarily by Reducing Interneuronal Correlations. *Nat. Neurosci.* **2009**, *12* (12), 1594–1600. https://doi.org/10.1038/nn.2439.

(52) Renart, A.; de la Rocha, J.; Bartho, P.; Hollender, L.; Parga, N.; Reyes, A.; Harris, K. D. The Asynchronous State in Cortical Circuits. *Science* **2010**, *327* (5965), 587–590. https://doi.org/10.1126/science.1179850.

(53) Stringer, C.; Pachitariu, M.; Steinmetz, N.; Carandini, M.; Harris, K. D. High-Dimensional Geometry of Population Responses in Visual Cortex. *Nature* **2019**, *571* (7765), 361–365. https://doi.org/10.1038/s41586-019-1346-5.

(54) Pinto, L.; Goard, M. J.; Estandian, D.; Xu, M.; Kwan, A. C.; Lee, S.-H.; Harrison, T. C.; Feng, G.; Dan, Y. Fast Modulation of Visual Perception by Basal Forebrain Cholinergic Neurons. *Nat. Neurosci.* **2013**, *16* (12), 1857–1863. https://doi.org/10.1038/nn.3552.

(55) Yogesh, B.; Keller, G. B. Cholinergic Input to Mouse Visual Cortex Signals a Movement State and Acutely Enhances Layer 5 Responsiveness. *eLife* **2024**, *12*, RP89986. https://doi.org/10.7554/eLife.89986.
(56) Raut, R. V.; Rosenthal, Z. P.; Wang, X.; Miao, H.; Zhang, Z.; Lee, J.-M.; Raichle, M. E.; Bauer, A. Q.; Brunton, S. L.; Brunton, B. W.; Kutz, J. N. Arousal as a Universal Embedding for Spatiotemporal Brain Dynamics. *Nature* **2025**, *647* (8089), 454–461. https://doi.org/10.1038/s41586-025-09544-4.
(57) Stringer, C.; Pachitariu, M.; Steinmetz, N.; Reddy, C. B.; Carandini, M.; Harris, K. D. Spontaneous Behaviors Drive Multidimensional, Brainwide Activity. *Science* **2019**, *364* (6437), eaav7893. https://doi.org/10.1126/science.aav7893.
(58) Dadarlat, M. C.; Stryker, M. P. Locomotion Enhances Neural Encoding of Visual Stimuli in Mouse V1. *J. Neurosci.* **2017**, *37* (14), 3764–3775. https://doi.org/10.1523/JNEUROSCI.2728-16.2017.
(59) Engel, T. A.; Steinmetz, N. A.; Gieselmann, M. A.; Thiele, A.; Moore, T.; Boahen, K. Selective Modulation of Cortical State during Spatial Attention. *Science* **2016**, *354* (6316), 1140–1144. https://doi.org/10.1126/science.aag1420.
(60) Vinck, M.; Batista-Brito, R.; Knoblich, U.; Cardin, J. A. Arousal and Locomotion Make Distinct Contributions to Cortical Activity Patterns and Visual Encoding. *Neuron* **2015**, *86* (3), 740–754. https://doi.org/10.1016/j.neuron.2015.03.028.
(61) Pfeffer, C. K.; Xue, M.; He, M.; Huang, Z. J.; Scanziani, M. Inhibition of Inhibition in Visual Cortex: The Logic of Connections between Molecularly Distinct Interneurons. *Nat. Neurosci.* **2013**, *16* (8), 1068–1076. https://doi.org/10.1038/nn.3446.
(62) Engel, T. A.; Steinmetz, N. A. New Perspectives on Dimensionality and Variability from Large-Scale Cortical Dynamics. *Curr. Opin. Neurobiol.* **2019**, *58*, 181–190. https://doi.org/10.1016/j.conb.2019.09.003.
(63) Avitan, L.; Stringer, C. Not so Spontaneous: Multi-Dimensional Representations of Behaviors and Context in Sensory Areas. *Neuron* **2022**, *110* (19), 3064–3075. https://doi.org/10.1016/j.neuron.2022.06.019.
(64) Reynolds, J. H.; Heeger, D. J. The Normalization Model of Attention. *Neuron* **2009**, *61* (2), 168–185. https://doi.org/10.1016/j.neuron.2009.01.002.
(65) Horrocks, E. A. B.; Rodrigues, F. R.; Saleem, A. B. Flexible Neural Population Dynamics Govern the Speed and Stability of Sensory Encoding in Mouse Visual Cortex. *Nat. Commun.* **2024**, *15* (1), 6415. https://doi.org/10.1038/s41467-024-50563-y.
(66) Lin, I.-C.; Okun, M.; Carandini, M.; Harris, K. D. The Nature of Shared Cortical Variability. *Neuron* **2015**, *87* (3), 644–656. https://doi.org/10.1016/j.neuron.2015.06.035.
(67) Erisken, S.; Vaiceliunaite, A.; Jurjut, O.; Fiorini, M.; Katzner, S.; Busse, L. Effects of Locomotion Extend throughout the Mouse Early Visual System. *Curr. Biol.* **2014**, *24* (24), 2899–2907. https://doi.org/10.1016/j.cub.2014.10.045.
(68) McGinley, M. J.; Vinck, M.; Reimer, J.; Batista-Brito, R.; Zagha, E.; Cadwell, C. R.; Tolias, A. S.; Cardin, J. A.; McCormick, D. A. Waking State: Rapid Variations Modulate Neural and Behavioral Responses. *Neuron* **2015**, *87* (6), 1143–1161. https://doi.org/10.1016/j.neuron.2015.09.012.

# Bibliography


(69) Reimer, J.; Froudarakis, E.; Cadwell, C. R.; Yatsenko, D.; Denfield, G. H.; Tolias, A. S. Pupil Fluctuations Track Fast Switching of Cortical States during Quiet Wakefulness. *Neuron* **2014**, *84* (2), 355–362. https://doi.org/10.1016/j.neuron.2014.09.033.

(70) Schröder, S.; Steinmetz, N. A.; Krumin, M.; Pachitariu, M.; Rizzi, M.; Lagnado, L.; Harris, K. D.; Carandini, M. Arousal Modulates Retinal Output. *Neuron* **2020**, *107* (3), 487-495.e9. https://doi.org/10.1016/j.neuron.2020.04.026.

(71) Vinck, M.; Batista-Brito, R.; Knoblich, U.; Cardin, J. A. Arousal and Locomotion Make Distinct Contributions to Cortical Activity Patterns and Visual Encoding. *Neuron* **2015**, *86* (3), 740–754. https://doi.org/10.1016/j.neuron.2015.03.028.

(72) Reeves, P. Rate of Pupillary Dilation and Contraction. *Psychol. Rev.* **1918**, *25* (4), 330–340. https://doi.org/10.1037/h0075293.

(73) Solomons, H. *Binocular Vision: A Programmed Text*; William Heinemann Medical Books Ltd: London, 1978.

(74) Barrionuevo, P. A.; Issolio, L. A.; Tripolone, C. Photoreceptor Contributions to the Human Pupil Light Reflex. *J. Photochem. Photobiol.* **2023**, *15*, 100178. https://doi.org/10.1016/j.jpap.2023.100178.

(75) Franke, K.; Willeke, K. F.; Ponder, K.; Galdamez, M.; Zhou, N.; Muhammad, T.; Patel, S.; Froudarakis, E.; Reimer, J.; Sinz, F. H.; Tolias, A. S. State-Dependent Pupil Dilation Rapidly Shifts Visual Feature Selectivity. *Nature* **2022**, *610* (7930), 128–134. https://doi.org/10.1038/s41586-022-05270-3.

(76) Barlow, H. B. THE INFORMATION CAPACITY OF NERVOUS TRANSMISSION. *Kybernetik* **1963**, *2*, 1. https://doi.org/10.1007/BF00292103.

(77) Barlow, H. B.; Levick, W. R. The Mechanism of Directionally Selective Units in Rabbit's Retina. *J. Physiol.* **1965**, *178* (3), 477–504.

(78) Olveczky, B. P.; Baccus, S. A.; Meister, M. Segregation of Object and Background Motion in the Retina. *Nature* **2003**, *423* (6938), 401–408. https://doi.org/10.1038/nature01652.

(79) Cottaris, N. P.; Jiang, H.; Ding, X.; Wandell, B. A.; Brainard, D. H. A Computational-Observer Model of Spatial Contrast Sensitivity: Effects of Wave-Front-Based Optics, Cone-Mosaic Structure, and Inference Engine. *J. Vis.* **2019**, *19* (4), 8. https://doi.org/10.1167/19.4.8.

(80) Denton, E. J. THE RESPONSES OF THE PUPIL OF GEKKO GEKKO TO EXTERNAL LIGHT STIMULUS. *J. Gen. Physiol.* **1956**, *40* (2), 201–216. https://doi.org/10.1085/jgp.40.2.201.

(81) Laughlin, S. B. Retinal Information Capacity and the Function of the Pupil. *Ophthalmic Physiol. Opt.* **1992**, *12* (2), 161–164. https://doi.org/10.1111/j.1475-1313.1992.tb00281.x.

(82) Atchison, D. A.; Smith, G.; Efron, N. The Effect of Pupil Size on Visual Acuity in Uncorrected and Corrected Myopia. *Am. J. Optom. Physiol. Opt.* **1979**, *56* (5), 315–323. https://doi.org/10.1097/00006324-197905000-00006.

(83) Matthis, J. S.; Muller, K. S.; Bonnen, K. L.; Hayhoe, M. M. Retinal Optic Flow during Natural Locomotion. *PLOS Comput. Biol.* **2022**, *18* (2), e1009575. https://doi.org/10.1371/journal.pcbi.1009575.

(84) Smith, G.; Atchison, D. A. *The Eye and Visual Optical Instruments*; Cambridge University Press: Cambridge, 1997. https://doi.org/10.1017/CBO9780511609541.
(85) Crombie, D.; Spacek, M. A.; Leibold, C.; Busse, L. Spiking Activity in the Visual Thalamus Is Coupled to Pupil Dynamics across Temporal Scales. bioRxiv January 15, 2024, p 2021.04.30.442134. https://doi.org/10.1101/2021.04.30.442134.
(86) Fitzpatrick, M. J.; Krizan, J.; Hsiang, J.-C.; Shen, N.; Kerschensteiner, D. A Pupillary Contrast Response in Mice and Humans: Neural Mechanisms and Visual Functions. *Neuron* **2024**, S0896627324002733. https://doi.org/10.1016/j.neuron.2024.04.012.
(87) Mathôt, S. Pupillometry: Psychology, Physiology, and Function. *J. Cogn.* **2018**, *1* (1), 16. https://doi.org/10.5334/joc.18.
(88) Clarke, R. J.; Zhang, H.; Gamlin, P. D. R. Characteristics of the Pupillary Light Reflex in the Alert Rhesus Monkey. *J. Neurophysiol.* **2003**, *89* (6), 3179–3189. https://doi.org/10.1152/jn.01131.2002.
(89) Medina, J. M.; Jiménez, J. R.; Jiménez del Barco, L. The Effect of Pupil Size on Binocular Summation at Suprathreshold Conditions. *Curr. Eye Res.* **2003**, *26* (6), 327–334. https://doi.org/10.1076/ceyr.26.5.327.15434.
(90) Thomson, L. C. Binocular Summation within the Nervous Pathways of the Pupillary Light Reflex. *J. Physiol.* **1947**, *106* (1), 59–65.
(91) Hubel, D. H. Single Unit Activity in Lateral Geniculate Body and Optic Tract of Unrestrained Cats. *J. Physiol.* **1960**, *150* (1), 91–104. https://doi.org/10.1113/jphysiol.1960.sp006375.
(92) Hubel, D. H.; Wiesel, T. N. Receptive Fields, Binocular Interaction and Functional Architecture in the Cat's Visual Cortex. *J. Physiol.* **1962**, *160* (1), 106–154. https://doi.org/10.1113/jphysiol.1962.sp006837.
(93) Sperry, R. W. Neural Basis of the Spontaneous Optokinetic Response Produced by Visual Inversion. *J. Comp. Physiol. Psychol.* **1950**, *43* (6), 482–489. https://doi.org/10.1037/h0055479.
(94) Crapse, T. B.; Sommer, M. A. Corollary Discharge across the Animal Kingdom. *Nat. Rev. Neurosci.* **2008**, *9* (8), 587–600. https://doi.org/10.1038/nrn2457.
(95) Jüttner, J.; Szabo, A.; Gross-Scherf, B.; Morikawa, R. K.; Rompani, S. B.; Hantz, P.; Szikra, T.; Esposti, F.; Cowan, C. S.; Bharioke, A.; Patino-Alvarez, C. P.; Keles, Ö.; Kusnyerik, A.; Azoulay, T.; Hartl, D.; Krebs, A. R.; Schübeler, D.; Hajdu, R. I.; Lukats, A.; Nemeth, J.; Nagy, Z. Z.; Wu, K.-C.; Wu, R.-H.; Xiang, L.; Fang, X.-L.; Jin, Z.-B.; Goldblum, D.; Hasler, P. W.; Scholl, H. P. N.; Krol, J.; Roska, B. Targeting Neuronal and Glial Cell Types with Synthetic Promoter AAVs in Mice, Non-Human Primates and Humans. *Nat. Neurosci.* **2019**, *22* (8), 1345–1356. https://doi.org/10.1038/s41593-019-0431-2.
(96) Liang, L.; Fratzl, A.; Reggiani, J. D. S.; El Mansour, O.; Chen, C.; Andermann, M. L. Retinal Inputs to the Thalamus Are Selectively Gated by Arousal. *Curr. Biol.* **2020**. https://doi.org/10.1016/j.cub.2020.07.065.
(97) Liang, L.; Fratzl, A.; Goldey, G.; Ramesh, R. N.; Sugden, A. U.; Morgan, J. L.; Chen, C.; Andermann, M. L. A Fine-Scale Functional Logic to Convergence from Retina to Thalamus. *Cell* **2018**, *173* (6), 1343-1355.e24. https://doi.org/10.1016/j.cell.2018.04.041.

(98) Bharioke, A.; Munz, M.; Brignall, A.; Kosche, G.; Eizinger, M. F.; Ledergerber, N.; Hillier, D.; Gross-Scherf, B.; Conzelmann, K.-K.; Macé, E.; Roska, B. General Anesthesia Globally Synchronizes Activity Selectively in Layer 5 Cortical Pyramidal Neurons. *Neuron* **2022**, *110* (12), 2024-2040.e10. https://doi.org/10.1016/j.neuron.2022.03.032.

(99) Baden, T.; Berens, P.; Franke, K.; Román Rosón, M.; Bethge, M.; Euler, T. The Functional Diversity of Retinal Ganglion Cells in the Mouse. *Nature* **2016**, *529* (7586), 345–350. https://doi.org/10.1038/nature16468.

(100) Dougherty, K.; Schmid, M. C.; Maier, A. Binocular Response Modulation in the Lateral Geniculate Nucleus. *J. Comp. Neurol.* **2019**, *527* (3), 522–534. https://doi.org/10.1002/cne.24417.

(101) Howarth, M.; Walmsley, L.; Brown, T. M. Binocular Integration in the Mouse Lateral Geniculate Nuclei. *Curr. Biol.* **2014**, *24* (11), 1241–1247. https://doi.org/10.1016/j.cub.2014.04.014.

(102) Zeater, N.; Cheong, S. K.; Solomon, S. G.; Dreher, B.; Martin, P. R. Binocular Visual Responses in the Primate Lateral Geniculate Nucleus. *Curr. Biol.* **2015**, *25* (24), 3190–3195. https://doi.org/10.1016/j.cub.2015.10.033.

(103) Bauer, J.; Weiler, S.; Fernholz, M. H. P.; Laubender, D.; Scheuss, V.; Hübener, M.; Bonhoeffer, T.; Rose, T. Limited Functional Convergence of Eye-Specific Inputs in the Retinogeniculate Pathway of the Mouse. *Neuron* **2021**, S0896627321004153. https://doi.org/10.1016/j.neuron.2021.05.036.

(104) Román Rosón, M.; Bauer, Y.; Kotkat, A. H.; Berens, P.; Euler, T.; Busse, L. Mouse dLGN Receives Functional Input from a Diverse Population of Retinal Ganglion Cells with Limited Convergence. *Neuron* **2019**, *102* (2), 462-476.e8. https://doi.org/10.1016/j.neuron.2019.01.040.

(105) Pirenne, M. H. Binocular and Uniocular Threshold of Vision. *Nature* **1943**, *152* (3867), 698–699. https://doi.org/10.1038/152698a0.

(106) Baker, D. H.; Lygo, F. A.; Meese, T. S.; Georgeson, M. A. Binocular Summation Revisited: Beyond √2. *Psychol. Bull.* **2018**, *144* (11), 1186–1199. https://doi.org/10.1037/bul0000163.

(107) Bearse, M. A.; Freeman, R. D. Binocular Summation in Orientation Discrimination Depends on Stimulus Contrast and Duration. *Vision Res.* **1994**, *34* (1), 19–29. https://doi.org/10.1016/0042-6989(94)90253-4.

(108) Campbell, F. W.; Green, D. G. Monocular versus Binocular Visual Acuity. *Nature* **1965**, *208* (5006), 191–192. https://doi.org/10.1038/208191a0.

(109) Dougherty, K.; Carlson, B. M.; Cox, M. A.; Westerberg, J. A.; Zinke, W.; Schmid, M. C.; Martin, P. R.; Maier, A. Binocular Suppression in the Macaque Lateral Geniculate Nucleus Reveals Early Competitive Interactions between the Eyes. *eneuro* **2021**, ENEURO.0364-20.2020. https://doi.org/10.1523/ENEURO.0364-20.2020.

(110) Morgan, J. L.; Berger, D. R.; Wetzel, A. W.; Lichtman, J. W. The Fuzzy Logic of Network Connectivity in Mouse Visual Thalamus. *Cell* **2016**, *165* (1), 192–206. https://doi.org/10.1016/j.cell.2016.02.033.

(111) Rompani, S. B.; Müllner, F. E.; Wanner, A.; Zhang, C.; Roth, C. N.; Yonehara, K.; Roska, B. Different Modes of Visual Integration in the Lateral Geniculate

Nucleus Revealed by Single-Cell-Initiated Transsynaptic Tracing. *Neuron* **2017**, *93* (4), 767-776.e6. https://doi.org/10.1016/j.neuron.2017.01.028.
(112) Busse, L. The influence of locomotion on sensory processing and its underlying neuronal circuits. *E-Neuroforum* **2018**, *24* (1), A41–A51. https://doi.org/10.1515/nf-2017-A046.
(113) Waterhouse, B. D.; Navarra, R. L. The Locus Coeruleus-Norepinephrine System and Sensory Signal Processing: A Historical Review and Current Perspectives. *Brain Res.* **2019**, *1709*, 1–15. https://doi.org/10.1016/j.brainres.2018.08.032.
(114) Mazziotti, R.; Carrara, F.; Viglione, A.; Lupori, L.; Lo Verde, L.; Benedetto, A.; Ricci, G.; Sagona, G.; Amato, G.; Pizzorusso, T. MEYE: Web App for Translational and Real-Time Pupillometry. *eNeuro* **2021**, *8* (5), ENEURO.0122-21.2021. https://doi.org/10.1523/ENEURO.0122-21.2021.
(115) Stringer, C.; Pachitariu, M. Cellpose3: One-Click Image Restoration for Improved Cellular Segmentation. *Nat. Methods* **2025**, *22* (3), 592–599. https://doi.org/10.1038/s41592-025-02595-5.
(116) Arieli, A.; Sterkin, A.; Grinvald, A.; Aertsen, A. Dynamics of Ongoing Activity: Explanation of the Large Variability in Evoked Cortical Responses. *Science* **1996**, *273* (5283), 1868–1871. https://doi.org/10.1126/science.273.5283.1868.
(117) Destexhe, A.; Contreras, D. Neuronal Computations with Stochastic Network States. *Science* **2006**, *314* (5796), 85–90. https://doi.org/10.1126/science.1127241.
(118) Faisal, A. A.; Selen, L. P. J.; Wolpert, D. M. Noise in the Nervous System. *Nat. Rev. Neurosci.* **2008**, *9* (4), 292–303. https://doi.org/10.1038/nrn2258.
(119) Salinas, E.; Thier, P. Gain Modulation: A Major Computational Principle of the Central Nervous System. *Neuron* **2000**, *27* (1), 15–21. https://doi.org/10.1016/s0896-6273(00)00004-0.
(120) Polack, P.-O.; Friedman, J.; Golshani, P. Cellular Mechanisms of Brain State–Dependent Gain Modulation in Visual Cortex. *Nat. Neurosci.* **2013**, *16* (9), 1331–1339. https://doi.org/10.1038/nn.3464.
(121) Musall, S.; Kaufman, M. T.; Juavinett, A. L.; Gluf, S.; Churchland, A. K. Single-Trial Neural Dynamics Are Dominated by Richly Varied Movements. *Nat. Neurosci.* **2019**, *22* (10), 1677–1686. https://doi.org/10.1038/s41593-019-0502-4.
(122) Zhuang, J.; Bereshpolova, Y.; Stoelzel, C. R.; Huff, J. M.; Hei, X.; Alonso, J.-M.; Swadlow, H. A. Brain State Effects on Layer 4 of the Awake Visual Cortex. *J. Neurosci.* **2014**, *34* (11), 3888–3900. https://doi.org/10.1523/JNEUROSCI.4969-13.2014.
(123) McCormick, D. A.; Nestvogel, D. B.; He, B. J. Neuromodulation of Brain State and Behavior. *Annu. Rev. Neurosci.* **2020**, *43* (Volume 43, 2020), 391–415. https://doi.org/10.1146/annurev-neuro-100219-105424.
(124) Cohen, M. R.; Kohn, A. Measuring and Interpreting Neuronal Correlations. *Nat. Neurosci.* **2011**, *14* (7), 811–819. https://doi.org/10.1038/nn.2842.
(125) Larkum, M. A Cellular Mechanism for Cortical Associations: An Organizing Principle for the Cerebral Cortex. *Trends Neurosci.* **2013**, *36* (3), 141–151. https://doi.org/10.1016/j.tins.2012.11.006.

# Bibliography

(126) Ebrahimi, S.; Lecoq, J.; Rumyantsev, O.; Tasci, T.; Zhang, Y.; Irimia, C.; Li, J.; Ganguli, S.; Schnitzer, M. J. Emergent Reliability in Sensory Cortical Coding and Inter-Area Communication. *Nature* **2022**, *605* (7911), 713–721. https://doi.org/10.1038/s41586-022-04724-y.

(127) Stringer, C.; Ki, C.; DelGrosso, N.; LaFosse, P.; Zhang, Q.; Pachitariu, M. Extracting Large-Scale Neural Activity with Suite2p. bioRxiv February 6, 2026, p 2026.02.04.703741. https://doi.org/10.64898/2026.02.04.703741.

(128) Akella, S.; Ledochowitsch, P.; Siegle, J. H.; Belski, H.; Denman, D. D.; Buice, M. A.; Durand, S.; Koch, C.; Olsen, S. R.; Jia, X. Deciphering Neuronal Variability across States Reveals Dynamic Sensory Encoding. *Nat. Commun.* **2025**, *16* (1), 1768. https://doi.org/10.1038/s41467-025-56733-w.

# List of publications

Lapanja, T., **Micheli, P**. *et al.* Pupil size modulation drives retinal activity in mice and shapes human perception. *Nat Commun* **16**, 7334 (2025). https://doi.org/10.1038/s41467-025-62736-4